U.PORTO

FEUP FACULDADE DE ENGENHARIA
UNIVERSIDADE DO PORTO

Numerical Simulation of Metal Cutting Processes Based on DEFORM™ software

Tiago Emanuel Fraga da Silva

Master's Dissertation

Supervisor: Prof. Dr. Abílio Manuel Pinho de Jesus

Integrated Masters in Mechanical Engineering

Faculty of Engineering of the University of Porto

July 2016

The funding of Project NORTE-01-0145-FEDER-000022 - SciTech, co-financed by NORTE2020, through FEDER is acknowledged.

Also the METALCUT/LAETA project is acknowledged for the granted scholarship funding and INEGI is also acknowledged for having hosted me during my Thesis Project.

To my dear family and friends

Numerical Simulation of Metal Cutting Processes Based on DEFORM™ software

Abstract

This dissertation presents an investigation on the numerical simulation using DEFORM™ software of two and three-dimensional turning operation for the aluminium alloy AlSi9Cu3 with PCD tools, followed by experimental validation. For that purpose, a literature review on the analytical models concerning metal cutting and on the main aspects of numerical simulation was performed.

In order to understand the influence of the several input simulation parameters, a numerical sensitivity analysis on cutting speed, uncut chip thickness, tool rake angle, tool cutting edge radius, shear friction coefficient, heat transfer coefficient, mesh element size and iteration method is conducted for two-dimensional orthogonal cutting models and selecting three very distinct workpiece materials from DEFORM™ material library: an aluminium alloy, a stainless steel and a titanium alloy.

Experimental work on the determination of Coulomb friction coefficient, through orthogonal turning operation is performed. Cast aluminium alloy AlSi9Cu3 is also characterized at low strain-rate and room temperature. The material behaviour for high strain-rates was estimated by similarity to a cast aluminium alloy available in DEFORM™ material library.

It was found that material characterization plays a very significant role in the simulation results. The registered cutting forces obtained from the two-dimensional numerical model with workpiece material from software's library correlated well with the experimental values for AlSi9Cu3, with a relative error lower than 10%. For the characterized material AlSi9Cu3, the cutting forces obtained by two-dimensional modelling simulation were predicted by default, while for three-dimensional modelling, by excess with an average relative error of 46,7%. Simulated temperature fields in some cases revealed to be excessive which demands for better friction model characterization using hybrid shear-Coulomb friction models.

Resumo

A presente dissertação expõe a investigação de simulação numérica 2D e 3D utilizando o software DEFORM™ de processos de torneamento para a liga de alumínio vazada AlSi9Cu3 com ferramentas PCD, seguida de validação experimental. Para esse efeito, foi realizada uma revisão bibliográfica aos modelos analíticos relativos ao corte por arranque de apara assim como aos principais aspetos da simulação numérica de processos de maquinagem.

De forma a entender a influência de vários parâmetros de entrada na simulação numérica foi feita uma análise de sensibilidade à velocidade de corte, espessura da apara antes de deformada, ângulo da face de ataque da ferramenta, raio da extremidade da ferramenta de corte, coeficiente de corte (atrito), coeficiente de transferência de calor, tamanho do elemento finito e método iterativo. Foram usados modelos numéricos bidimensionais e foram selecionados três materiais distintos para a peça a maquinar, disponíveis na biblioteca de materiais do software DEFORM™: uma liga de alumínio, aço inoxidável e uma liga de titânio.

Foi feito trabalho experimental para a determinação do coeficiente de fricção de Coulomb, através da execução de testes de corte ortogonal num torno usando a liga AlSi9Cu3. A liga de alumínio vazada AlSi9Cu3 é caracterizada a baixas taxas de deformação e temperatura ambiente com base em ensaios de compressão. O comportamento deste material a elevadas taxas de deformação e temperaturas foi estimado por similaridade à liga vazada presente na biblioteca de materiais do software DEFORM™.

A caracterização do material tem uma grande influência nos resultados da simulação. As forças de corte obtidas para modelos numéricos bidimensionais com um material semelhante ao caracterizado experimentalmente, presente na biblioteca do software, aproximam-se dos resultados experimentais obtidos para a liga AlSi9Cu3, com um erro relativo inferior a 10%. Para o material caracterizado, AlSi9Cu3, as forças de corte simuladas a partir de modelos numéricos bidimensionais foram previstas por defeito enquanto que para modelos tridimensionais, por excesso, com um erro relativo médio de 46,7%. Os campos de temperaturas simulados resultaram em valores excessivos o que requer uma melhor caracterização dos modelos de fricção recorrendo a modelos híbridos de corte-Coulomb.

Acknowledgements

Firstly, I would like to express my sincere gratitude to my advisor Prof. Abílio Jesus for the continuous support of my Master's dissertation and related research, for his patience, motivation, dedication and immense knowledge. His guidance helped me in all the time of research and writing of this thesis.

I would also like to thank Prof. Pedro Rosa, responsible for the mechanical workshops at IST, for his availability and disposal of equipment for experimental tests.

I would like to thank my colleague Rui Soares for all the help with experimental work and for the useful information regarding the machinability studies that he conducted.

I would like to thank my colleague Santiago Villa for his insightful comments and encouragement throughout the writing of this dissertation.

I would like to thank Prof. M. Parente, for the precious help and instructions related to CAD software manipulation.

To my friends, specially José, Inês, Miguel, Paulo e Bruno, I would like to thank for the support and true friendship throughout this stage of our lives.

I must express my very profound gratitude to my parents, my brother and my girlfriend for providing me with unfailing support and continuous encouragement throughout my years of study, through the process of researching, writing this thesis and life in general. This accomplishment would not have been possible without them. Thank you.

The funding of Project NORTE-01-0145-FEDER-000022 - SciTech, co-financed by NORTE2020, through FEDER is acknowledged.

Also the METALCUT/LAETA project is acknowledged for the granted scholarship funding and INEGI is also acknowledged for having hosted me during my Thesis Project.

Table of Contents

Symbols and Abbreviations

A_s	Shear plane area
F_c	Cutting force
F_f	Feed force
F_n	Normal force
F_r	Radial force
F_s	Shear force
T_f	Melting temperature
T_{room}	Room temperature
t_c	Chip thickness after cut
v_c	Cutting speed
v_{ch}	Chip speed
γ_w	Wedge angle
ε_f	Plastic strain
θ_c	Clearance angle
$\dot{\bar{\varepsilon}}_0$	Equivalent plastic strain rate reference
$\dot{\bar{\varepsilon}}$	Equivalent plastic strain-rate
$\bar{\varepsilon}$	Equivalent plastic strain
$\bar{\sigma}$	Equivalent plastic stress
σ_1	Maximum principal stress
σ_3	Minimum principal stress
τ_s	Average stress on the shear plane
Al	Aluminium
BUE	Built up edges
CAD	Computer aided design
D	Damage parameter
E	Elasticity modulus
FEM	Finite Element Method
PCD	Polycrystalline diamond
Ti	Titanium
WC	Tungsten carbide
T	Temperature
b	Width of cut

m	Shear friction coefficient
r	Chip thickness cutting ratio
t	Uncut chip thickness
w	Depth of cut
α	Rake angle
β	Merchant circle friction angle
ε	Strain
η	Stress triaxiality
θ	Lode Angle parameter
λ	Cutting edge inclination angle
μ	Coulomb friction coefficient
ρ	Density
ϕ	Shear angle

List of Figures

List of Tables

1 INTRODUCTION

1.1 Project's framework and motivation

Predictive industry has significantly improved over the last years. Metal cutting, and in a broader way, machining processes are not an exception. This dissertation results from an attempt of enriching the metal cutting field that is currently being developed at the Faculty of Engineering of the University of Porto and its industry interface investigation institution – INEGI. Upon an investment in a Finite Element Method software directed to machining operations - DEFORMTM 2D/3D – a set of strategic goals were defined in order to achieve proficiency in the mentioned computer program and metal cutting field as a consequence. The simulation of Metal Cutting of cast aluminium alloy using PCD inserts with chip breakers is also an ultimate goal for which this thesis will produce an increment. It will continue a previous experimental work that compared in an experimental perspective the machinability of different inserts (PCD, hard metal, distinct chip breakers) used in AlSi9Cu3 cast aluminium alloy. Predictive models for turning operations using such kind of inserts is envisaged.

1.2 Objectives

The goal of this dissertation is the numerical simulation and experimental validation of metal cutting processes using DEFORM™ 2D/3D commercial FEM software. In order to achieve what is the major goal of this work, some intermediate objectives, fully described in chapter 1.3 Project Approach, were defined:

- An initial exploratory work of DEFORM™ capabilities and potential, going through literature review and performing a sensitivity analysis of metal cutting simulation parameters;
- Material characterization, with the purpose of input information for simulations, achieved by means of experimental compression tests;
- Orthogonal cutting input friction data retrieved through experimental machining tests;
- Numerical simulation of external cutting operations using PCD tools with flat rake surface and using different material and modelling strategies and comparison with existing experimental data.

1.3 Project Approach

This thesis project was supported by a set of tasks that are summarized as follows:

Task 1: Literature review and DEFORM™ 2D/3D initiation steps (4 weeks)

The objective of this task is to perform a literature review on the mechanics as well as analytical modelling of orthogonal cutting. It is also a goal to adjust to the software and understand its main capabilities and limitations.

Task 2: Review of DEFORM™ 2D/3D capabilities (4 weeks)

The objective of this task is to perform a state-of-the-art concerning the numerical simulation of metal cutting, taking into account the following issues: constitutive plastic-damage-fracture models used for workpiece material, heat transfer models, friction models, discretization strategies (Lagrangian/Eulerian). It is also a goal to study DEFORM™ 2D/3D capabilities concerning the simulation of metal cutting operations and to establish a comparison with literature state-of-the-art.

Task 3: Metal cutting sensitivity analysis (6 weeks)

The objective of this task is to select certain metal cutting simulation parameters (process, material and numerical) and build FEM models in DEFORM™ 2D in order to put them through a sensitivity analysis. Obtained results are subjected to a critical review taking into account what was reviewed in the previous task.

Task 4: Material and metal cutting process characterization (5 weeks)

The objective of this task is to run compression tests of aluminium alloy AlSi9Cu3 for further input material data (flow stress curves), fully accomplished by analytical manipulation, trial and error approach and inverse methodologies. Orthogonal cutting tests are also done in order to understand friction conditions among a defined range of cutting parameters.

Task 5: (6 weeks)

The aim of this task is to build and run FEM simulation depicting the turning process in two and three-dimensional approaches with both software's library material and characterized material as well as a chip geometry study and further analysis of the obtained results.

1.4 Structure of this dissertation

In Chapter 1 a brief explanation of the goals, approaches and context of this project are presented as an introductory part of this dissertation. In Chapter 2, Theoretical Modelling of Metal Cutting, a literature review on the main concepts of metal cutting and its analytical modelling is performed, focusing on the mechanical frictional and thermal aspects. In Chapter 3, Simulation of Metal Cutting Using Finite Element Method, the most frequent approaches to FEM metal cutting simulation are reviewed. Discretization strategies material, friction, thermal and damage models are examined and compared with DEFORMTM software capabilities. In Chapter 4, in order to understand the influence of each orthogonal cutting process parameters, tool geometry, friction and numerical parameters are investigated through a sensitivity analysis. Chapter 5 corresponds to the experimental procedure where Cast aluminium alloy AlSi9Cu3 is mechanically characterized through compression tests. Orthogonal cutting tests are conducted in order to infer certain aspects for further simulation input such as load forces, chip geometry and friction parameters. In Chapter 6, DEFORM™ software is applied to simulate turning operations involving the cast aluminium alloy AlSi9Cu3. Existing experimental turning tests are reviewed and serve as validation of turning simulation.

2 ANALYTICAL MODELLING OF METAL CUTTING

2.1 Introduction

In order to obtain the final shape, most mechanical components undergo machining operations - processes that shape parts by removing unwanted material [1]. Despite being a rather expensive and slow rate process, forging and casting are generally followed by machining to achieve certain shapes, geometrical tolerances and/or appropriate surface quality [2].

Conventional machining continues to occupy a dominant area of all manufacturing operations [3] turning productivity improvement a very desirable goal. Imitating a dynamic process in order to transfer the obtained knowledge to reality is a way of improving efficiency. Machining simulation is nowadays an essential tool when it comes to product quality, cost reduction and overall prediction of metal cutting operations, contributing to a reduction or even elimination of trial and error approaches. Figure 2.1 shows the increasing importance of machining simulation through the number of publications released since 1970 until now. An exponential increase is the observed trend.

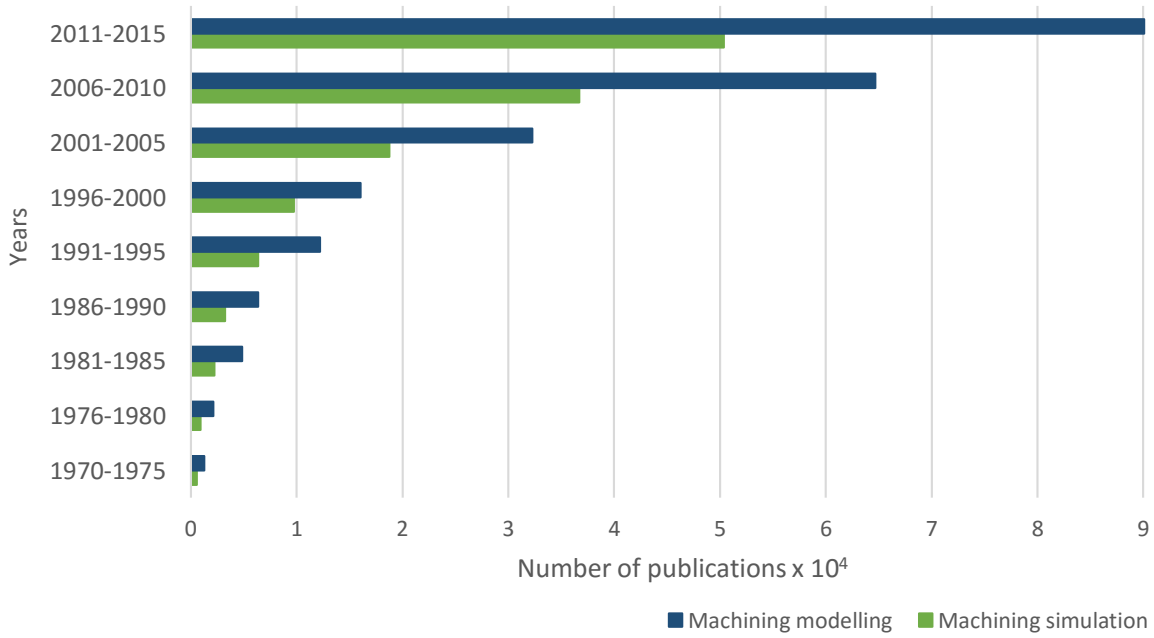

Figure 2.1 – Number of scientific published articles concerning machining simulation and modelling over time

Metal cutting can be described as the formation of chip via the interaction of a tool in the form of a wedge with the surface of the workpiece, given that there is a relative movement between them [1]. Even though all metal-removing operations share the same mechanical principle, geometries and kinematics vary for each machining process. In order to build solid and reliable simulations it is essential to understand this mechanical principle often converted into mechanical, analytical, numerical or even artificial intelligence models.

According to Grzesik, a model can be defined as an abstract system equivalent to the real system with respect to key properties and characteristics, and is used for investigation, calculation and/or explanation of demonstration purposes, which would otherwise be too expensive or not possible. A model allows general statements about elements, structure and behaviour of a section of reality [1], [4]

In this chapter, the most popular metal cutting analytical models, which are often seen as predecessors of numerical models, are going to be briefly reviewed. Listing each model and studying their weaknesses and strengths contributes to a better perception of the variable multitude that is characteristic of machining simulation.

As an interdisciplinary process, it is a good strategy to understand each branch of what can be called the metal cutting simulation tree. A general notion of orthogonal cutting is also presented since it depicts in a direct and broad way the machining principle of conventional machining.

In this dissertation, conventional machining processes (see Figure 2.2) will be considered, in particular turning operations simulation will be the target at the end of this work.

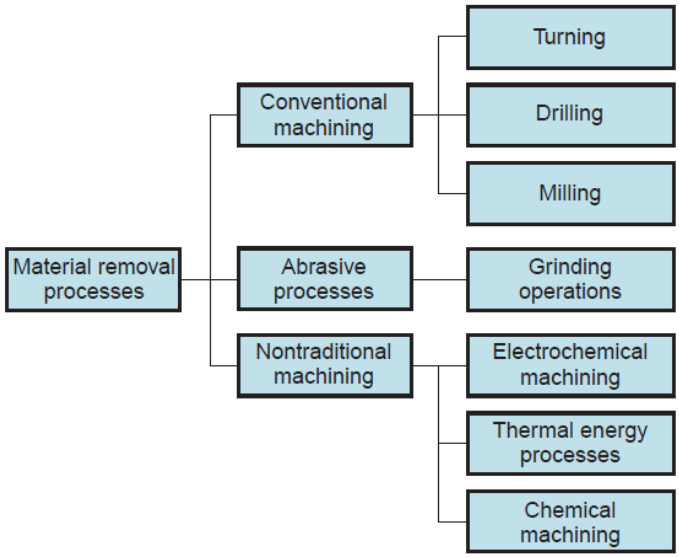

Figure 2.2 – Classification of material removal processes [5]

2.2 Orthogonal and oblique metal cutting

2.2.1 Mechanics of the processes

Orthogonal cutting is the simplest case when it comes to material removing processes. It is widely studied due to its simplicity and it portraits the mechanical principle of machining in two dimensions. Representing a reasonably good approximation in a big diversity of geometrically and physically more complex processes, building FEM models using orthogonal cutting is a big advantage.

In orthogonal cutting, the material is removed by a cutting edge that is perpendicular to the direction of the of relative tool-workpiece motion, as seen in Figure 2.3 [2].

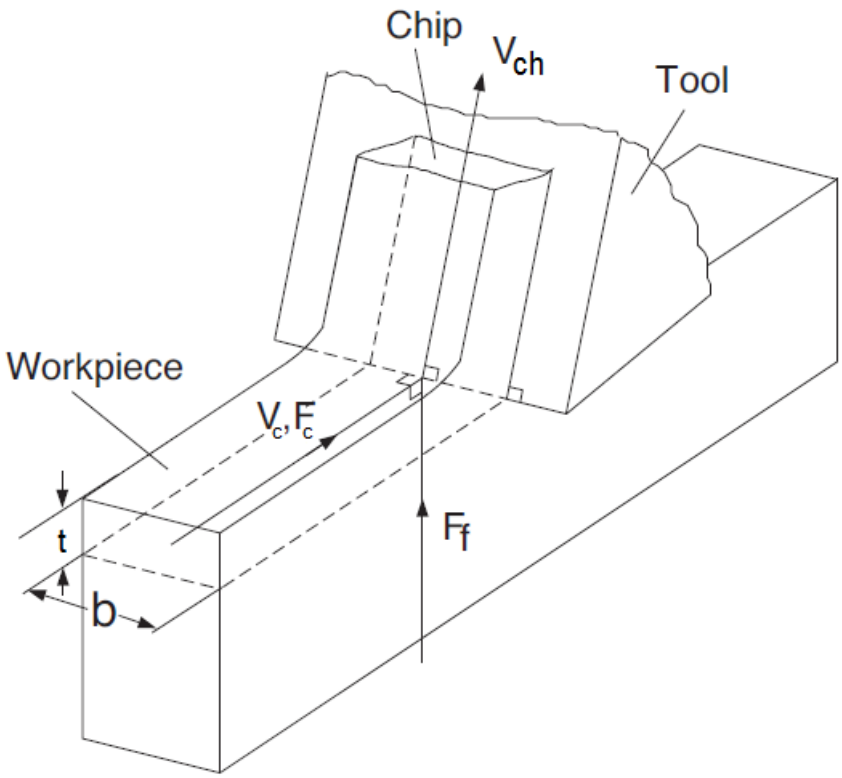

Figure 2.3 – Orthogonal cutting geometry scheme [2]

A metal chip with a width of cut (b) and uncut chip thickness (t) is sheared away from the workpiece, by action of the tool. The cutting is assumed to be uniform along the cutting edge [2]. Since it is a two-dimensional plane strain deformation process without side spreading of the material, the cutting forces are exerted only in the directions of velocity and uncut chip thickness, which are called cutting (F_c) and feed forces (F_f), respectively.

In oblique cutting (see Figure 2.4), the cutting edge is oriented with an inclination angle (λ) and the additional third force acts in the radial direction (F_r) [2]. This inclination allows forces to act in a larger area, which decreases tool wear. However, for analysis and modelling purposes, the complexity when comparing to orthogonal cutting is increased. Even though oblique cutting depicts certain machining processes in a more realistic way, it does not contribute to a significant improvement of metal cutting basic analysis [6].

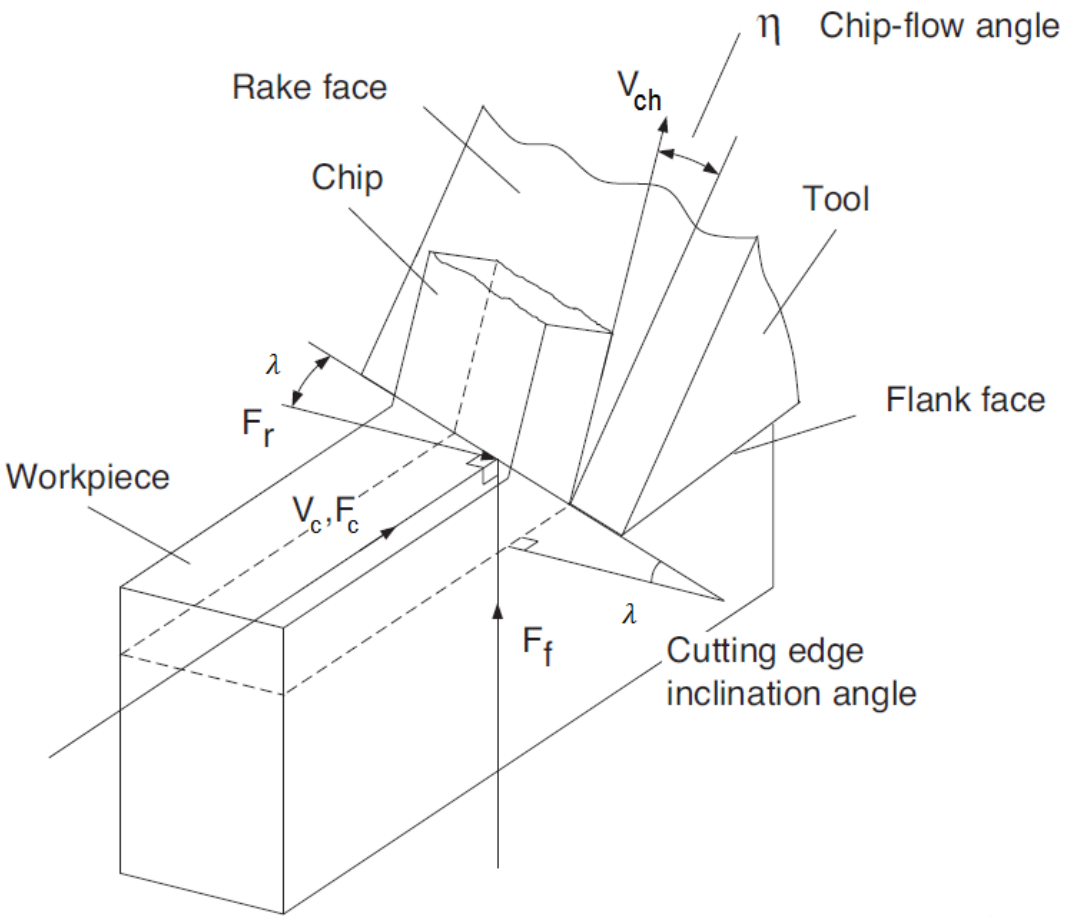

Figure 2.4 – Oblique cutting geometry scheme [2]

There are three regions of interest in the cutting process as shown in the cross-sectional view of the orthogonal cutting of Figure 2.5. As the edge of the tool penetrates into the workpiece, the material ahead of the tool is sheared over the primary shear zone to form a chip. The sheared material, the chip, partially deforms and moves along the rake face of the tool, which is called the secondary shear zone. The friction area where the flank of the tool rubs the newly machined surface, is called the tertiary shear zone [2].

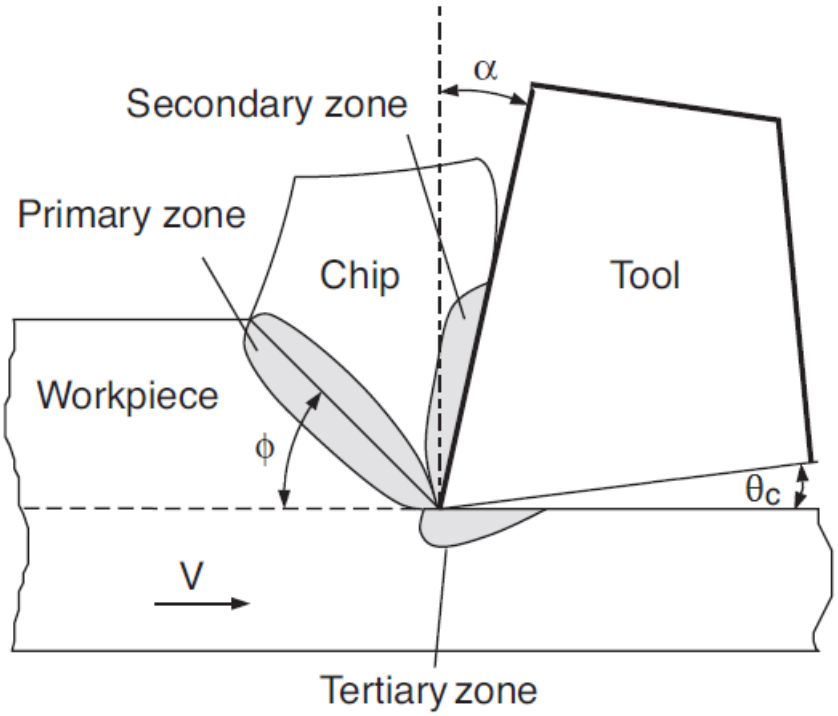

Figure 2.5 – Deformation zones in orthogonal cutting cross-section scheme [2]

The primary zone is where the chip is plastically deformed and, according to a simplified approach, the shear angle (ϕ) defines its inclination. Secondary zone is characterized by a sticking and a sliding region. The sticking region, closer to the edge of the tool, is where the material adheres causing shear stresses on the chip. The sliding region, where the chip slides, is located above the previous region. Primary deformation zone is closely related to severe plastic deformation, while secondary deformation zone to friction.

In orthogonal cutting, there are three important angles to consider: rake angle (α) , clearance angle (θ_c) and the wedge angle (γ_w) [1], [6], [7].

- The rake angle determines the direction of chip flow as it is formed. It can be positive or negative according to its position relatively to vertical dashed line (positive rake angle is represented in Figure 2.5). Tools with positive rake angles are normally used for ductile materials while negative rake angles for high strength materials.
- The clearance angle provides a small clearance between tool flank and newly generated work surface, protecting it from abrasion.
- The angle between rake and flank faces is called the wedge angle and the sum of the three angles is always equal to 90º.

2.2.2 Chip formation analysis

The severe shearing stresses induced by the tool on the workpiece cause the material above the cutting edge to yield and flow plastically in a form of chip. Separation of the chip occurs when ultimate stress of the material is exceeded. The chip, moving upwards the tool rake face, can acquire four different basic geometrical types [8], [9]:

- Continuous;
- Lamellar;
- Segmented;
- Discontinuous.

2.2.2.1 Continuous chip formation

In continuous chip formation the chip slides off along the rake face at a constant speed in a stationary flow [9]. Continuous chips are normally obtained by machining of ductile materials under certain conditions such as low friction between the tool and chip as well as high cutting speeds. High (positive) rake angle, sharp cutting edge and low feed rate also contribute to the formation of this type of chip.

With this type of chip formation, built up edges (BUE) can occur (see Figure 2.6). Built up edge occurs when workpiece material adheres to the tool cutting edge, affecting the chip formation. High temperature and pressure conditions as well as high friction in the tool-chip interface may cause BUE to happen and to grow during the machining process. This negatively affects the surface finish of the machined workpiece.

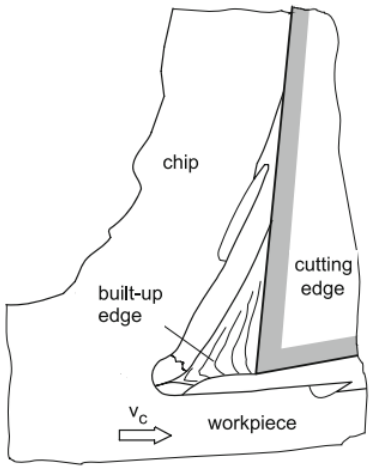

Figure 2.6 – Built up edge formation scheme [9]

Continuous chip formation is normally undesirable since the tool is in contact with the chip for a longer period, resulting in more frictional heat. It is also inconvenient when it comes to handle this type of chip – it may curl around the tool injuring the operator or damaging machine components.

Chip breakers prevent this kind of chip formation (see Figure 2.7). They consist of a typical geometry on tool's rake face that forces the chip to break. This is achieved by putting the chip under additional stress by reducing its radius of curvature.

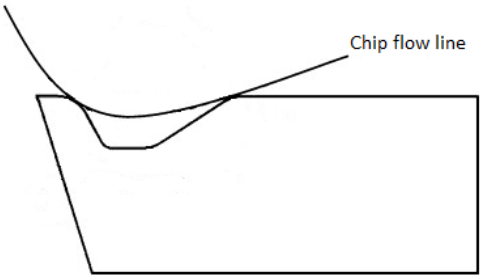

Figure 2.7 – Chip flow line with a chip breaker geometry tool, adapted from [10]

2.2.2.2 Lamellar chip formation

Lamellar chip type corresponds to a cyclical shaped continuous chip. Variations in the deformation process cause more or less significant cleavages [9]. It is frequent to find a wavy shape in this chip type (see Figure 2.8 and Figure 2.9).

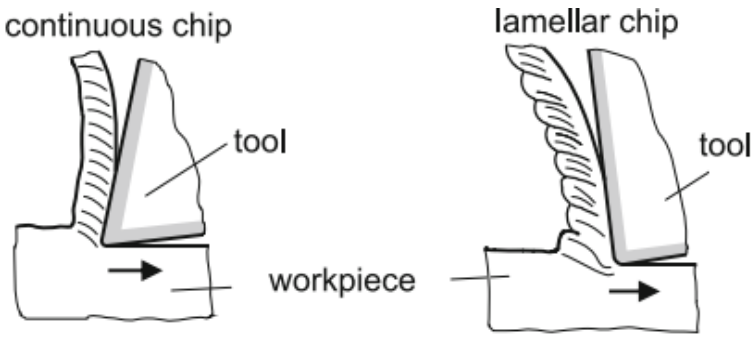

Figure 2.8 – Continuous and lamellar chip formation [9]

Figure 2.9 – Wavy shaped chip example [8]

2.2.2.3 Segmented chip formation

Chips with more or less connected elements with significant variations in the degree of deformation along the flow path are called segmented (see Figure 2.10). These type of chips frequently have a saw-tooth geometry [9]. Negative rake angles, low cutting speeds and high chip thickness contribute to this kind of chip formation.

Figure 2.10 – Scheme [9] and sample of segmented chip formation [8]

2.2.2.4 Discontinuous chip formation

Discontinuous chip type frequently occurs in machining of low ductility materials (see Figure 2.11). Large chip thickness, small rake angle and low cutting speed may also contribute to this type of chip formation. The brittle nature of the material forces the chip fragments to rip out of the workpiece. This has a bigger impact on the surface finish than the actual tool geometry [9].

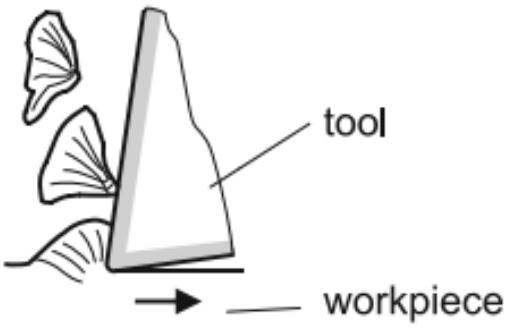

Figure 2.11 – Discontinuous chip formation scheme [9]

2.3 Theoretical modelling of orthogonal cutting

In order to design parts and tools, evaluating equipment suitability and planning of machining processes, it is essential to predict, to a certain level, the forces experienced by the tool and workpiece. It is crucial information when it comes to tool life improvement, power consumption determination and, therefore, efficiency and productivity increase.

It was many researchers' goal to find analytical solutions in order to portrait several areas of machining. The cutting process, friction and heat transfer were extensively studied and different theories were proposed. The wide range of materials, and the conditions intrinsic to machining (high strains, strain rates and temperatures) add to the difficulty in modelling which is reflected by the numerous existent models over the years.

2.3.1 Shear plane models

Ernst and Merchant published the most popular theory supporting this model in 1941. According to their theory, the chip is formed by shear along a single plane (infinitely thin) inclined at an angle ϕ. The chip is assumed to be a rigid body in an equilibrium of forces on the chip-tool interface and across the shear plane. Merchant developed also a circle diagram approach (Figure 2.12) for forces prediction in orthogonal cutting in 1945 [11]–[14]. It allows a fast determination of the several forces experienced by the tool and chip with a good precision and reasonable accuracy [6].

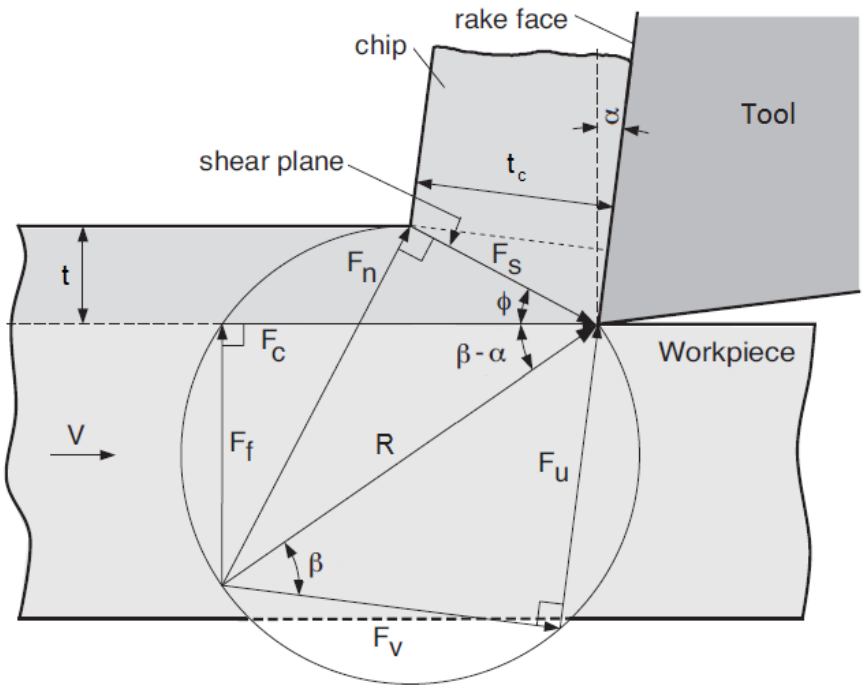

Figure 2.12 – Merchant's forces circle diagram, modified from [2]

It is assumed that [15]:

- The model is a plane-stress problem;
- The material has negligible strain hardening;
- The shear angle is defined by minimization of cutting energy criterion;
- Friction between tool and chip is Coulombian with a fixed friction coefficient;
- There is no variation of the chip width.

According to the model, all cutting forces are due to shearing process or chip–rake face contact. The resultant force $\vec{R}$ applied on the shear plane, over the workpiece is in equilibrium with the force $\vec{R}$ applied on the shear plane, over rake face contact zone. This resultant force is composed by the feed or thrust ($\overrightarrow{F_f}$) and the tangential or cutting ($\overrightarrow{F_c}$) forces. All forces acting on the tool will have equal amplitude but opposite directions with respect to the forces acting on the chip [2].

Feed ($\overrightarrow{F_f}$) and cutting ($\overrightarrow{F_c}$) forces can be decomposed as:

$$F_f = F_n \cos\phi - F_s \sin\phi \quad (1)$$

$$F_c = F_n \sin\phi + F_s \cos\phi \quad (2)$$

On the shear plane, resistance to shear of the metal ($\overrightarrow{F_s}$) and its normal ($\overrightarrow{F_n}$) can be decomposed as:

$$F_s = F_c \cos\phi - F_f \sin\phi \quad (3)$$

$$F_n = F_c \sin\phi + F_f \cos\phi \quad (4)$$

While $\overrightarrow{F_u}$ and $\overrightarrow{F_v}$, can be decomposed as:

$$F_u = F_{tc} sin\ \alpha + F_{fc} \cos\alpha \quad (5)$$

$$F_v = F_{tc} cos\ \alpha - F_{fc} \sin\alpha \quad (6)$$

If feed ($\overrightarrow{F_f}$) and cutting ($\overrightarrow{F_c}$) forces are known, friction coefficient and friction angle will be given as:

$$\mu = \frac{F_u}{F_v} = \frac{F_c \tan\alpha + F_f}{F_c - F_f \tan\alpha} \quad (7)$$

$$\beta = tan^{-1}\mu \quad (8)$$

The average stress on the shear plane area can be depicted as:

$$\tau_s = \frac{F_s}{A_s} \quad (9)$$

A_s, being the shear plane area, is given as:

$$A_s = \frac{bt}{\sin\phi} \quad (10)$$

Where t corresponds to uncut chip thickness and is presented in the cutting ratio equation:

$$r = \frac{uncut\ chip\ thickness}{chip\ thickness\ after\ cut} = \frac{t}{t_c} \quad (11)$$

And ϕ to the mentioned shear angle that can be mathematically defined as:

$$\phi = \frac{r\cos\alpha}{1 - r\sin\alpha} \quad (12)$$

From Eq. 3 and 10, Eq. 9 can now be written as:

$$\tau_s = \frac{F_{tc}\cos\phi - F_{fc}\sin\phi}{bt/\sin\phi} \quad (13)$$

For maximum shear stress, the average stress on the shear plane is differentiated with respect to ϕ:

$$\frac{\partial\tau_s}{\partial\phi} = 0$$

Which leads to,

$$\tan(2\phi)\tan(\beta-\alpha)=1$$

Resulting in the shear plane angle relationship proposed by Merchant:

$$\phi=\frac{\pi}{4}-\frac{1}{2}(\beta-\alpha) \quad (14)$$

Constant friction coefficient assumption and discrepant force and velocity diagrams relatively to experimental data represent the major shortcomings of this model it is still widely used by researchers due to its simplicity. However, a continuous study of the subject resulted in the appearance of new models.

2.3.2 Slip line models

A slip line consists of a boundary between plastically loaded and non-yielded parts of material. In machining, the borders of the primary deformation zone and the chip and the borders between the secondary deformation zone and the chip consist of slip lines [1].

Lee and Shafter, in 1951 [16], by considering that the material had an ideal rigid-plastic behaviour and that the shear plane would be in the maximum shear direction, proposed their shear theory which was the first contribution to the slip-line models. It resulted from an approach to orthogonal cutting with continuous chip with a simplified plasticity analysis.

Their model relies on orthogonal cutting with the following assumptions [17]:

- There is no work-hardening during elastic deformation;
- The material behaviour is independent of deformation rate;
- Temperature rising during deformation is neglected;
- The effect of inertia caused by material acceleration is neglected;

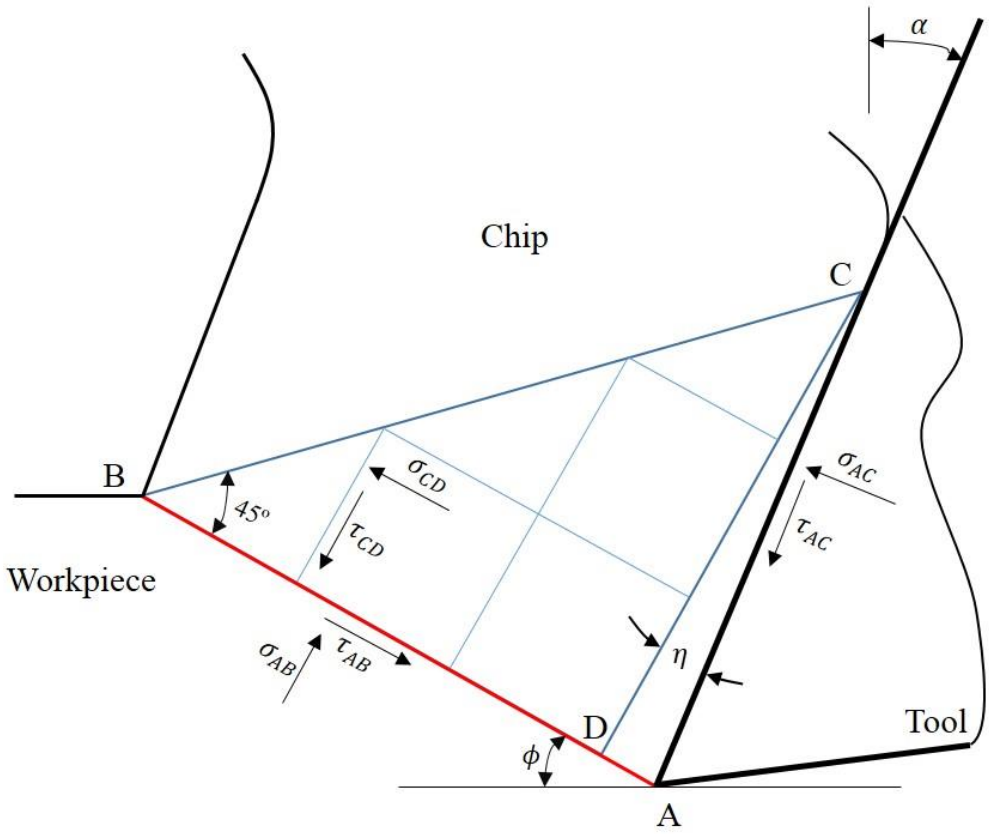

Figure 2.13 – Lee and Shaffer slip-line field scheme, modified from [18]

Cutting forces are transmitted from the shear plane to the chip resulting in the triangular plastic zone ABC (see Figure 2.13). In this region no deformation occurs but the material is stressed to its yield point. Slip line field consists of a set of two types of lines that intersect orthogonally indicating the two orthogonal maximum shear stress directions. The shear plane AB is the lower boundary of the field and indicates one of the directions of slip lines because the maximum shear stress occurs along that plane. BC can be regarded a free surface. Since no forces act on the chip after BC, stresses cannot be transmitted from there.

Since slip lines must intersect free surfaces at angles of 45º, ∠ BAC is equal to $\pi/4$. Assuming that stresses act uniformly at the chip-tool interface, normal stresses will meet the boundary at angles β and $\beta + \pi/2$. Maximum shear stresses are $\pi/4$ to the direction of normal stresses and thus ∠ACB is $\eta = \frac{\pi}{4} - \beta$ [1].

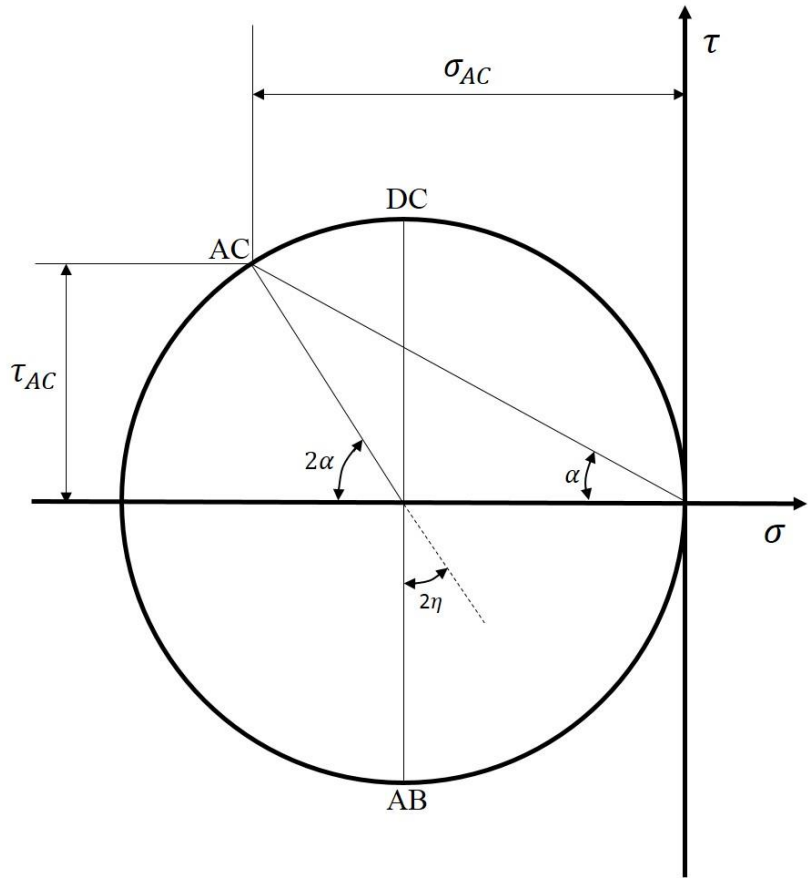

Figure 2.14 - Mohr's circle representing slip line field boundaries, modified from [18]

Using the Mohr's circle (see Figure 2.14), the shear angle is related to the tool rake angle α and friction angle β according to the following equation:

$$\phi = \frac{\pi}{4} - (\beta - \alpha) \quad (15)$$

Even though a new plastic deformation zone theory was proposed, there was still some major shear plane model inherent drawbacks contributing to the inapplicability of the theory in a wide range of cases:

- Infinite stress and strain rate gradient across the shear plane;
- Unrealistic high shear strain that is in contradiction with material testing results;
- Perfectly rigid plastic workpiece material assumption;
- Perfectly sharp tool cutting edge and no contact on the tool flank with the workpiece surface.

2.3.3 Shear zone models

In this type of models, rather than a plane, a shearing region is considered for workpiece deformation (see Figure 2.15). If it is assumed that deformation takes place in a narrow band centred on the shear plane, more general material assumptions can be made. The effects of yield stress varying with strain, strain rate and temperature are considered and simplification of the equilibrium and flow is achieved. Palmer and Oxley [19], Zorev [20] and Okushima and Hitomi [21] were the first developers of this theory.

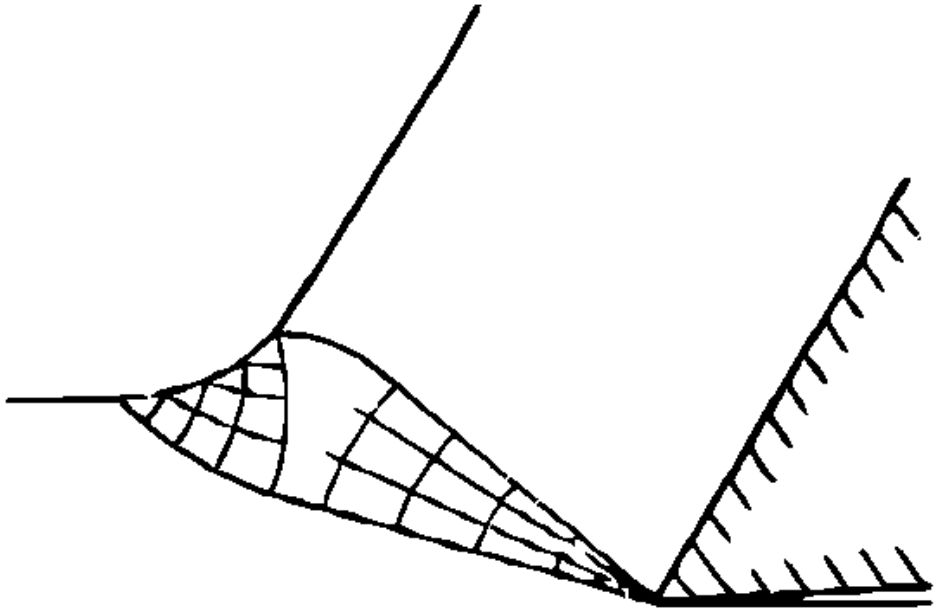

Figure 2.15 - Idealized plastic zone by Palmer and Oxley [19]

Okushima and Hitomi [21] assume that the work material is rigid perfectly plastic. According to Figure 2.16, the stress in the area AOB must be in the yield state and, therefore, the shear stresses on both boundaries must be equal to the yield shear flow stress.

$$\tau_{OA} = \tau_{OB} = \tau_0 \qquad (16)$$

The shear stresses on both boundaries and along the chip-tool interface can be obtained by means of the resultant force on the workpiece side and on the chip side, assuming a uniform distribution of those stresses:

$$\tau_{OA} = \frac{F_c \sin(\phi_1 - \alpha + \beta)}{bt} \quad (17)$$

$$\tau_{OB} = \frac{F_c \cos(\phi_2 - \alpha)\cos(\phi_2 - \alpha + \beta)}{bt_c} \quad (18)$$

$$\tau_{OD} = \frac{F_c \ \sin(\beta)}{bl_c} = \tau_0 \quad (19)$$

Rearranging Eq. 17 to 19 it is possible to obtain the inclination angles of lower and upper boundary regions:

$$\phi_1 = \frac{K_1}{2} - \frac{\beta}{2} + \frac{\alpha}{2} \quad (20)$$

$$\phi_2 = \frac{K_2}{2} - \frac{\beta}{2} + \frac{\alpha}{2} \quad (21)$$

Where K_1 and K_2 are:

$$K_1 = sin^{-1}\left[\frac{2t}{l_c}\sin\beta + \sin(\beta - \alpha)\right] \quad (22)$$

$$K_2 = sin^{-1}\left[\frac{2t}{l_c}\sin\beta + \cos(\beta)\right] \quad (23)$$

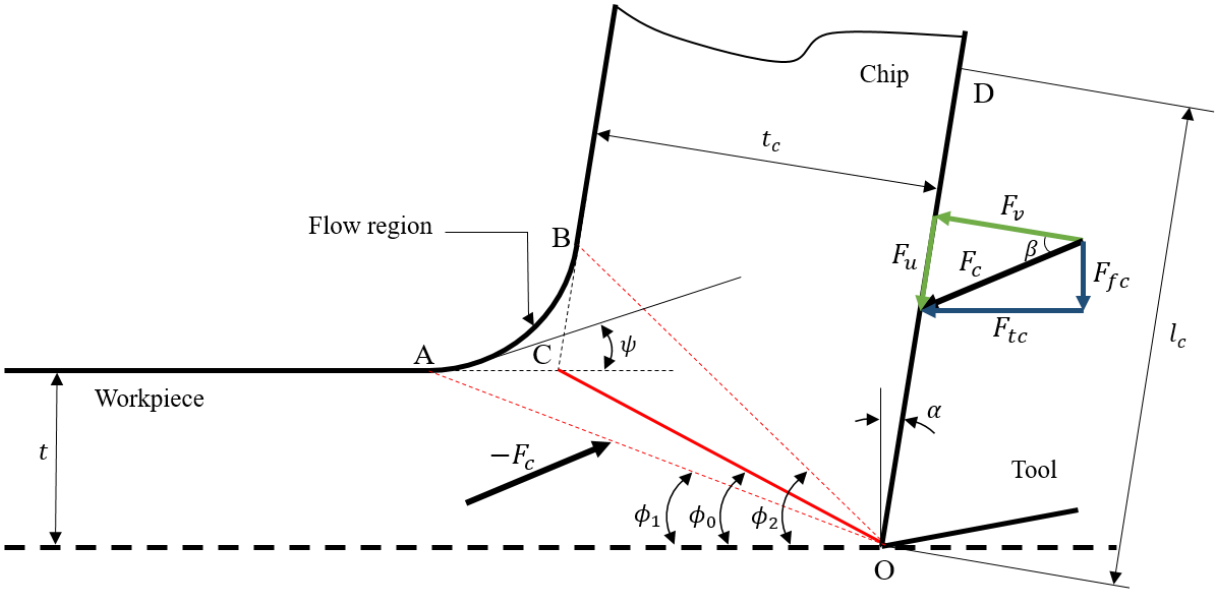

Figure 2.16 - Okushima and Hitomi's shear zone model, adapted from [21]

The most distinguished contribution from Okushima and Hitomi's shear zone model is the gradual change of the shear strain, according to tool rake angle and the average friction angle variation. For a radial plane between OA and OB, the shear strain inside the shear zone at any given transitional line can be expressed as follows:

$$\gamma_i = \cot \phi_i - \cot(\phi_i - \psi_i) \quad (24)$$

Where ϕ_i is the inclination angle of the arbitrary radial plane and ψ_i is the angle formed by the tangential to the point belonging to the plane in the free surface of the flow region.

Considering that plastic deformation is characterized by slip-lines and these should meet the free surface with a 45º angle, Zorev [20] proposed a plastic region characterized by slip-lines as illustrated in Figure 2.17.

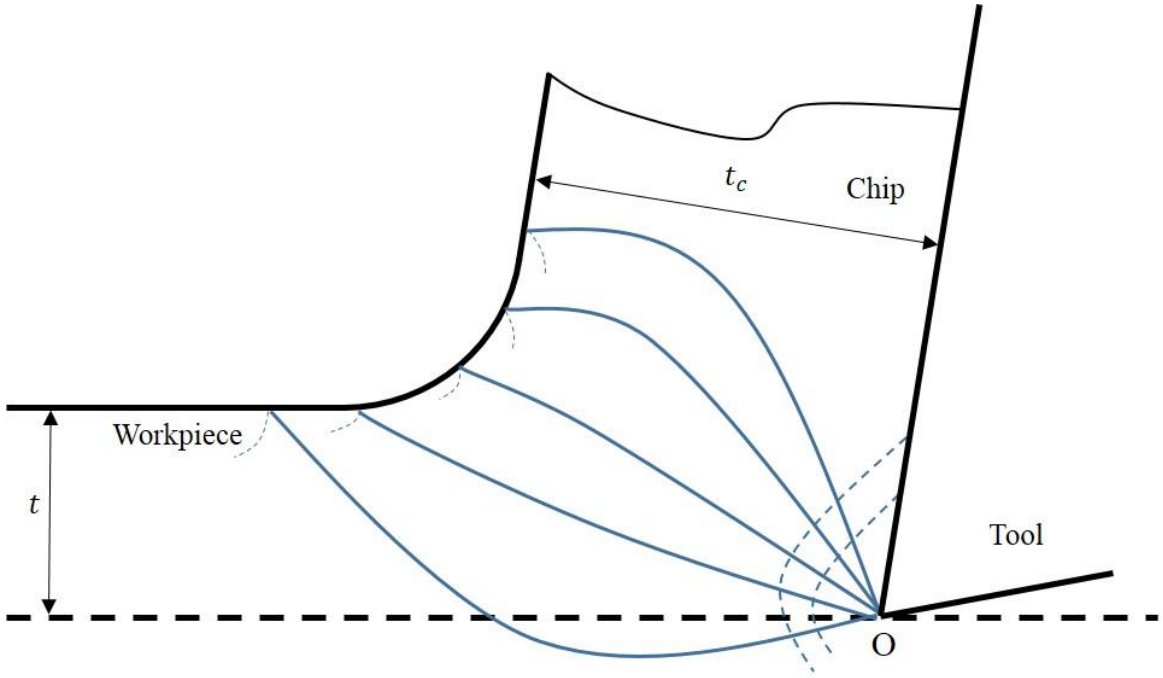

Figure 2.17 - Zorev's qualitative shear zone model, adapted from [1]

Oxley [22], in an attempt to overcome the deficiencies of the existing theories, developed a thermomechanical model, including the effect of work hardening and temperature softening effect of the material. It was also assumed that plastic zone was of considerable width and the streamlines of flow were smooth curves passing from the work to the chip. However, the existence of several parameters contribute to the complexity of the model which leads to a difficult interpretation of some trends of the model [13].

Usui [23]–[25] managed to present a three dimensional similar analysis to the work of Oxley. His analysis included secondary cutting edge as well as nose radius effect. However, similarly to Oxley's model, it is quite complex. It requires stress and strain data at the strain rates and temperatures encountered in metal machining. The lack of these data is a significant drawback. These are the reasons that these models, although more complete than all the others since they include temperature effects and can be used in tool wear and segmented chip formation modeling and are in agreement with experimental data, are not widely used [1].

More recently, A. Moufki et al [13] presented a model that combines a thermomechanical analysis of the material flow within the primary shear zone and a modelling of friction at the tool-chip interface. Coulomb law was used, in which the friction coefficient is a decreasing

function of the temperature. Experimental trends such as the decay of the mean friction coefficient in terms of the cutting velocity, the feeding, and the growth of mean friction coefficient in terms of the rake angle are reproduced by this model.

Table 2.1 – Shear angles according to several authors

Model	**Formula**	**Year**
Ernst-Merchant (shear plane)	$\phi = \frac{\pi}{4} - \frac{1}{2}(\beta - \alpha)$	1941
Stabler (shear plane)	$\phi = \frac{\pi}{4} - \beta - \frac{\alpha}{2}$	1951
Lee-Shaffer (slip-line)	$\phi = \frac{\pi}{4} - (\beta - \alpha)$	1951
Hucks (slip-line)	$\phi = \frac{\pi}{4} - \frac{a\tan(2\mu)}{2} + \alpha$	1951
Shaw et al. (slip-line)	$\phi = \frac{\pi}{4} - (\beta - \alpha) \pm \eta$	1953
Sata (slip-line)	$\phi = \frac{\pi}{4} - \alpha \pm \frac{\alpha - 15^\circ}{2}$	1954
Weisz (slip-line)	$\phi = 54.7^\circ - (\beta - \alpha)$	1957
Kronenberg (shear zone)	$\phi = a\cot\left[\frac{e^{\mu(\frac{\pi}{2}-\alpha)} - \sin\alpha}{\cos\alpha}\right]$	1957
Colding (shear zone)	$\phi = a\tan\left[-\frac{2\left(\frac{F}{H}+2\right)}{\left(\frac{F}{H}+1\right)}\cot(2\Omega) - (\beta - \alpha)\right]$	1958
Oxley (shear zone)	$\phi = a\tan\left[1 + \frac{\pi}{2} - 2\phi + \frac{\cos 2(\phi - \alpha)}{\tan\beta} - \sin 2(\phi - \alpha)\right] - (\beta - \alpha)$	1961
Sata-Yoshikawa (shear zone)	$\phi = a\cot\left[\cot\theta + \frac{\cos\theta}{\sin(\theta + \alpha)}kL\right]$	1963
Zorev (shear plane)	$2\phi_{sp} + \beta - \alpha = \frac{\pi}{2} - \psi_{sp}$	1966
Atkins [26], [27] (shear plane)	$F_c = \left(\frac{\tau_y w\gamma}{Q}\right)t_0 + \frac{R_w}{Q}$, where $Q = [1 - (\sin\beta\sin\phi \,/\, cos\ (\beta - \alpha)\ cos\ (\phi - \alpha))]$	2002

2.3.4 Friction models

Despite being difficult to estimate, friction effect has big influence in orthogonal cutting. It is important in order to determine cutting forces but also tool wear and surface quality. Tool-chip contact length (l_c) as well as friction coefficient depend mainly on cutting speed, feed rate, tool geometry and material properties. It is widely accepted that friction in secondary deformation zone can be represented with a relation between the normal and frictional stress over the tool rake face [28].

According to Zorev (1963), the normal stress is greatest at the tool's cutting edge and gradually decreases to zero at the point where the chip separates from the rake face (see Figure 2.18). Over the length "l_p" of the tool-chip contact area, normal stress is sufficiently high for sticking friction to occur and the frictional shearing stress is equal to the shear strength of workpiece material. Over the remainder of the tool-chip contact area (l_c-l_p) sliding friction occurs and the frictional shearing stress can be calculated using the coefficient of friction, which is constant [2], [28].

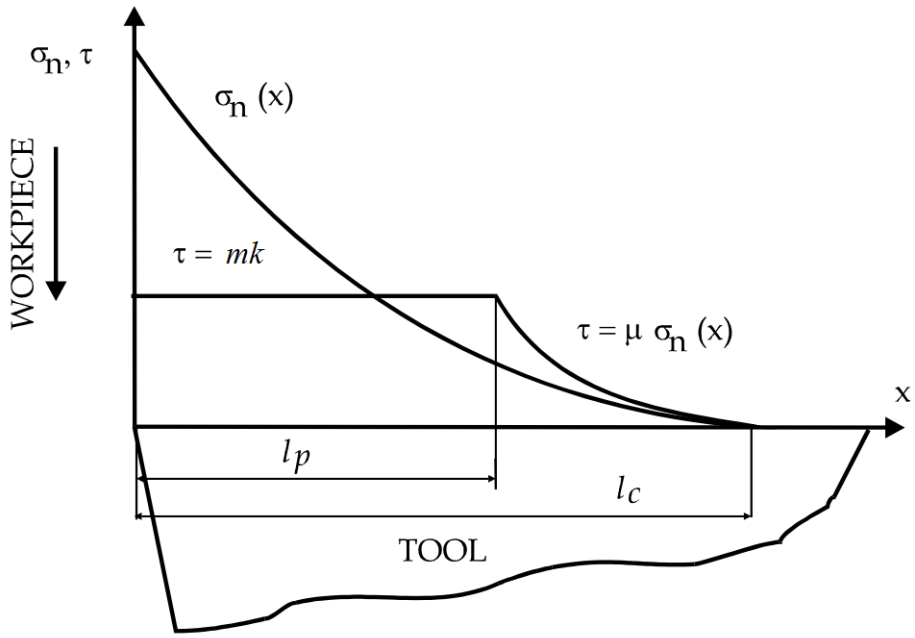

Figure 2.18 – Distribution of normal and shear stress on tool's rake face [28]

Zorev's stick-slip temperature independent friction model can be described as:

$$\tau = \begin{cases} k, & 0 \le l \le l_p \\ \mu\sigma, & l_p \le l \le l_c \end{cases} \quad (25)$$

where k corresponds to the shear flow stress of the work material at the tool-chip interface and μ the fiction coefficient of Coulomb's friction law.

Based on Zorev's model and experimental results, Usui proposed a non-linear stress expression that approaches sticking region part of Eq. 25 for high values of σ and sliding region for low values with a unique relation:

$$\tau = k\left[1 - exp\left(-\frac{\mu\sigma}{k}\right)\right] \quad (26)$$

Table 2.2 – Resume of friction models in metal cutting modelling, adapted from [1]

Model	Equation	Year
Coulomb	$\tau = \mu$	1785
Zorev	$\tau = \begin{cases} k, & 0 \le l \le l_p \\ \mu\sigma, & l_p \le l \le l_c \end{cases}$	1963
Usui	$\tau = k\left[1 - exp\left(-\frac{\mu\sigma}{k}\right)\right]$	1981
Iwata et al.	$\tau = \frac{H_v}{0.07}\tanh\left(\frac{\mu\sigma}{H_v/0.07}\right)$	1984
Childs	$\tau = mk\left[1 - exp\left(-\frac{\mu\sigma}{mk}\right)^n\right]^{1/n}$	1990
Sekhon and Chenot	$\tau = -\alpha K\left\|v_f\right\|^{p-1}v_f$	1993
Yang and Liu	$\tau = \sum_{k=0}^{4}\mu_k\,\sigma^k$	2002

Friction modelling has been subject of research and a big variety of models has been proposed. Table 2.2 chronologically resumes the most important approaches. Material Vickers hardness and relative sliding velocity are two examples of the used criteria.

In order to analyse what could be the most correct approach, the evaluation and comparison between different friction models has been studied by various authors. Özel [28] suggests that tool-chip interface friction modelling has a significant influence in predicting chip geometry, forces, stresses and temperatures and the predictions are clearly found to be most accurate when utilizing friction models based on the measured normal and frictional stresses.

It has also been found that metal cutting under the influence of an oxygen-present atmosphere results in higher friction values, chip compression factors and chip curl radius as well as lower values of the shear plane, which indicates that the surface films formed in freshly cut metal surfaces significantly influence the chip formation [29].

On the implementation of the stick-slip model, Arrazola [30] concluded that a major disadvantage is the uncertainty of the limiting shear stress value.

According to Filice et al. [31], when talking about the conducted experience, main mechanical results (such as forces and contact length) are not very sensitive to the friction modelling. On the other hand, it is observed that friction modelling greatly affects thermal results.

2.3.5 Thermal models

Temperature has a significant effect on the performance of a cutting tool and the quality of the machined component [32] and its determination is essential when it comes to estimate tool wear. The heat generated in metal cutting was one of the first investigated topics in machining [33].

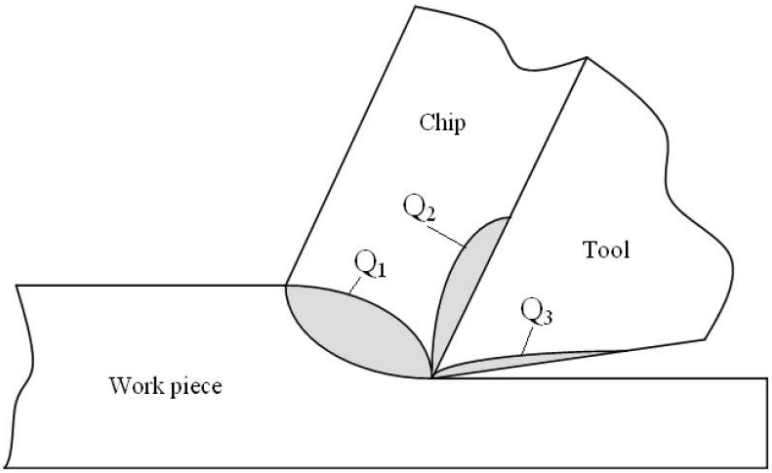

Figure 2.19 – Heat sources in orthogonal cutting process

It is well known that heat in orthogonal cutting is caused by two principal sources: the shear plane heat source (Q_1) and the frictional heat source at the tool-chip interface (Q_2). Some authors mention a third heat source due to the friction between the newly generated surface of the workpiece and the tool's flank face (see Figure 2.19). It is important to note that heat generation is closely related with the effect of both intense plastic deformation and tool-chip friction. However, since the they depend on each other, it makes sense to take in account the combined effect of shear plane and frictional heat sources [34].

Trigger and Chao, in 1951, were the pioneers of metal cutting temperature modelling. They presented an analytical method for the evaluation of the metal cutting temperatures, determined the average chip temperature as it leaves the shear zone by considering the total mechanical energy input as well as the shear energy at the shear plane (see Figure 2.20).
Based on the work of Schmidt and Roubik, who studied the distribution of heat in drilling, they assumed the heat partition into the chip to be 90% and that in the work to be 10%. They also assumed that of the total plastic deformation energy, 12.5% would remain in the deformed chip as latent energy based on the work of Taylor and Quinney.

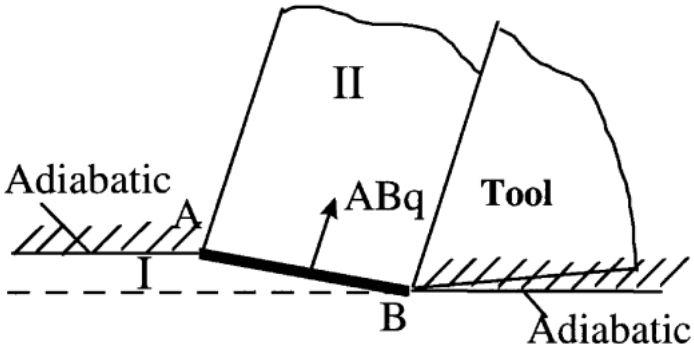

Figure 2.20 - Trigger and Chao analytical model [33]

However, other researchers chose to neglect this part in their analyses as it is considered to be small (or negligible) and unknown. This way, they calculated the average temperature rise of the chip as it leaves the shear plane due to the shear plane heat source using the equation:

$$\bar{\theta}_s = (1 - B)\frac{(F_c V_c - F V_{ch})}{J\ c\rho\ V_c\ tb} \quad (27)$$

where $(1 - B)$ corresponds to the fraction of the shear plane heat conducted into the chip, F_c and V_c to the cutting force and speed, respectively, F to the frictional force at the tool-chip interface, V_{ch} to the chip speed, J is the Joule's mechanical equivalent of heat, c the specific heat and ρ the density.

The term $\bar{\theta}_s\ cp\ V_c\ tw$ is the increment of internal heat energy in the material passing through the shear plane heat source per unit time and $(1 - B)\ F_c V_c - F V_{ch}$ is the sensible heat part of the work done from the shearing process in the shear band per unit time.

Even though Eq. 27 proposed by Trigger and Chao was widely used, the considered heat partition (B) was, by different authors, altered for better estimation of the temperature rise, as shown in Table 2.3.

Table 2.3 – Summary of used equation in heat partition fraction B [33]

Author	Determination of B parameter
Trigger and Chao	$B = 1$
Loewen and Shaw	$(1 - B) = 1/\left(1 + 1.328\sqrt{\frac{a\gamma}{v_c t_c}}\right)$
Leone	$B = 1/\left(1 + 1.13r\sqrt{\frac{Lv_c}{a}}\right)$
Boothroyd	$B = f(N_{th}\tan\phi)^a$

Despite the pioneer studies of Trigger and Chao, that contributed to a widely used model, different models were developed by different authors throughtout time, in an attempt to better define temperature rise in the chip and workpiece caused by the shear plane heat source in machining.

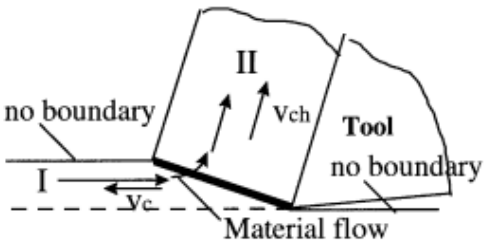

Hahn's model, 1951

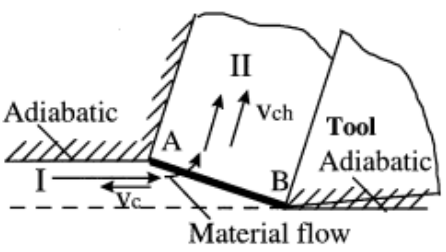

Chao and Trigger's model, 1953

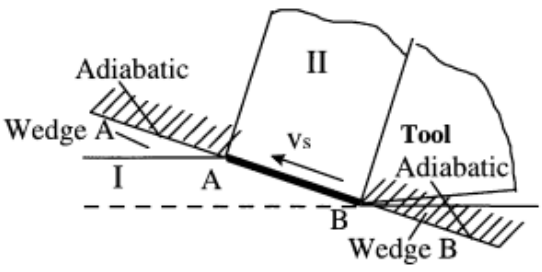

Loewen and Shaw's model, 1954

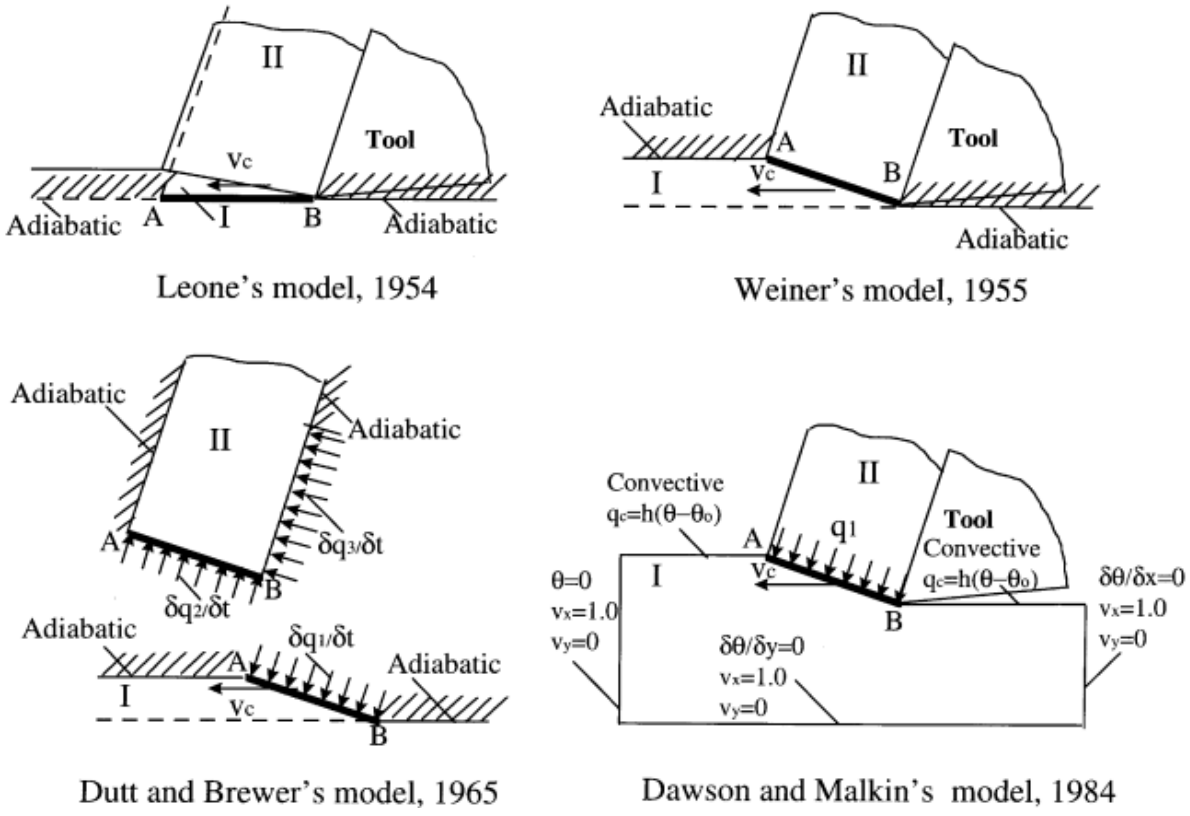

Figure 2.22 – Summary of the models used by various researchers for the determination of temperature rise in the chip and work material [33]

3 SIMULATION OF METAL CUTTING USING FINITE ELEMENT METHOD

3.1 Introduction

Numerous industries require manufacture of parts shaped by removal of unwanted material. Automotive, aeronautics, aerospace, alternative energy, moulds and dies, biomedical industries among others, rely on metal cutting science [35]. In order to develop technological methods, achieve better efficiency and determine the best cutting conditions for a given situation, experimental work is necessary. Due to their expensive and time-consuming nature, analytical methods were developed over the past decades. Because of their rather complex applicability and difficulty to obtain, they can be seen as limited. They were, however, a foundation for numerical models and finite element machining simulation, which constitute nowadays most frequent analysis.

Metal cutting research is also focused on building hybrid models in order to get up to date outputs, relevant to both scientific and technological parts of metal cutting (see Figure 3.1).

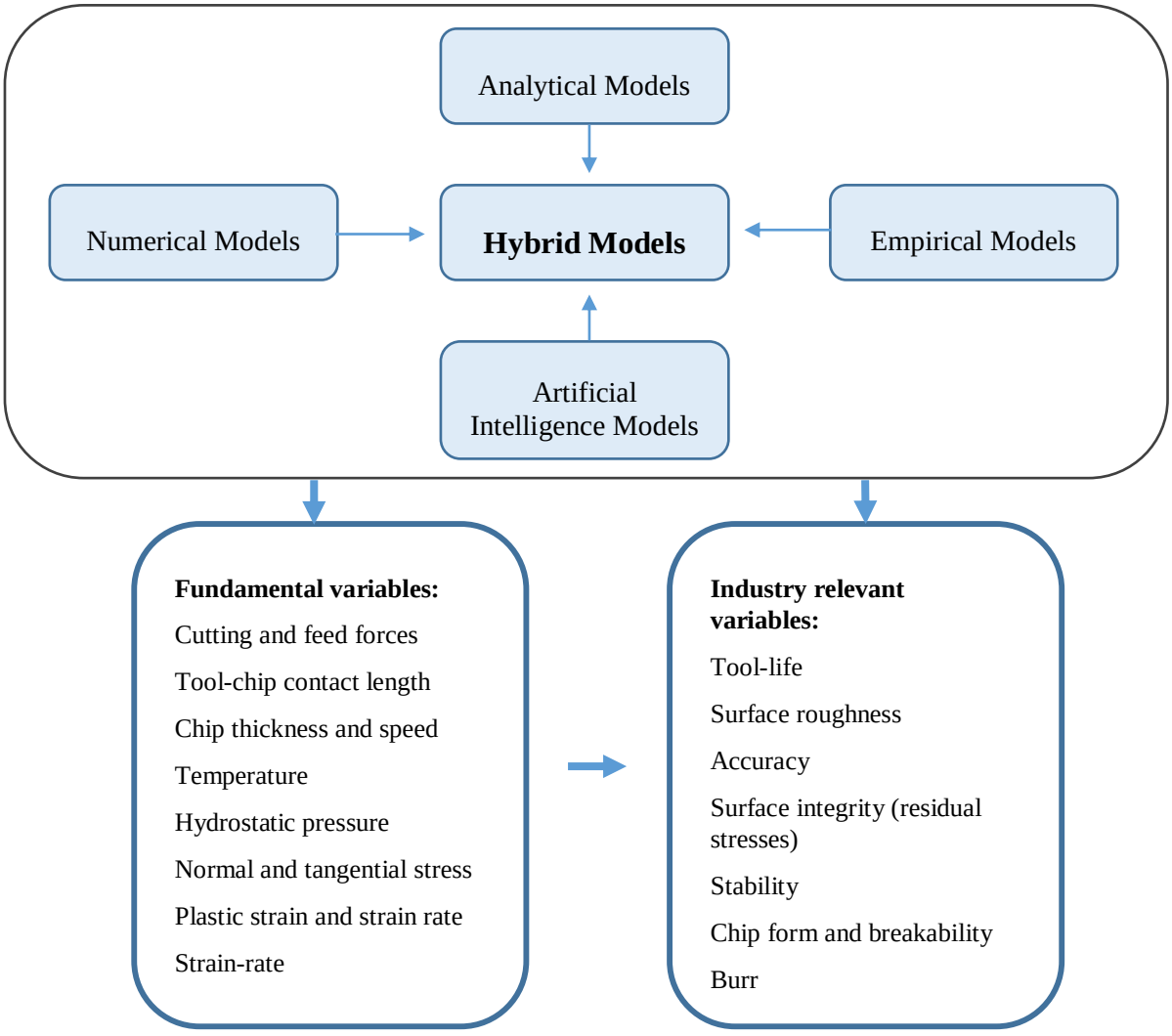

Figure 3.1 – Modelling approach for machining processes [3]

The goal of this chapter is to give an overall review the main aspects related to finite element method numerical simulation of metal cutting. As it was mentioned in chapter 2, metal cutting simulation is characterized by the multitude of variables and can be seen as an interdisciplinary process. Discretization methods, flow stress of workpiece material, friction at tool-chip interface, temperature distribution and damage models are going to be emphasized and, at the same time, capacities and limitations of DEFORM™ 3D/2D software will be discussed.

3.2 Commercial software for machining simulation

When it comes to shaping and finishing metal parts, machining processes are still the most popular manufacturing technique [36], which results in a large effort to develop computational software environments that solve metal cutting problems. Trial and error approaches as well as time and material minimization are some of the benefits. Due to its cost-reducing nature and optimization capabilities both academic research and industry have great interest in machining simulation.

The choice of finite element software for machining analysis is an important factor in determining the quality and scope of analysis that can be performed. DEFORM™ and AdvantEdge™ consist of two examples of commercial software for machining simulation that include machining modules. These have the advantage of quickly setting up models with intuitive and familiar interface. On the other hand, some limitations are imposed and there is no full control of the simulation process. In order to overcome that, there are general purpose commercial software like Abaqus™ that allow minimal restrictions but with less intuitiveness which are better suited for FEM advanced users.

DEFORM™ (Design Environment for Forming), is a commercially available FEM solver that can be applied to several manufacturing processes. Even though its original area of specialty were metal forming operations like forging, it has expanded to include modules that support machining operations. Its major advantages are:

- Allows quick setup of FEM models, more specifically, turning, milling and drilling operations;
- Extensive material library, containing several common materials and alloys;
- Possibility of defining new materials, increasing its applicability;
- Adaptive meshing controls accommodate high workpiece deformations, that are very common in machining.

As for shortcomings:

- Workpiece tends to demand more elements over simulation time, due to mesh regeneration, which causes long computational time;

Abaqus™ is a general purpose FEM simulation software and it does not have any modules for machining operations. Its major advantages are:

- Counts with two different solvers (explicit and implicit), covering a wide range of different simulation possibilities;
- High level of detain in modelling and very fine control over the meshing and element type when building the FEM model;

As for disadvantages:

- Less intuitive interface when compared to software with machining modules;
- No support for any materials, but it allows detailed material edition and configuration;
- Time-consuming modelling;

AdvantEdge™ is a specific software module created by Third Wave Systems for metal cutting operations and allows 2D and 3D simulation. Its advantages are:

- Quick and intuitive modelling;
- Large material library;
- Tool geometry library;

As for disadvantages:

- Very small control over the simulation parameters;
- Even though it allows adaptive mesh, its control is not available;

3.3 Discretization Strategies

There are two primary mathematical formulations of continuum-based FEM: Lagrangian and Eulerian. Lagrangian mesh deforms in time with the material while Eulerian mesh is fixed in space (control volume) [3].

In those analyses, two distinct methods, the implicit and explicit time integration techniques can be utilized. The implicit technique is more applicable to solving linear static problems while explicit method is more suitable for nonlinear dynamic problems.

In order to combine advantages from these two methods, other techniques such as Arbitrary Lagrangian Eulerian and Coupled Lagrangian Eulerian formulations are used in metal cutting finite element simulation.

3.3.1 Lagrangian formulation

In a Lagrangian analysis, a computational mesh is attributed to the workpiece that deforms with the material. The Lagrangian calculation embeds a computational mesh in the material domain and solves for the position of the mesh at discrete points in time [37]. This formulation is widely used in metal cutting simulation due to the possibility of determining chip formation from incipient stage to steady state. Chip geometry depends only on the process parameters and has no predefined geometrical assumptions. This becomes a big advantage when the goal is to study the influence of certain aspects (such as cutting parameters, material and friction models, among others) on the chip's shape.

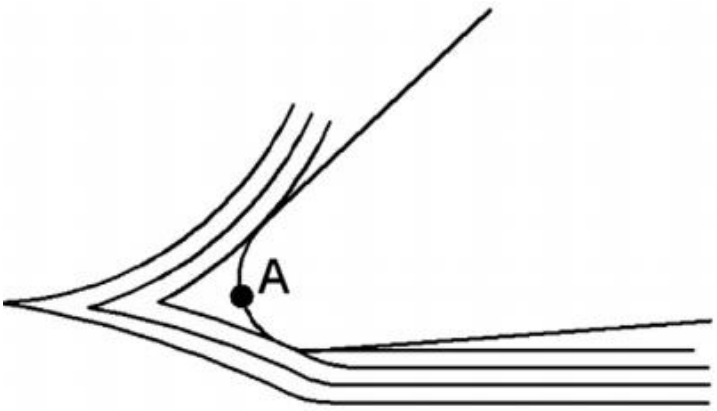

Figure 3.2 – Example of chip separation criterion with material flow lines around stagnation point [38]

In addition to that, it is needed to define a chip separation criterion (see Figure 3.2) that can be based on vicinity of the tool and consequent element separation or material fracture, in order to simulate discontinuous chip formation [39]. Severe plastic deformation is experienced on machining processes. This means element distortion of the computational mesh embedded on the workpiece. Even though mesh regeneration is essential for this type of formulation, it can also be seen as a shortcoming since it slows down computing and decreases the confidence in the results [39].

Updated Lagrangian implicit formulation with automatic meshing regeneration without using chip separation criterion has also been used in simulation of continuous and segmented chip formation in machining processes [40].

3.3.2 Eulerian Formulation

In Eulerian formulation, the mesh is spatially fixed and the material flows through the control volume. A pure Eulerian model can only be used if the machining process is in a steady-state regime [3], [39]. The advantage of using Eulerian formulation is that fewer elements required in modelling the workpiece and the chip, thereby reducing the computation time. There is also no need for mesh regeneration since there is no distortion of the elements. The biggest disadvantage of this approach is the need of determining the final chip geometry and shear angle experimentally prior to the simulation [28] which on the other hand means absence of element separation criteria.

3.3.3 Arbitrary Lagrangian-Eulerian formulation (ALE)

The arbitrary Lagrangian-Eulerian technique combines the unique features of Lagrangian and Eulerian formulations, adopting an explicit solution technique for fast convergence [3]. This code uses an arbitrary formulation on an unstructured mesh, allowing one to designate whether material should flow through a stationary mesh (pure Eulerian), whether the mesh should move with the material (pure Lagrangian), or whether the mesh should be allowed to move independently from the material motion (arbitrary) [41]. It allows a simulation to proceed in Lagrangian formulation until the mesh becomes too highly distorted and mesh regeneration stages are diminished with this technique [37].

- ALE FE model with Eulerian and Lagrangian boundaries:

Even though pre-defined chip geometry is needed in this approach, chip thickness, chip-tool contact surface length as well as workpiece top surface gradually settle to their final shape with the change in deformation conditions as the cutting reaches steady state cutting [30], [37].

The chip and workpiece surfaces are defined with the Lagrangian boundary conditions (blue line) while the chip upper surface and workpiece ends are defined with the Eulerian boundary conditions (pink line) as shown on Figure 3.3.

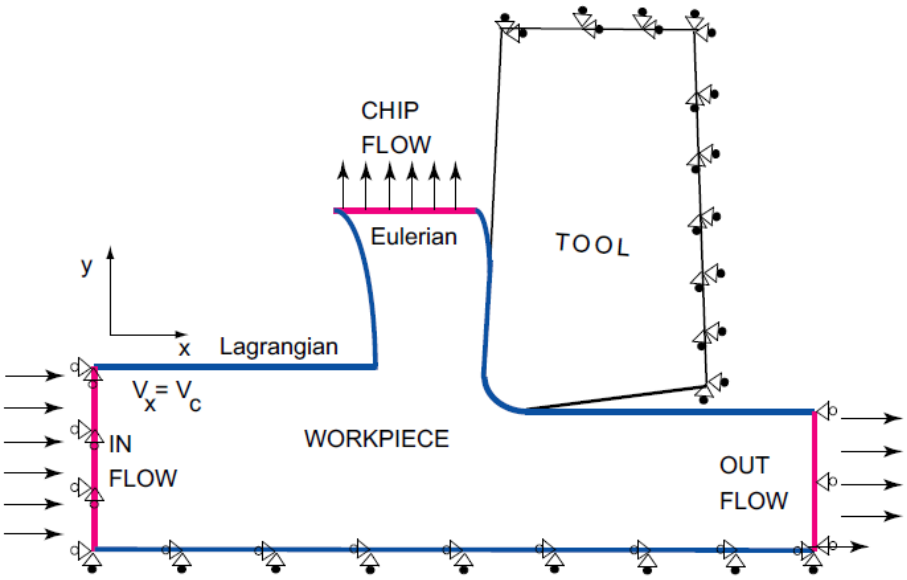

Figure 3.3 – FEM model for ALE formulation with Eulerian and Lagrangian boundary conditions [30]

Noticeable advantages of an ALE model with Eulerian and Lagrangian boundaries are that it allows to model long duration cutting and a refined mesh is easily used in the primary and secondary shear zones [39].

- ALE FE model with pure Lagrangian boundaries (see Figure 3.4):

This model allows simulation of chip formation from the incipient to steady state by performing a large number of small time increments efficiently. The adaptive meshing technique does not alter elements and connectivity of the mesh. This technique combines the features of pure Lagrangian analysis in which the mesh follows the material and Eulerian analysis, when it is needed as part of the adaptive meshing, in which the mesh is fixed spatially and the material flows through the mesh. Due to the relative displacement between the mesh and the material, an ALE model with pure Lagrangian boundaries does not lead to a chip geometry close to the experimental one when segmented chip is observed, contrary to a Lagrangian model [39].

It is very important that the intensity, frequency and sweeping of adaptive meshing are adjusted to the most optimum setting for maintaining a successful mesh during the simulation of the orthogonal cutting process [30].

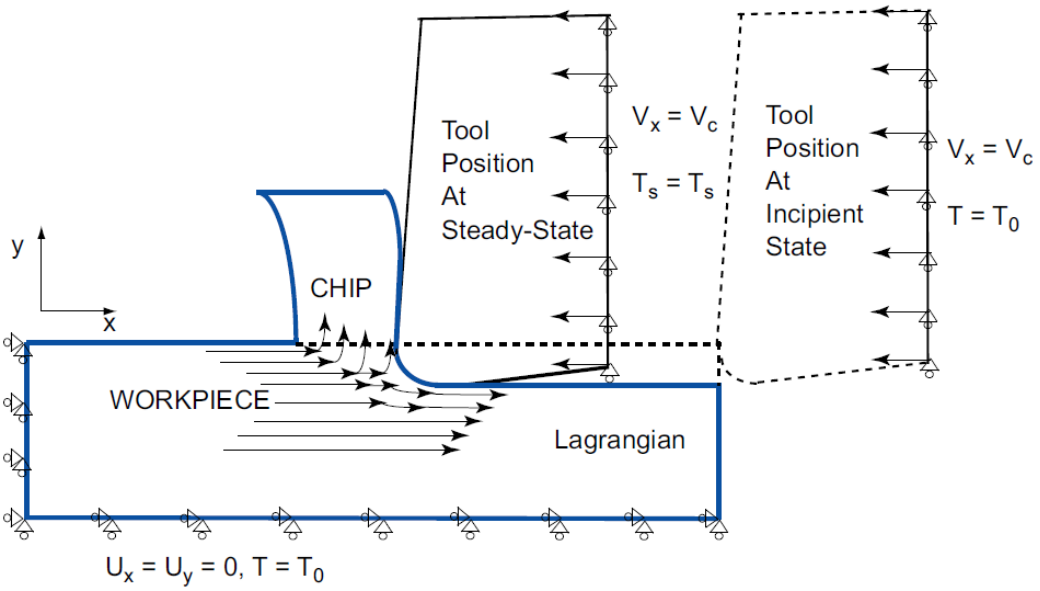

Figure 3.4 – FEM model for ALE formulation with pure Lagrangian boundary conditions [30]

3.3.4 Coupled Lagrangian-Eulerian formulation (CEL)

This method has recently been applied to orthogonal cutting and the comparison with experimental results and an Arbitrary Lagrangian-Eulerian (ALE) model with pure Lagrangian boundaries shows that the chip morphology and the cutting forces are well predicted by this new model. Workpiece is described by the Eulerian formulation and the tool by Lagrangian formulation. Model is composed of a Eulerian mesh representing the volume in which the Eulerian material "flows" and interacts with Lagrangian part(s).

The absence of element deformation in the workpiece, thanks to the Eulerian formulation is a significant advantage of the method. It can lead to a smaller computing time than with ALE model because of the absence of stable time increment decrease due to the mesh deformation and consequent regeneration [39]. This also increases confidence in the results given by the CEL model and opens new possibilities in the modelling of metal cutting.

DEFORM™ 2D/3D is based on an implicit integration method and uses incremental Lagrangian discretization method with adaptive mesh regeneration technique in order to reduce mesh distortion on chip formation.

3.3.5 Meshfree formulation

Large deformation and the consequent high distortion of the mesh can lead to numerical difficulties and premature end of the simulation. Even though mesh regeneration battles these difficulties, it does not always arrive to a stable solution. Another frequent issue is the material separation: the necessity of a mesh separation criterion often leads to approaches that imprecisely predefine part of the solution.

Meshfree solution methods discretize the continuum with a finite number of points or nodes. Since these nodes are not arranged in a rigid grid, meshfree methods offer a bigger flexibility for the simulation of large material deformation and separation. However, only a few meshfree methods have been used so far for the simulation of manufacturing processes being Finite Pointset Method (FPM) one of the used methods. As each particle in a FPM simulation has a higher number of local neighbours than a node in a FEM simulation, the computational effort is generally higher in a FPM simulation [42]. Figure 3.5 shows an example of orthogonal cutting simulation using FPM.

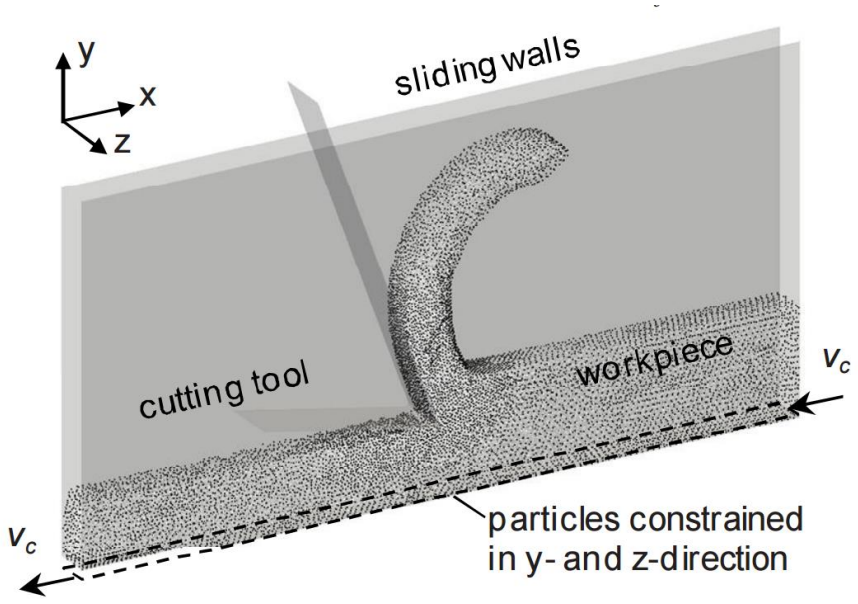

Figure 3.5 – Finite Pointset Method (FPM) for 2D orthogonal cutting [42]

3.4 Material Constitutive Models

In order to be successful, a material constitutive model needs to be reliable and mathematically simple. Metal cutting simulation requires a plastic model, with the J2 plasticity being a very common approach. The isotropic constitutive yield surface is normally assumed, requiring hardening of the flow stress definition. Several flow stress rules are available in the literature for the purpose of metal cutting simulation. The flow stress can also be understood as the instantaneous yield strength at which work material starts to plastically deform or flow; the elastic strains are much lower than plastic strains in metal cutting and so workpiece material flows plastically into the cutting zone [1]. Reliability depends on accurate mechanical and thermo-physical parameter identification. The difficulty in recreating the same conditions of machining operations can lead to modelling limitations. In the following subsections several flow stress relations are presented.

3.4.1 Power law flow stress model

This constitutive model assumes a power law relation to determine flow stress as a function of strain, strain rate and temperature. The experimentally determined exponents are n, m and τ corresponding to strain, strain rate and temperature sensitivity, respectively [3].

$$\overline{\sigma} = \sigma_0 \left(\frac{\overline{\varepsilon}}{\overline{\varepsilon}_0}\right)^n \left(\frac{\dot{\overline{\varepsilon}}}{\dot{\overline{\varepsilon}}_0}\right)^m \left(\frac{T}{T_0}\right)^\tau \quad (28)$$

3.4.2 Oxley's constitutive flow stress model

Oxley proposed that flow stress can be expressed as a work-hardening behaviour Eq. 29 where σ_0 and n are written as functions of a velocity modified temperature, in which strain rate and temperature are combined into a single function as given in Eq. 30,

$$\overline{\sigma} = \sigma_0 \overline{\varepsilon}^n \quad (29)$$

$$T_{MOD} = T\left[1 - v log\left(\frac{\dot{\overline{\varepsilon}}}{\dot{\overline{\varepsilon}}_0}\right)\right] \quad (30)$$

where σ_0 is the strength coefficient, n is the strain hardening coefficient, T is the temperature, υ is a workpiece material constant, $\overline{\varepsilon}$ is the strain and $\dot{\overline{\varepsilon}}$ is the strain-rate. This model has been utilized in modelling orthogonal cutting of low and medium carbon steels in conjunction with slip-line field analysis as an analytical solution to predict cutting forces, average strain, strain-rate and temperatures in the primary shear zone [43].

3.4.3 Strain-path dependent flow stress model

This flow stress model proposed by Maekawa et al. (1983) captures the effect of loading history as well as the coupling effect of strain rate and temperature, as show in Eq. 31 where k and m are constants and A, M, N are functions of temperature [44].

$$\overline{\sigma} = A(\,10^{-3}\dot{\overline{\varepsilon}}\,)^{M}\, e^{kT}\left[\int_{T,\overline{\varepsilon}=\dot{\overline{\varepsilon}}} e^{-\frac{kT}{N}}(10^{-3}\dot{\overline{\varepsilon}})^{-m/N}\, d\,\overline{\varepsilon}\right]^{N} \qquad (31)$$

The integral term accounts for the history effects of strain and temperature in relation to strain-rate. In that respect, the model is considered unique to recover history effects of strain and temperature during metal cutting. A shortcoming is the difficulty of applying the model in finite element analysis software without modifications.

Innovative electromagnetic techniques for material characterization taking into account strain loading path has been developed by Silva [45]. This is of big importance experimental results have shown that strain-rate vs. strain loading paths during plastic deformation of metallic materials have a significant influence on the material stress response [46].

3.4.4 Johnson-Cook (J-C) flow stress model

This widely used constitutive model describes the flow stress of the material as a function of strain, strain rate and temperature effects. It was verified using static tensile and torsion tests over a wide range of strain rates as well as dynamic Hopkinson bar tensile tests and Hopkinson bar tests at elevated temperatures [47].

$$\overline{\sigma} = \underbrace{[A + B(\overline{\varepsilon})^{n}]}_{\text{Elasto-Plastic term}} \quad \underbrace{\left[1 + C\, ln\left(\frac{\dot{\overline{\varepsilon}}}{\dot{\overline{\varepsilon}}_0}\right)\right]}_{\text{Viscosity term}} \quad \underbrace{\left[1 - \left(\frac{T - T_{room}}{T_{melt} - T_{room}}\right)^{m}\right]}_{\text{Thermal softening term}} \qquad (32)$$

The equivalent plastic stress ($\overline{\sigma}$) is in function of equivalent plastic strain ($\overline{\varepsilon}$), equivalent plastic strain rate ($\dot{\overline{\varepsilon}}$), equivalent plastic strain rate reference ($\dot{\overline{\varepsilon}}_0$) and temperature ($T$). A, B, C, n and m correspond to constants previously determined based on flow stress data obtained from the mentioned mechanical tests. T_{room} corresponds to the room temperature while T_{melt} to the melting point temperature of the workpiece material. The first term, elasto-plastic, corresponds to the strain hardening of the yield stress. The second term is known as the viscosity term and models the increase of yield stress at high strain rates. The last term is a softening of the yield stress due to local thermal effects.

Even though being the most used and easy to apply constitutive material model in machining simulation [48], there are some limitations:

- Interaction between each influence factor cannot be completely expressed, since the three terms of the equation are independent from each other [49];
- The model is meaningful in certain ranges of strain and strain rate but fails to capture high strain behaviour because the levels of strain, strain rate and temperature achieved with the split Hopkinson pressure bar are lower than those developed during the machining process [48], [50];
- It is not applicable for all materials since some materials exhibit different behaviour [50];
- Inability to predict the flow stress at deformations below room temperature [51];
- It does not capture history effects of load path neither incorporates the material static and dynamic recovery [52].

In order to overcome some of the limitations such as the absence of interaction between terms, multiplicative strain and temperature dependent terms have been introduced and modified versions of Johnson-Cook flow stress model have been suggested [50]:

$$\overline{\sigma} = [A + B(\overline{\varepsilon})^n]\left[1 + C\ ln\left(\frac{\dot{\overline{\varepsilon}}}{\dot{\overline{\varepsilon}}_0}\right)\right]\left[1 - \left(\frac{T - T_{room}}{T_{melt} - T_{room}}\right)^m\right]\left[D + (1 - D)\left[tanh\left(\frac{1}{(\overline{\varepsilon} + p)^r}\right)\right]^s\right] \quad (33)$$

where,

$$D = 1 - \left(\frac{T}{T_{melt}}\right)^d \quad (34)$$

and

$$p = \left(\frac{T}{T_{melt}}\right)^b \quad (35)$$

3.4.5 Zerilli-Armstrong (Z-A) flow stress model

This model is based on dislocation mechanics theory and crystal structure of materials, which play a main role in determining the inelastic behaviour and flow stress under different load conditions. It incorporates the effect of strain hardening, strain rate hardening and thermal softening with reasonable accuracy. Body cubic centered (BCC) and face cubic centered (FCC) lattice structure have distinct formulations in this model, as given in Eq. 36 and 37, respectively.

$$\overline{\sigma} = C_0 + C_1 \exp\left[-C_3 T + C_4 T ln\left(\dot{\overline{\varepsilon}}\right)\right] + C_5(\overline{\varepsilon})^n \qquad \text{(BCC)} \qquad (36)$$

$$\overline{\sigma} = C_0 + C_2(\overline{\varepsilon})^n exp\left[-C_3 T + C_4 T ln\left(\dot{\overline{\varepsilon}}\right)\right] \qquad \text{(FCC)} \qquad (37)$$

The thermal flow stress component, which has the coupling effect of both temperature and strain rate, pertains mainly to the yield stress in BCC metals and to the hardening stress in FCC metals [53]. In these constitutive equations C_0 to C_5 and n are empirical material constants and often determined through experience based methods rather than using computational methods [43]. Zerilli and Armstrong expanded the applicability of their model mostly due to the alpha phased titanium, by developing a newer representation for hexagonal closely packed (HPC) structure.

Even though Z-A model is preferred to J-C model as it considers the coupled effect of strain rate and temperature, it is particularly not suitable to represent the flow behaviour of material at temperatures above $0.6T_m$ and at lower strain rates due to inconsistencies and inaccurate temperature prediction at high temperatures [53], [54] Due to this limitation, a modified constitutive model based on the Zerilli–Armstrong (Z-A) model has been formulated to predict elevated temperature flow behaviour of materials. The modified Z-A model for the prediction of high-temperature flow behaviour of the material is represented as:

$$\overline{\sigma} = \left(C_1 + C_2\overline{\varepsilon}^n\right) exp\left[-\left(C_3 + C_4\overline{\varepsilon}^n\right)T^* + (C_5 + C_6 T^*) ln\left(\frac{\dot{\overline{\varepsilon}}}{\dot{\overline{\varepsilon}}_0}\right)\right] \qquad (38)$$

where $\overline{\sigma}$ is the flow stress, $\overline{\varepsilon}$ is the equivalent plastic strain, $\dot{\overline{\varepsilon}}$ is the strain rate and $\dot{\overline{\varepsilon}}_0$ the reference strain rate, $T^* = (T - T_{ref})$ with T and T_{ref} being the current and reference temperatures and C_1 to C_6 and n are material constants. This modified Z-A equation for prediction of high temperature behaviour of the material considers isotropic hardening, temperature softening, strain rate hardening, and the coupled effects of temperature and strain and of strain rate and temperature on the flow stress.

3.5 Friction Models

Realistic characterisation of the friction interaction between the chip and the tool is at least as important as flow stress characterisation of the work material [1], [55]. Cutting forces, tool wear, surface quality and temperature highly depend on the applied friction model. Friction parameters are, in turn, greatly influenced by cutting parameters and tool geometry (mainly because of the very high normal pressure at the surface).

Friction in the secondary deformation zone, at the interface of the chip and the rake face of the tool is complicated and difficult to estimate [28]. As mentioned in Chapter 2, and according to Zorev, sliding and sticking friction occur on the tool rake face.

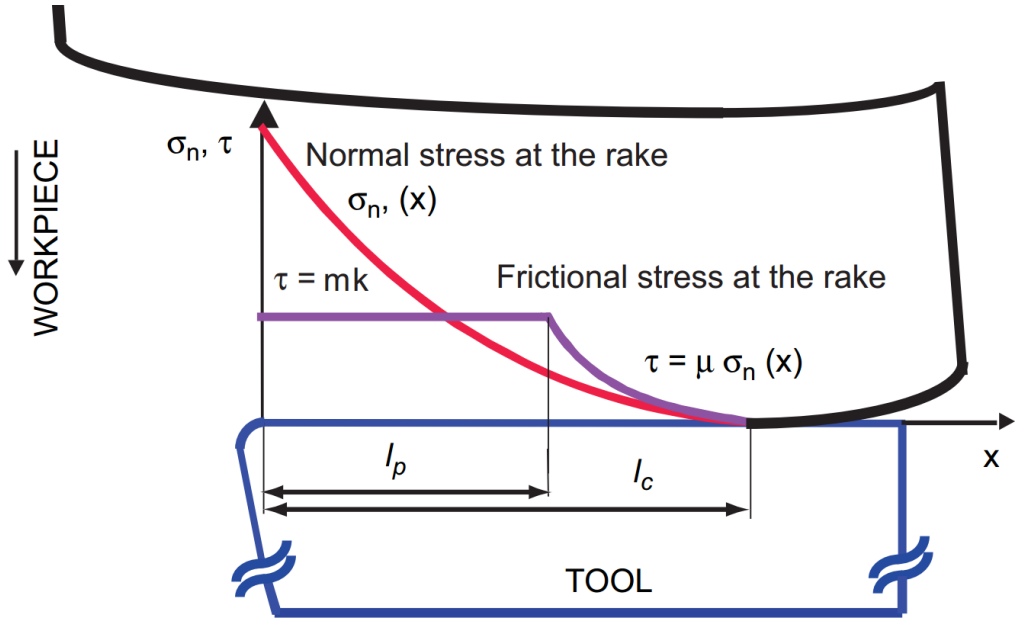

Figure 3.6 – Normal and frictional stress on the tool rake face [30]

The normal stress (σ_n) is greatest at the tool tip and gradually decreases to zero at the point where the chip separates from the rake face (see Figure 3.6). Frictional stress (τ_p) is considered constant in a sticking region (from the tip of the tool up to lp). After this point, frictional stress decreases on the tool rake face in a sliding region.

In finite element method simulation, it is often assumed a classical friction situation following Coulomb's law, where frictional sliding force is proportional to the applied normal load in all the contact length between chip and tool. A shear friction model through all contact zone or a hybrid model that combines both Coulomb and shear friction models are the most popular approaches.

3.5.1 Coulomb model

This friction relation at the tool-chip interface captures the proportional relationship between frictional stress and normal stress along the tool rake face according to the following equation,

$$\tau = \mu\sigma_n \quad (39)$$

where τ is the frictional stress, σ_n the normal stress and μ the friction coefficient. However, as the normal stresses increase and surpass a critical value, this equation fails to give accurate predictions. The full contact zone can be modeled with a constant or variable friction coefficient μ. A variable friction coefficient can be constructed by considering μ as a function of normal stress along the entire tool-chip interface. An example of the evolution of a variable Coulomb friction coefficient (μ) is shown in Figure 3.7.

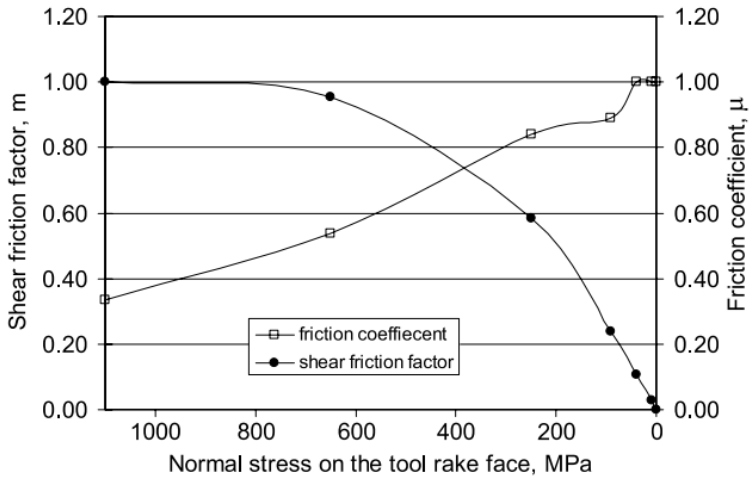

Figure 3.7 – Variable shear friction coefficient, m, and friction coefficient, μ, as functions of normal stress on the tool rake face [28]

3.5.2 Shear model

In this friction type, the workpiece-tool contact is modeled using a shear friction coefficient m, defined the following equation,

$$\tau = mk \quad (40)$$

where k is shear flow stress of the work material at the tool-chip interface. The shear friction coefficient, m, must be estimated as an input into the FE simulations to represent the friction at entire the tool-chip interface. This parameter can be a constant value or variable. In this last case, it is often considered as a function of normal surface pressure along the entire tool-chip

contact. The example of variable shear friction coefficient for low carbon free cutting steel shown in Figure 3.7 is determined based on the empirical model suggested by Dirikolu et al. [55]:

$$m = \frac{\tau_p}{k}\left[1 - \exp\left\{-\left(\frac{\sigma_n}{\tau_p}\right)^n\right\}\right]^{m/n} \quad (41)$$

Coulomb and shear friction models can have a variable coefficient that is dependent of time, temperature, pressure or even a combination of them as well as strain rate or sliding velocity.

3.5.3 Hybrid model

This widely used friction approach consists of applying a combination of shear and Coulomb friction to sticking and sliding region of the tool, respectively. The biggest difficulty that arises with this friction type is defining those regions' boundaries. In order to implement this hybrid friction type with constant or variable friction coefficients for both shear and Coulomb models, the length of lp and lc needs to be estimated from the measured stress distribution on the tool rake face with the purpose of creating two distinct friction regions on tool rake face in the FE simulation. Figure 3.8 shows an example of the relation between measured stress distribution and its distance from the cutting edge. Comparing with the stresses shown in Figure 3.6 , sticking $(0 < x < lp = 0{,}1mm)$ and sliding $(0{,}1mm = lp < x < lc = 0{,}6mm)$ regions can be identified.

It is important to mention that some FEM metal cutting simulation software, such as DEFORM™, allow the possibility of defining a hybrid friction model without defining sticking and sliding regions, which will be automatically identified by the program.

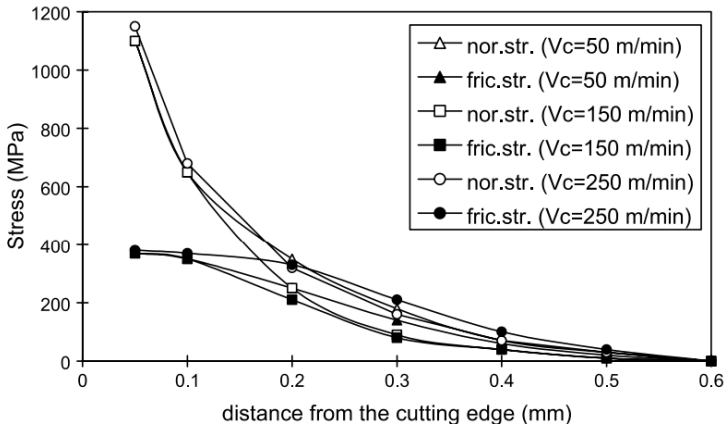

Figure 3.8 – Measured normal and frictional stress distribution on cutting tool rake face in orthogonal cutting of low carbon free-cutting steel [28]

3.6 Damage Models

Metal cutting involves material fracture and, in order to simulate that phenomenon, chip separation and breakage criteria are employed. Chip separation relates to the material failure criterion that allows chip separation from the workpiece while chip breakage concerns the chip release as shown in Figure 3.9.

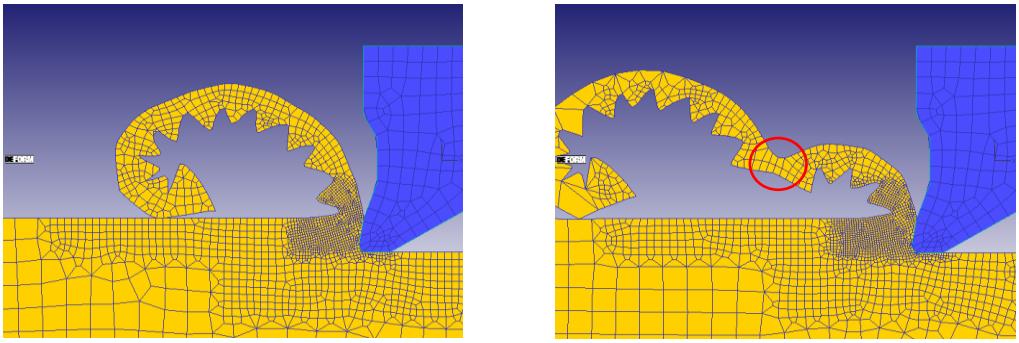

a) b)

Figure 3.9 – Example of chip separation without breakage (a) and with breakage (b)

When it comes to chip separation criteria, these can be divided into two categories [56]:

- Geometrical: Based on the distance D between the tool tip "o" and the node "a" located immediately ahead. Two nodes are assumed to separate when this distance D is less than a critical value;

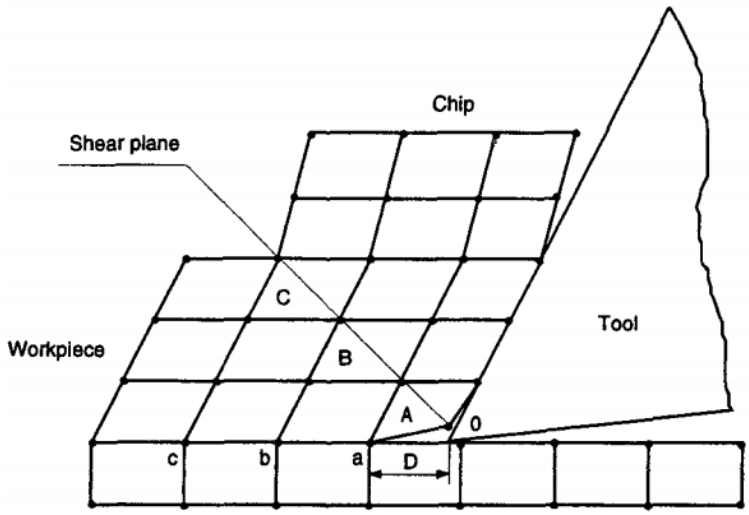

Figure 3.10 – Geometrical chip separation criterion (twin node model) [56]

Even though that ideally chip generation simulation should be achieved by incorporation of real physical models, many researchers support the idea that continuous chip formation in ductile metal cutting involves only plastic deformation [1] which is easily achieved by applying geometrical chip separation criteria without any fracture considerations.

- Physical: based on the values of the selected physical variable, such as the stress, strain, or strain energy, in the element "A" (Figure 3.10) immediately ahead of the tool tip. Two nodes are assumed to separate when the value of the physical variable in the element is larger than the selected threshold value of the material.

Damage can be seen as a decrease of elastic properties of the material as well as stress softening (see Figure 3.11). The initiation of this effect and the way it evolves can be modelled using several damage evolution laws. The ductile fracture mechanism can depend on the single or combined effect of various parameters such as strain and stress intensity, strain rate, temperature and stress triaxiality.

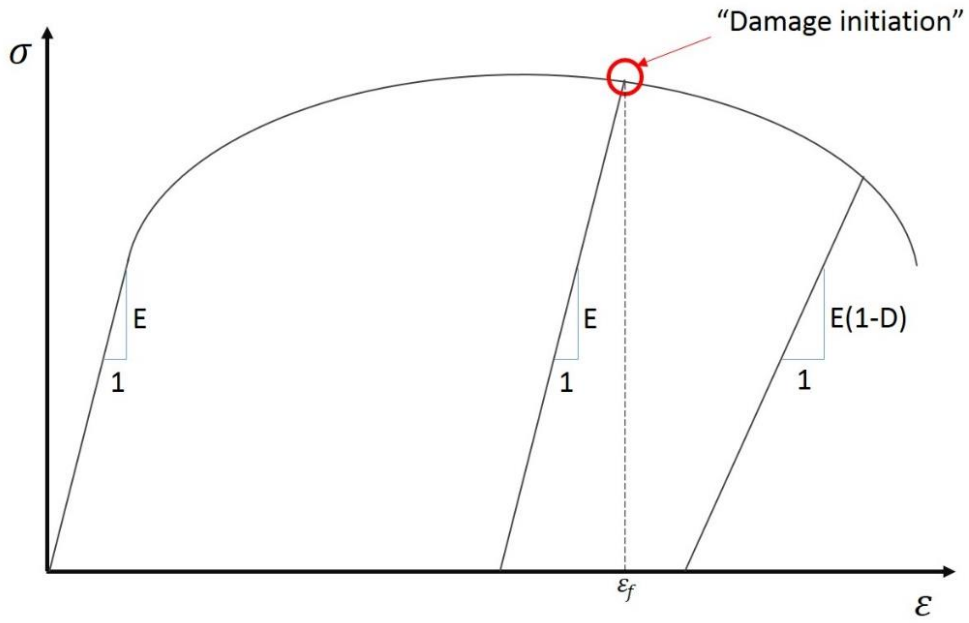

Figure 3.11 – Damage as a material softening process

Large plastic deformation occurs in metal cutting which develops ductile damage process. Even though these two phenomena are different, they influence each other [57]. The combined effect may result in several stages of ductile fracture known as nucleation, growth and coalescence of micro voids.

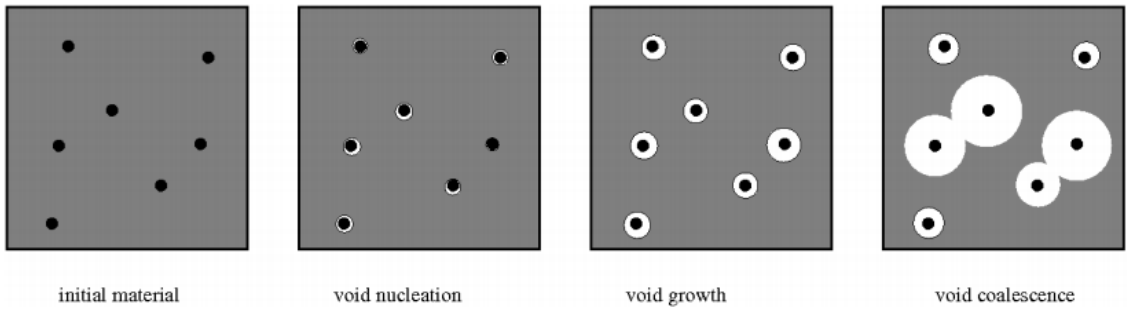

Figure 3.12 - Stages of ductile material damage [58]

Stress triaxiality (η) can be defined as the ratio between mean normal stress (or hydrostatic von Mises stress) and the equivalent stress,

$$\eta = \frac{\sigma_m}{\overline{\sigma}} \quad (42)$$

and according to Bao and Wierzbicki it is, besides the equivalent strain intensity, the most important factor that controls initiation of ductile fracture [59]. Fracture ductility is understood as the ability of a material to accept large amount of deformation without fracture. Equivalent strain to fracture ε_f is a good measurement of fracture ductility.

Studies on the effect of stress triaxiality on fracture ductility for metals were performed with smooth and notched round bar specimens to quantify the effect of stress triaxiality on ductile fracture strain and therefore calibrate the fracture locus in a wide range of stress triaxiality [60]

The Lode angle, θ, is related to the normalized third stress invariant ξ through

$$\xi = \left(\frac{r}{q}\right)^3 = \cos(3\theta) \quad (43)$$

Since the range of the Lode angle is $0 \leq \theta \leq \frac{\pi}{3}$, the range of ξ is $-1 \leq \xi \leq 1$. Furthermore, the Lode angle can be normalized by:

$$\bar{\theta} = 1 - \frac{6\theta}{\pi} = 1 - \frac{2}{\pi}\arccos\xi$$

With a range of $-1 \leq \bar{\theta} \leq 1$, the Lode angle parameter can characterize together with stress triaxiality $(\eta, \bar{\theta})$ all stress conditions. It can be shown that $(\theta = 1)$ corresponds to generalized tension, $(\theta = 0)$ to generalized shear and $(\theta = -1)$ to generalized compression [60], [61].

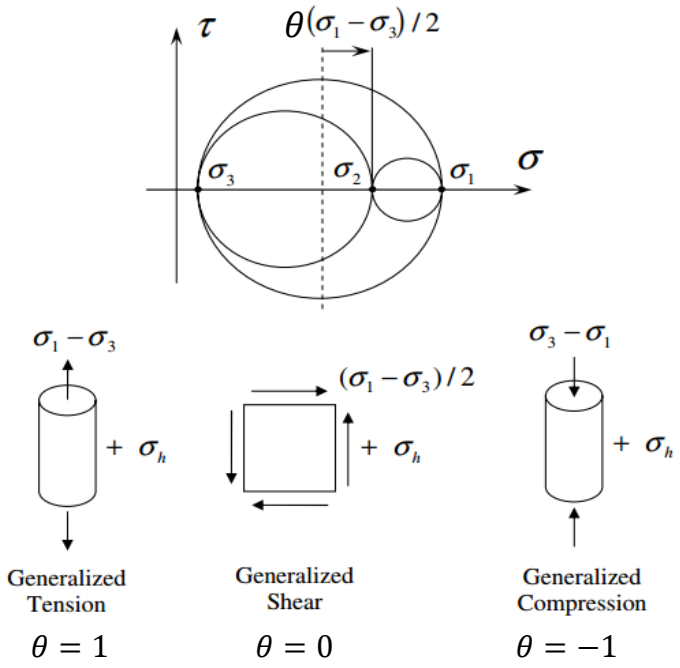

Figure 3.13 – Illustration of the Lode parameter and the three special cases: generalized tension, shear and compression, respectively. Here, σ_h denotes the superimposed hydrostatic stress equal to σ_3 for $\theta = 1$, σ_2 for $\theta = 0$ and σ_1 for $\theta = -1$, respectively [61].

Being a physically complicated process to model, material failure models have drawn the attention of many researchers over past decades and various models have been developed based on different assumptions.

Besides the geometrical and damage approaches for chip separation criteria, some authors have proposed the use of fracture mechanics criteria. This is the case of the works performed by Atkins [27].

3.6.1 Johnson and Cook failure model

This approach is widely used to model ductile failure of materials experiencing large pressures, strain rates and temperatures. Similarly to Johnson and Cook material constitutive model, Eq. 44 consists of 3 independent terms that define dynamic fracture strain: the first term relates to pressure dependence, the second strain-rate dependence and the third, the temperature [62].

$$\varepsilon_f = \left[D_1 + D_2 \exp\left(D_3 \frac{\sigma_m}{\overline{\sigma}}\right)\right]\left[1 + D_4 \ln\frac{\dot{\overline{\varepsilon}}}{\dot{\varepsilon}_0}\right]\left[1 + D_5\left(\frac{T - T_{room}}{T_f - T_{room}}\right)\right] \quad (44)$$

The constants D_1 to D_5 represent the material parameters of the damage law and are obtained from tensile tests. σ_m represents the hydrostatic stress and $\overline{\sigma}$ the von Mises equivalent stress. The rest of parameters have the same meaning as Johnson and Cook material model described in Eq. 32. The damage in a given finite element is defined as:

$$w_d = \sum \frac{\Delta\varepsilon}{\varepsilon_f} \quad (45)$$

where $\Delta\varepsilon$ is the increment of equivalent plastic strain and ε_f is the equivalent strain to fracture, under the current conditions of strain rate, temperature, pressure and equivalent stress.

Eq. 45 is, therefore, a function of strain rate and stress triaxiality coefficient and fracture is initiated when w exceeds 1.

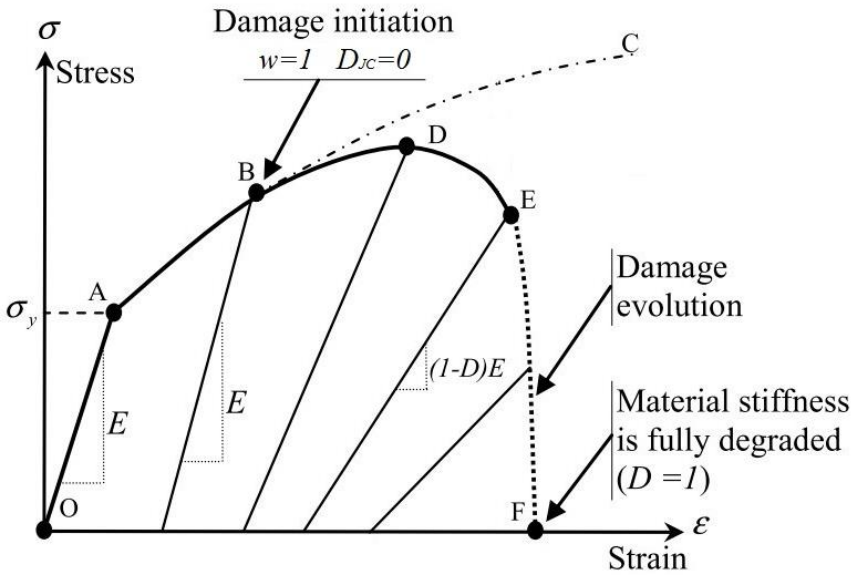

Figure 3.14 – Uniaxial stress-strain curve in the case of a ductile material, modified from [63]

3.6.2 Bao-Wierzbicki failure model

Bao and Wierzbicki fracture criterion states that fracture locus is, in fact, a surface in the space of (ε_f, η, $\bar{\theta}$) rather than a single curve on the plane of (ε_f, η), as shown in Figure 3.15 and Figure 3.16. The dependence of the equivalent strain to fracture on the stress triaxiality is described by an exponential function while the dependence on the Lode angle parameter is taken to be parabolic.

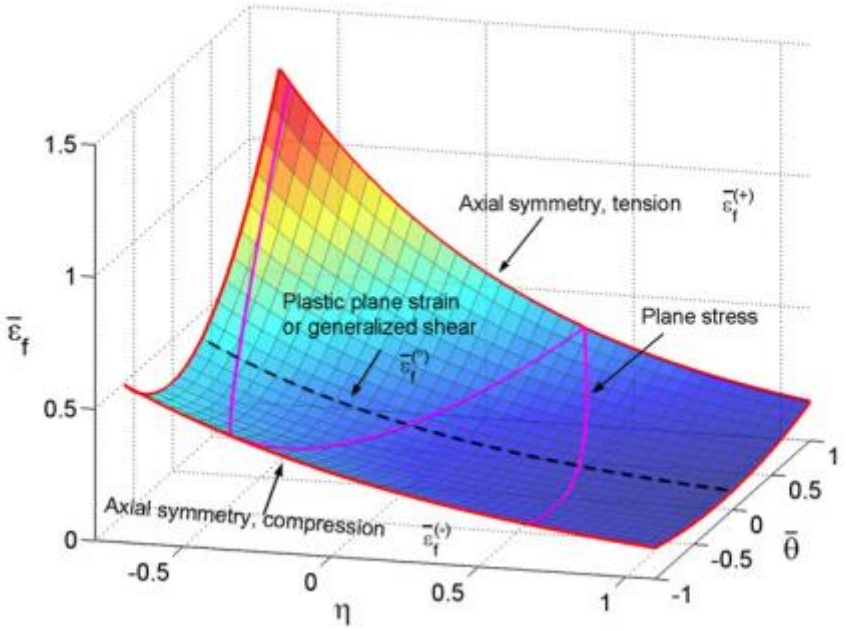

Figure 3.15 – General 3D fracture locus postulated by Bai and Wierzbick [60]

By introducing different types of notches in cylindrical specimens and grooves in flat plate specimens it is possible to characterized different types of stress triaxiality and lode angle parameters that allow the calibration of fracture locus.

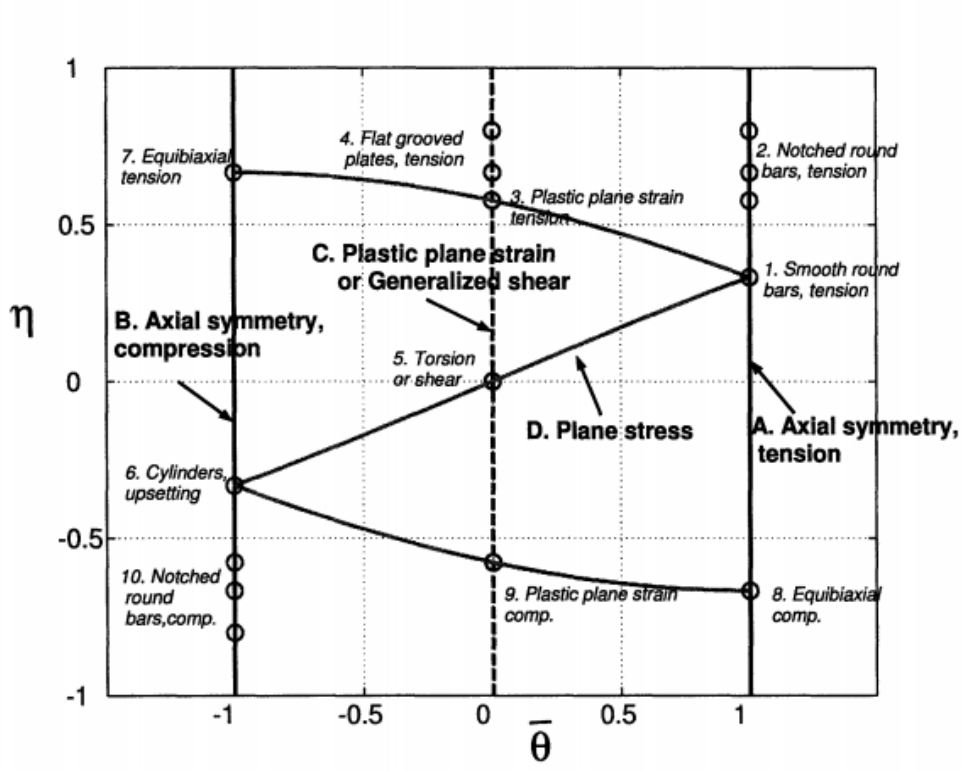

Figure 3.16 - Conceptual representation of the initial stress states on the plane of η and $\bar{\theta}$ [64]

Tests have shown that the effect of the third stress invariant on ductile fracture initiation becomes weak in the high range of pressures or high stress triaxiality region. Fracture locus calibration using "classical specimens" is complicated and time-consuming. Another shortcoming is that the classical specimens correspond all to the limiting cases of loading condition ($\bar{\theta}$ = 0, or $\bar{\theta}$ = ±1)

In order to obtain data points between three limiting cases, other types of specimens with butterfly shape and double curvature have been designed to calibrate the fracture locus in the space of stress triaxiality and equivalent fracture strain (see Figure 3.17).

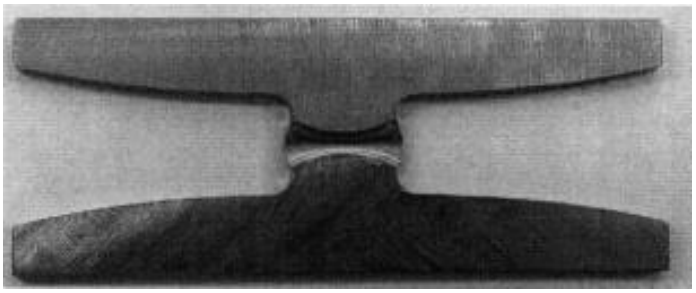

Figure 3.17 - Butterfly shape specimen [64]

3.6.3 Cockroft & Latham failure model

Cockroft and Latham suggested that the critical damage which leads to fracture can be described as the integral of the maximum principal stress with respect to the equivalent plastic strain:

$$D_{CL} = \int_0^{\varepsilon_f} \sigma_1 \, d\overline{\varepsilon} \tag{46}$$

where σ_1 is the maximum principle stress, $\overline{\varepsilon}$ the equivalent strain and ε_f is the equivalent strain at which fracture occurs.

This model was later modified by normalizing the maximum principal stress by the equivalent stress, resulting in:

$$D_{NCL} = \int_0^{\varepsilon_f} \frac{\sigma_1}{\overline{\sigma}} d\overline{\varepsilon} \tag{47}$$

As it is observable Cockroft & Latham fracture model is based on only one constant to indicate the fracture properties of a material. Upsetting, shear or tension tests are available choices for calibration of this method.

3.6.4 McClintock failure model

McClintock [65] analysed the expansion of long cylindrical cavities under a triaxial stress system of fixed orientation, defining the following equation:

$$D_{MC} = \int_0^{\varepsilon_f} \left(\frac{2}{\sqrt{3}(1-n)} \sinh\left(\frac{\sqrt{3}(1-n)}{2} \frac{\sigma_1 + \sigma_3}{\overline{\sigma}} \right) + \frac{\sigma_1 - \sigma_3}{\overline{\sigma}} \right) d\overline{\varepsilon} \tag{48}$$

where σ_1, σ_3, $\overline{\sigma}$, and $\overline{\varepsilon}$ are the maximum principal stress, minimum principal stress, equivalent stress, and equivalent plastic strain, respectively. n is a material constant. This model's range of validity is limited by the hypothesis of constant triaxiality ratio during loading.

3.6.5 Rice & Tracy failure model

This model, often used due to its simplicity and ease of interface with finite element analysis is defined by the following equation

$$D_{RT} = \int_0^{\varepsilon_f} A \exp\left(\frac{3}{2}\frac{\sigma_m}{\overline{\sigma}}\right) d\overline{\varepsilon} \quad (49)$$

where A corresponds to a material constant. The main drawback of this model, similary to McClintock failure model, is that the range of validity is limited by the hypothesis of constant triaxiality ratio during loading [66].

3.6.6 Freudenthal failure model

All the integrated stress–strain criteria based on empirical and semiempirical approach are versions of Freudenthal's critical plastic work per unit of volume:

$$D_F = \int_0^{\varepsilon_f} \overline{\sigma}\ d\overline{\varepsilon} \quad (50)$$

3.6.7 Oyane failure model

A criterion for the ductile fracture of pore-free materials is derived by Oyane (Oyane et al. 1980) from the equations of plasticity theory for porous materials where A consists of a material constant.

$$D_O = \int_0^{\varepsilon_f} \left(1 - \frac{\sigma_m}{A\overline{\sigma}}\right) d\overline{\varepsilon} \quad (51)$$

3.6.8 Brozzo failure model

Explicit dependence of damage on the level of both the largest (tensile) principal stress, σ_1 , and the hydrostatic stress, σ_m , was proposed by Brozzo et al.

$$D_B = \frac{2}{3}\int_0^{\varepsilon_f} \frac{\sigma_1}{\sigma_1 - \sigma_m}\ d\overline{\varepsilon} \quad (52)$$

3.6.9 Ayada failure model

This model, frequently used in blanking and forging, is sensitive to the pressure according to the following relation:

$$D_O = \int_0^{\varepsilon_f} \left(\frac{\sigma_m}{\overline{\sigma}}\right) d\overline{\varepsilon}$$

These laws can be intrinsic to the material model or defined separately (coupled or uncoupled formulations).

4 FEM METAL CUTTING SIMULATION WITH DEFORM™ 2D: SENSITIVITY STUDIES

4.1 Introduction

As a first approach to DEFORM™ 2D/3D it is important to understand the contribution of key parameters of finite element machining simulation. Knowing the influence of each separate factor allows a global comprehension of this software, its potential and limitations. The key parameters can be divided into 3 main groups: numerical, process and material parameters. The conducted sensitivity analysis extends to these three.

The chosen process parameters to test were cutting speed, feed rate, tool geometry (rake angle and cutting edge), friction and heat transfer coefficients. When it comes to numerical parameters, mesh element size, iteration method as well as solver were taken into consideration. In order to understand the influence of the material parameters, this analysis was extended to 3 different workpiece metals from the software's material library: aluminium alloy Al7075 – T351, stainless steel AISI316L and titanium alloy Ti6Al4V. 2D metal cutting simulations were performed which allowed depicting the orthogonal cutting process. This option became appropriate to reduce the computational times that this kind of study generally requires. The simulations were performed from an initial stage of chip initiation transient process until a stabilized/steady-state chip formation.

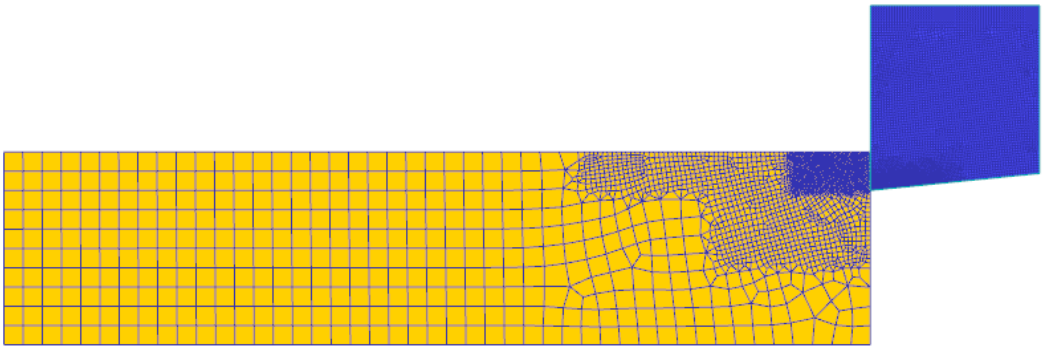

Figure 4.1 – Scheme of two-dimensional setup of orthogonal cutting simulation

4.2 Materials characterization according to DEFORM™ library database

The material component of this sensitivity analysis was achieved by using three different materials. By default, the flow stress of library materials of DEFORM™ software are defined by a function of temperature, strain and strain-rate, in form of tables.

$$\overline{\sigma} = \overline{\sigma}(\overline{\varepsilon}, \dot{\overline{\varepsilon}}, T)$$

Adidtionaly, and for each material, elastic properties (such as Young modulus and Poisson's coefficient) and thermal (such as thermal conductivity and heat capacity) are also defined by default. When it comes to damage model, Normalised Cockroft and Latham is the default model. However, very few materials are characterized regarding this parameter. Titanium alloy Ti6Al4V is one of those materials. Due to its very complete characterization on the software's library, it was one of the chosen materials for this sensitivity analysis.

In order to cover a considerable range of materials an aluminium alloy and a stainless steel were selected. To understand the influence of flow stress characterization, a less characterized material (meaning less flow stress values for less strain, temperature and strain-rate condition) was chosen (Al7075-T351) as well as an intermediately characterized material, Stainless steel AISI316L.

The flow stress curves dependent on temperature and strain rate are shown. These curves were built from the tables that relate flow stress with strain for independent conditions of strain-rates and temperatures in the material library of the software.

4.2.1 Aluminium alloy Al7075 – T351

This aluminium alloy, known for its high mechanical resistance, low density and good fatigue strength, is typically applied used in transportation applications, including marine, aviation and automotive.

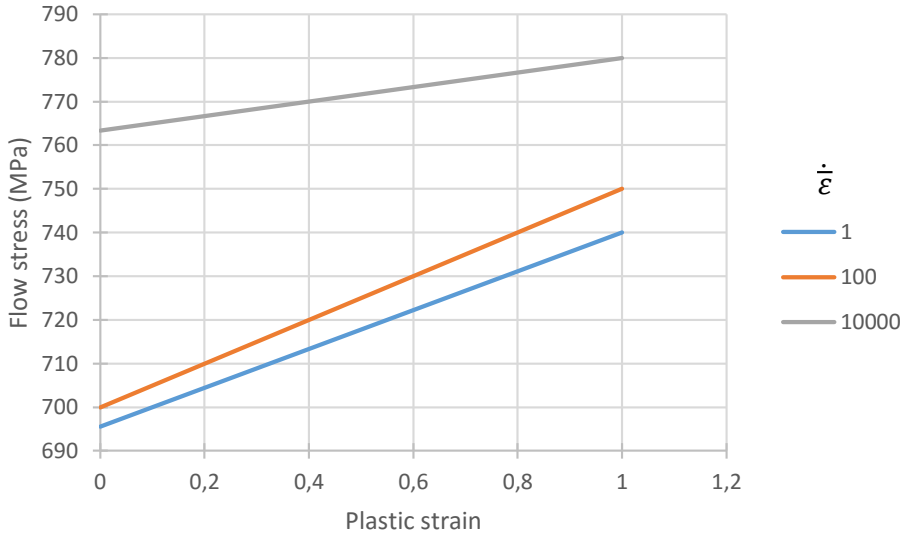

Figure 4.2 - Flow stress vs. strain curves of Al7075-T351 for different strain rates and a fixed temperature of 20ºC

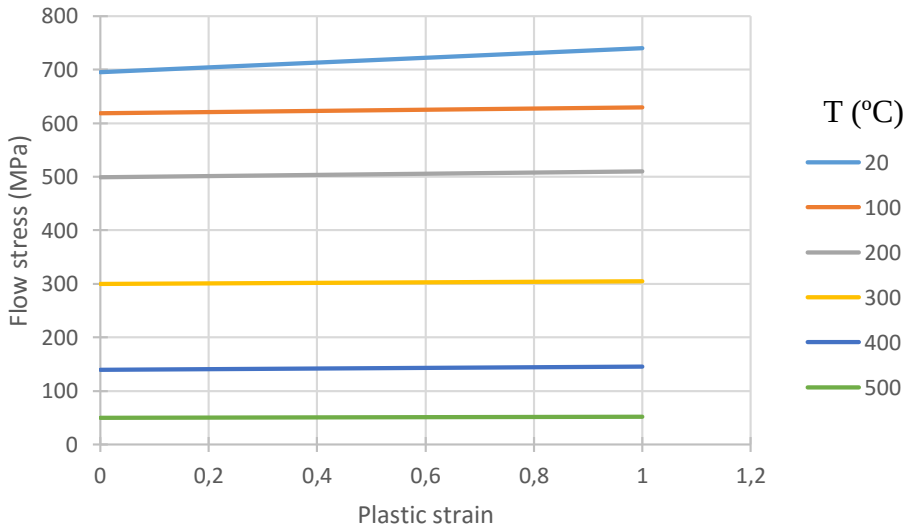

Figure 4.3 - Flow stress vs. strain curves of Al7075-T351 for different temperatures and a fixed strain rate of 1

4.2.2 Stainless steel AISI 316 L

This material is known for its high corrosion resistance. It has a low carbon grade, which makes it easier to machine comparing to other stainless steels. Its main applications are marine, architectural, medical and pharmaceutical, and in the fabrication of reactor pressure vessels and boiling water reactors, when it comes to nuclear energy field applications [67].

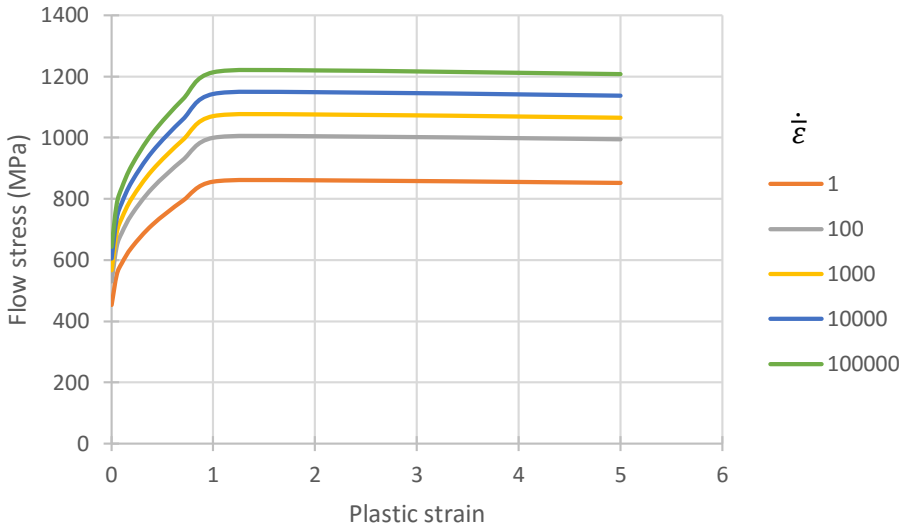

Figure 4.5 – Flow stress vs. strain curves of AISI 316 L for different strain rates and a fixed temperature of 20ºC

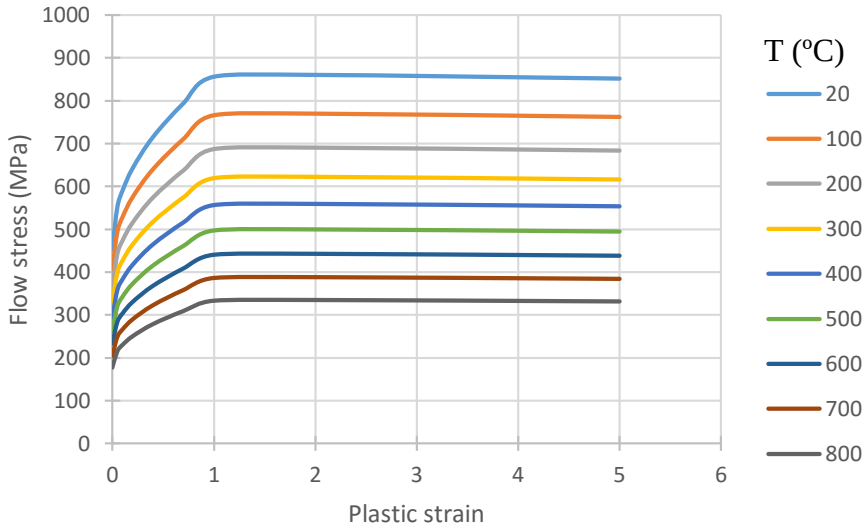

Figure 4.4 – Flow stress vs. strain curves of Al7075-T351 for different temperatures and a fixed strain rate of 1

4.2.3 Titanium alloy Ti6Al4V

This Titanium alloy is an excellent combination of specific strength and corrosion resistance, being the most commonly used alloy. It is significantly stronger than commercially pure titanium while having the similar stiffness and thermal properties.

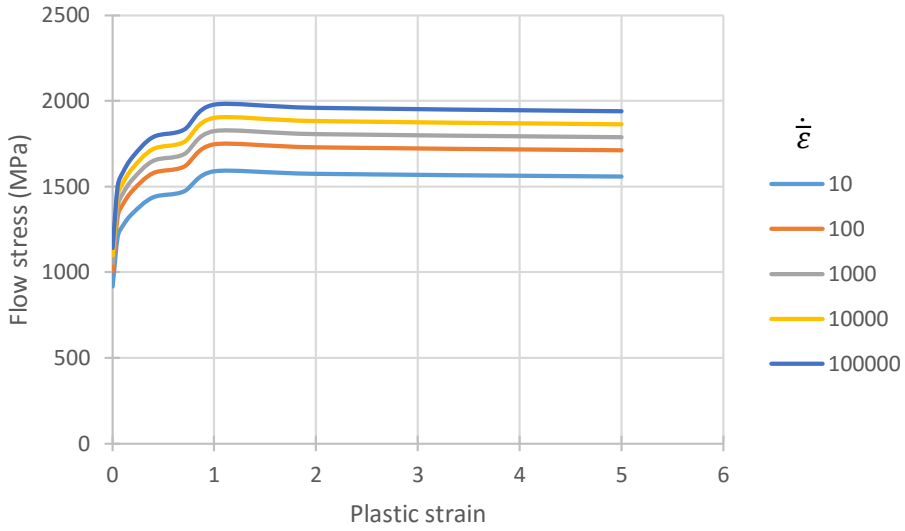

Figure 4.6 – Flow stress vs. strain curves of AISI 316 L for different strain rates and a fixed temperature of 20ºC

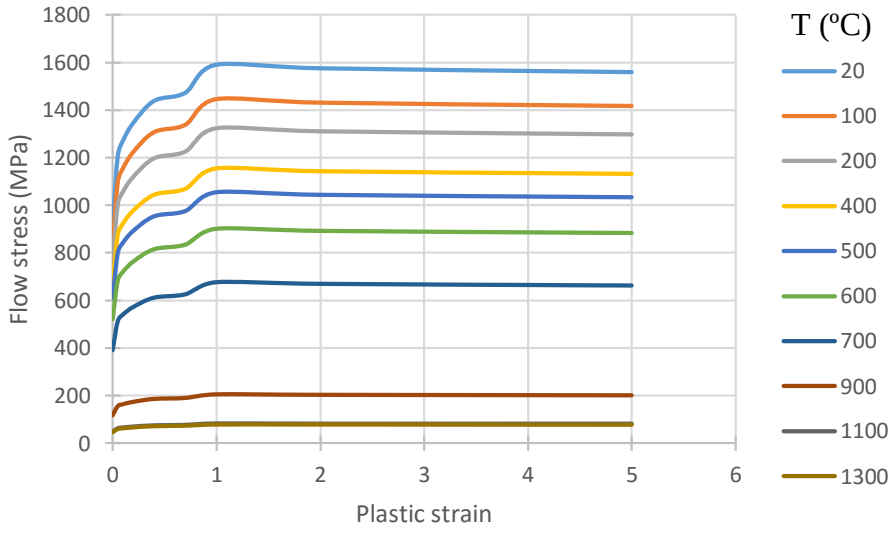

Figure 4.7 – Flow stress vs. strain curves of Al7075-T351 for different temperatures and a fixed strain rate of 10

4.3 Process parameters input

4.3.1 Cutting speed

Cutting speed is one of the metal cutting parameters and it normally defines the nature of the metal cutting operation (finishing or roughing) along with the feed rate. Four different simulations were run for 3 different metals, varying cutting speed only. This way it is possible to analyse cutting speed variation isolated effect. Other simulation parameters were fixed and are summarized in the following table.

Table 4.1 – Summary of simulation parameters used in cutting speed sensitivity analysis

Process	Cutting speed, v_c [m/min]	Al7075-T351 a)250 b)500 c)750 d)1000
		AISI316L a)75 b)150 c)225 d)300
		Ti6Al4V a)25 b)50 c)75 d)100
	Uncut chip thickness, t	0.1 mm
	Cutting length	1.125 mm
	Environment temperature	20ºC
	Environment convection coefficient	0,02 N/s/mm/ºC
Tool Parameters	Material	WC
	Mesh	1092 elements
	Dimensions	Figure 4.8
Workpiece Parameters	Material	Al7075 – T351 AISI316L Ti6Al4V
	Mesh	1548 elements
	Dimensions	4,5x1,0 mm
Contact	Friction (between Tool-Workpiece and Chip-Workpiece)	0.8 (Shear model)
	Heat transfer coefficient (T-W and C-W)	40 N/s/mm/ºC
	Separation Criterion	Default
Numeric	Iteration method	Direct
	Solver	Skyline

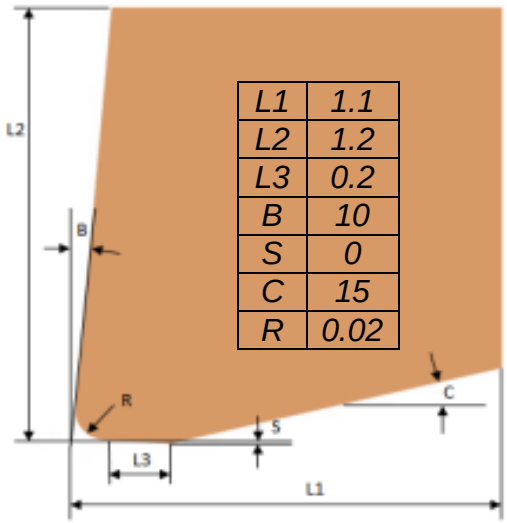

Figure 4.8 – Tool geometry and dimensions used in sensitivity analysis (in millimetres or degrees)

4.3.1.1 Load results

Load-time results are obtained from DEFORM™ in a text file format in which there is two columns: a certain load for each specific time instant of the process. Figure 4.9 shows that data in a curve form for the three different metals.

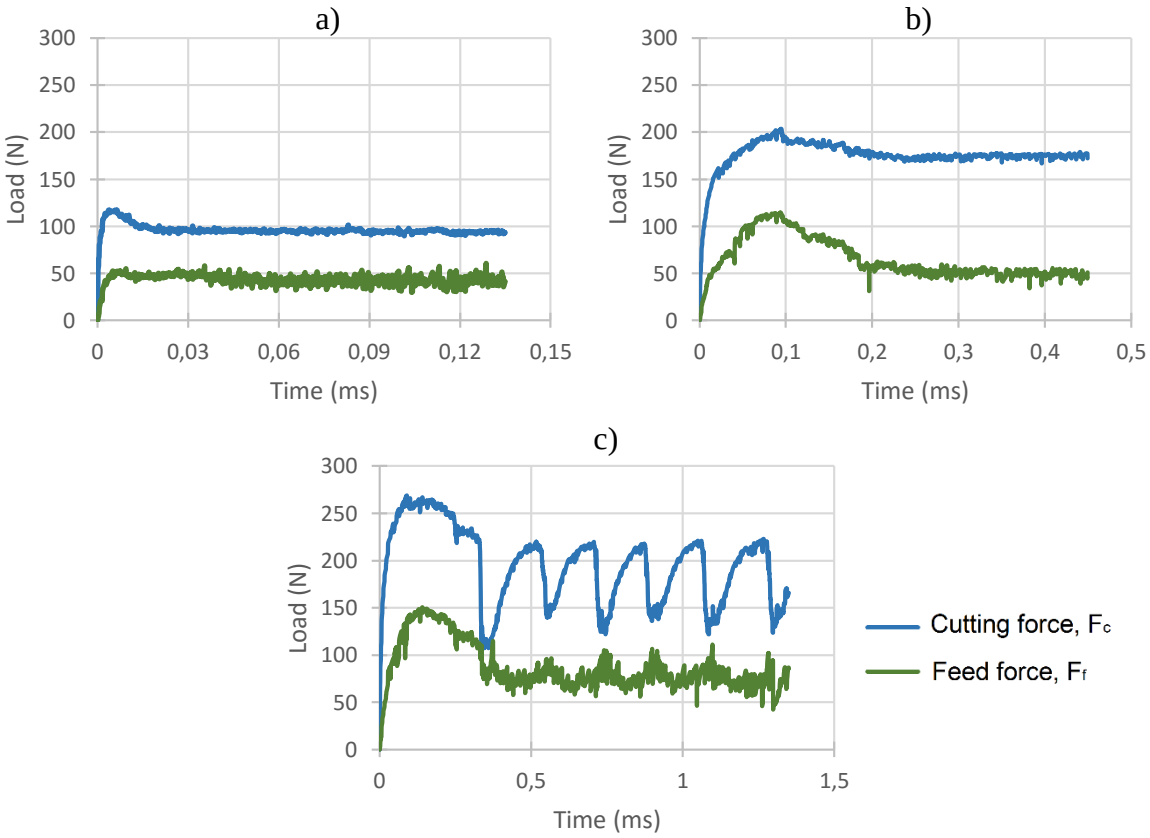

Figure 4.9 – Load-time curves for three different metals:
a) Al7075-T351 (500m/min); b) AISI316L (150m/min); c) Ti6Al4V (50m/min)

At the initial part of each curve, there is a small period where forces reach a maximum. This corresponds to a transient stage of chip formation in the metal cutting process. Already on a steady-state period, loads show small variations that can be caused, among others, by mesh regeneration steps. In order to intuitively compare a considerable amount of information, average load from a steady state section of curves of Figure 4.9 are shown in the following figure.

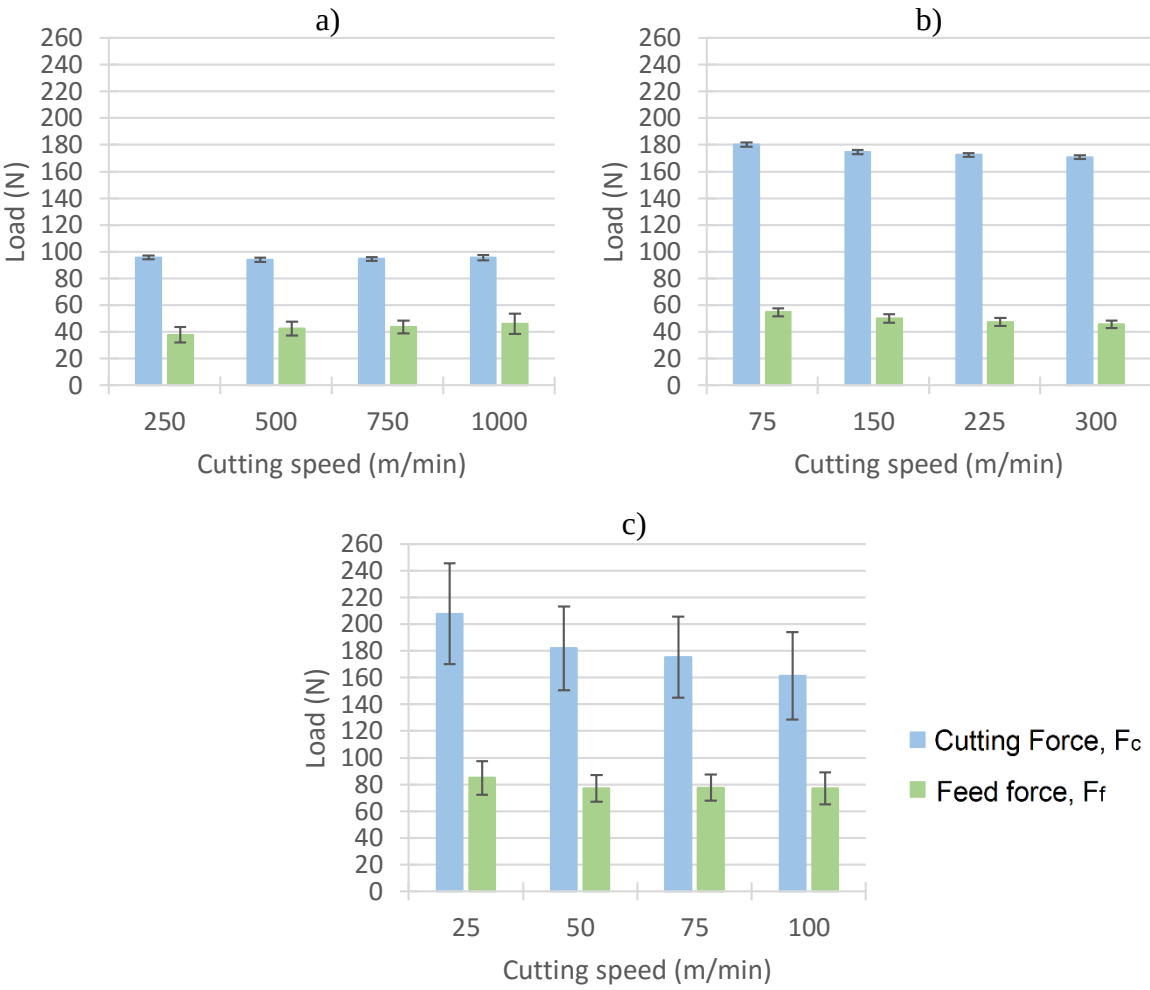

Figure 4.10 – Average load sensitivity on variable cutting speed.

a) Al7075-T351; b) AISI316L; c) Ti6Al4V

Taking into account the load results obtained, cutting speed seems to have a bigger influence on cutting forces when the workpiece material is Titanium alloy. By studying Ti6Al4V and Ti555.3 alloys, Arrazola et al. [68] verified that both cutting and feed forces decrease with cutting speed increase due to the decrease in thickness of the generated chip and thermal softening phenomenon caused by temperature rising.

Moreover, Titanium alloys have a propensity to saw-tooth chip formation which is a source of cutting force components fluctuation [69]. This effect results from thermo-plastic instability in the primary deformation zone [70] and can be noticed in graphs C of Figure 4.9 and Figure 4.10 where average loads show a wide standard deviation.

4.3.1.2 Chip geometry

As shown in Table 4.1, the cutting length of cutting speed sensitivity analysis was the same for all simulations allowing a direct comparison between the created chips. In order to have a notion of the zones and values of maximum stress, von Mises effective stress field distribution is also shown. Figure 4.11 to Figure 4.13 show the chip geometries after the simulation for the 3 materials and different cutting speeds.

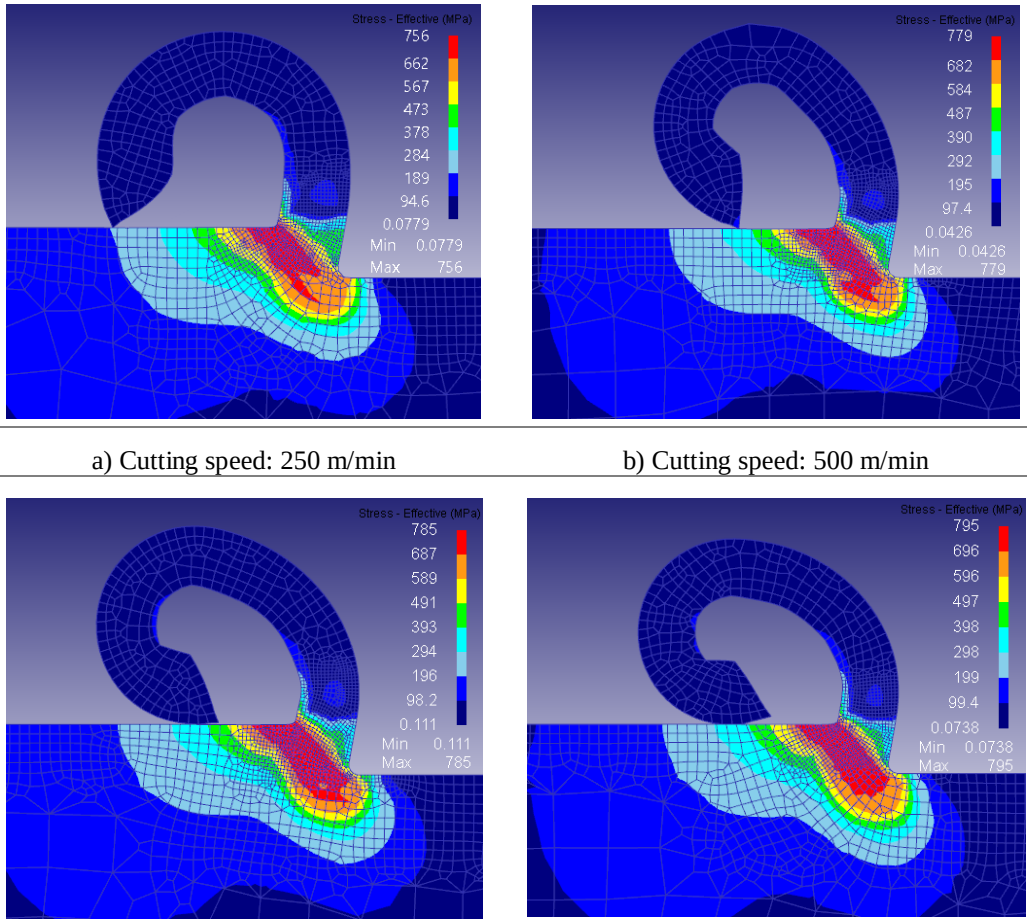

a) Cutting speed: 250 m/min

b) Cutting speed: 500 m/min

c) Cutting speed: 750 m/min

d) Cutting speed: 1000 m/min

Figure 4.11 – Chip geometry with effective stress field distribution for each cutting speed (Al7075-T351)

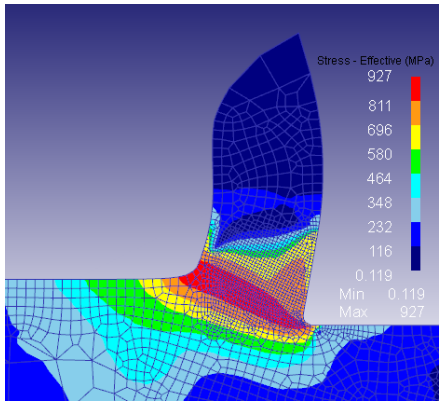

a) Cutting speed: 75 m/min

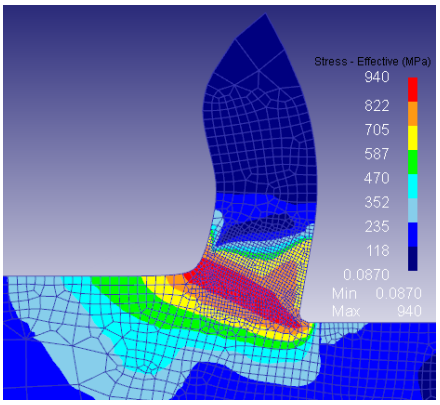

b) Cutting speed: 150 m/min

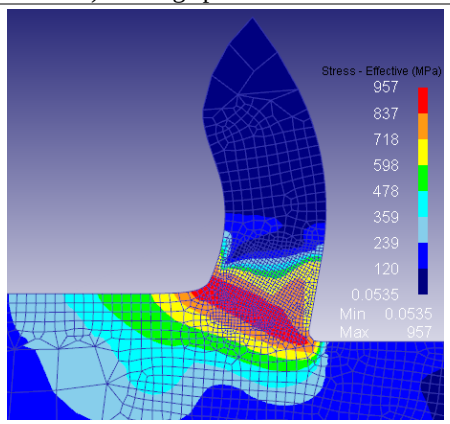

c) Cutting speed: 225m/min

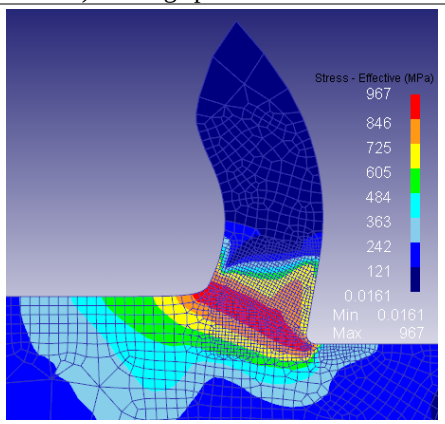

d) Cutting speed: 300 m/min

Figure 4.12 – Chip geometry with effective stress field distribution for each cutting speed (AISI316L)

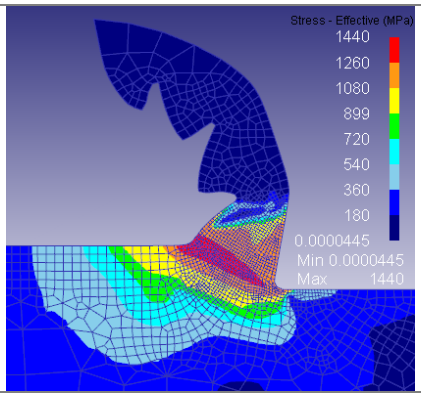

a) Cutting speed: 25 m/min

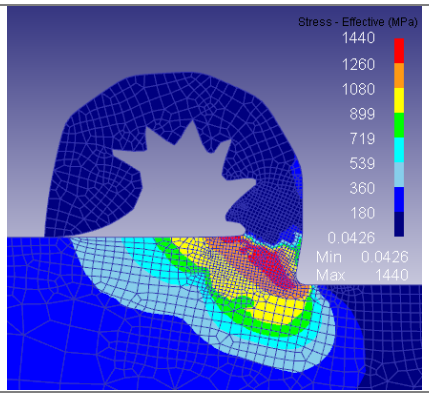

b) Cutting speed: 50 m/min

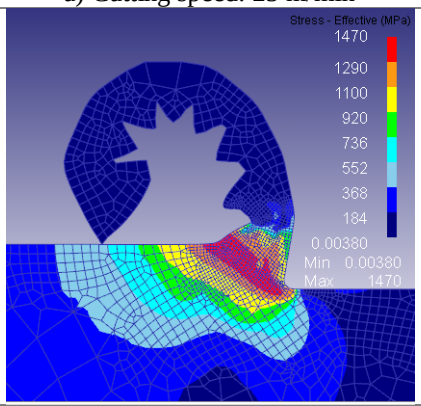

c) Cutting speed: 75 m/min

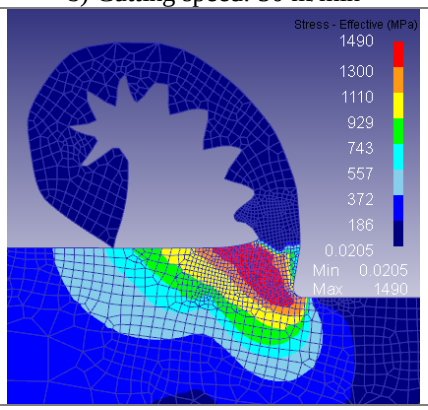

d) Cutting speed: 100 m/min

Figure 4.13 – Chip geometry with effective stress field distribution for each cutting speed (Ti6Al4V)

Curvature radii of Al7075-T351 and AISI316L tends to diminish with cutting speed increase. As suspected, it is also noticeable that values of effective stress increase with cutting speed increase and those were maximum in primary deformation zone. Chip thickness for the AISI 316L stainless steel was less curved than observed for the other materials. Titanium alloy showed the saw-tooth morphology.

4.3.1.3 Maximum temperature results

Figure 4.14 represents the maximum temperatures for each cutting simulation on both tool and workpiece.

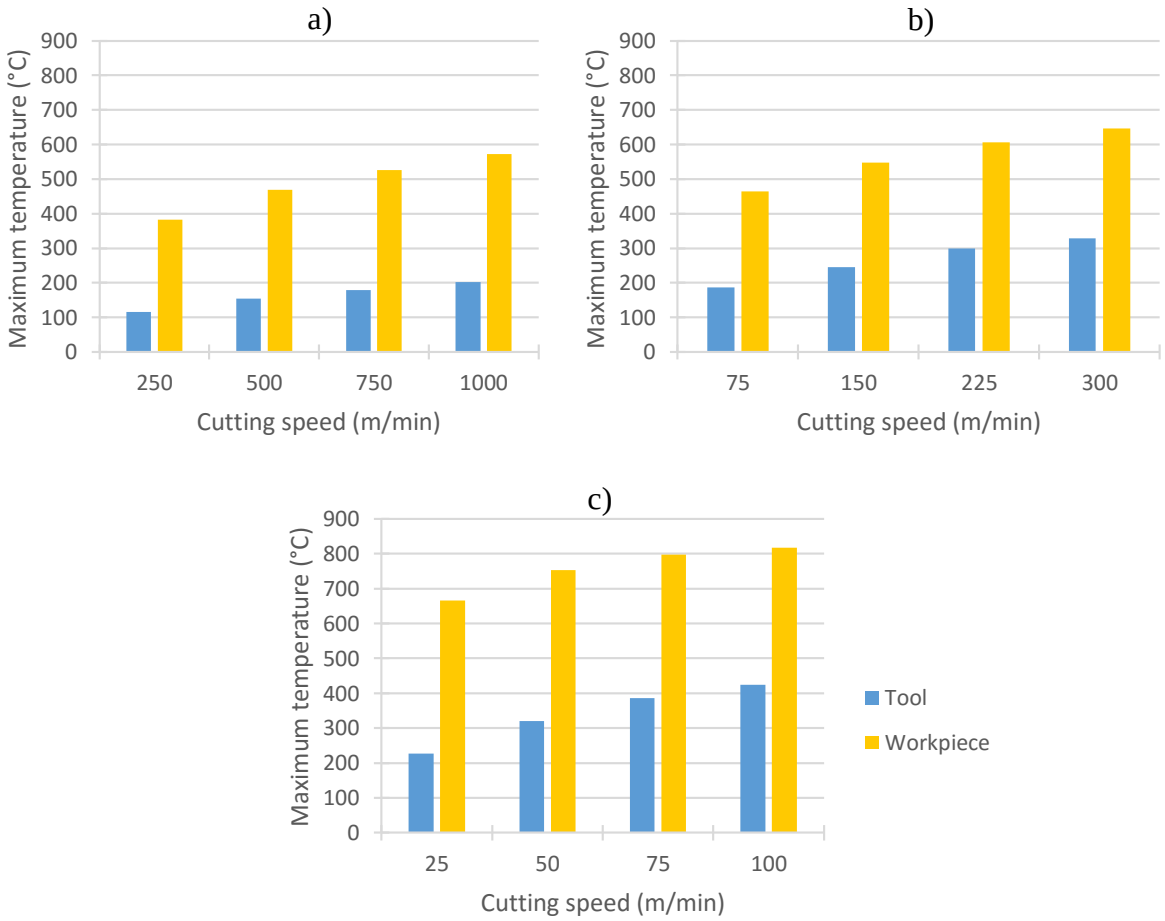

Figure 4.14 – Maximum workpiece and tool temperature sensitivity on variable cutting speed.
a) Al7075-T351; b) AISI316L; c) Ti6Al4V

There is a big difference in maximum reached temperature according to the defined material for the workpiece. It is also seen that with cutting speed increase, maximum reached temperature is higher.

Low cutting speeds are indicated for machining titanium alloys since the generated temperature on tool's cutting edge is directly related to that parameter [71]. In graph c) of Figure 4.14, for a cutting speed of 100 m/min, tool's maximum temperature is about 400ºC which is already twice as much the maximum temperature of the tool when machining aluminium alloy Al7075 (200ºC) at a speed of 1000 m/min (10 times faster).

4.3.1.4 Average Shear Angle Results

Figure 4.15 represents the evolution of the cutting conditions under consideration.

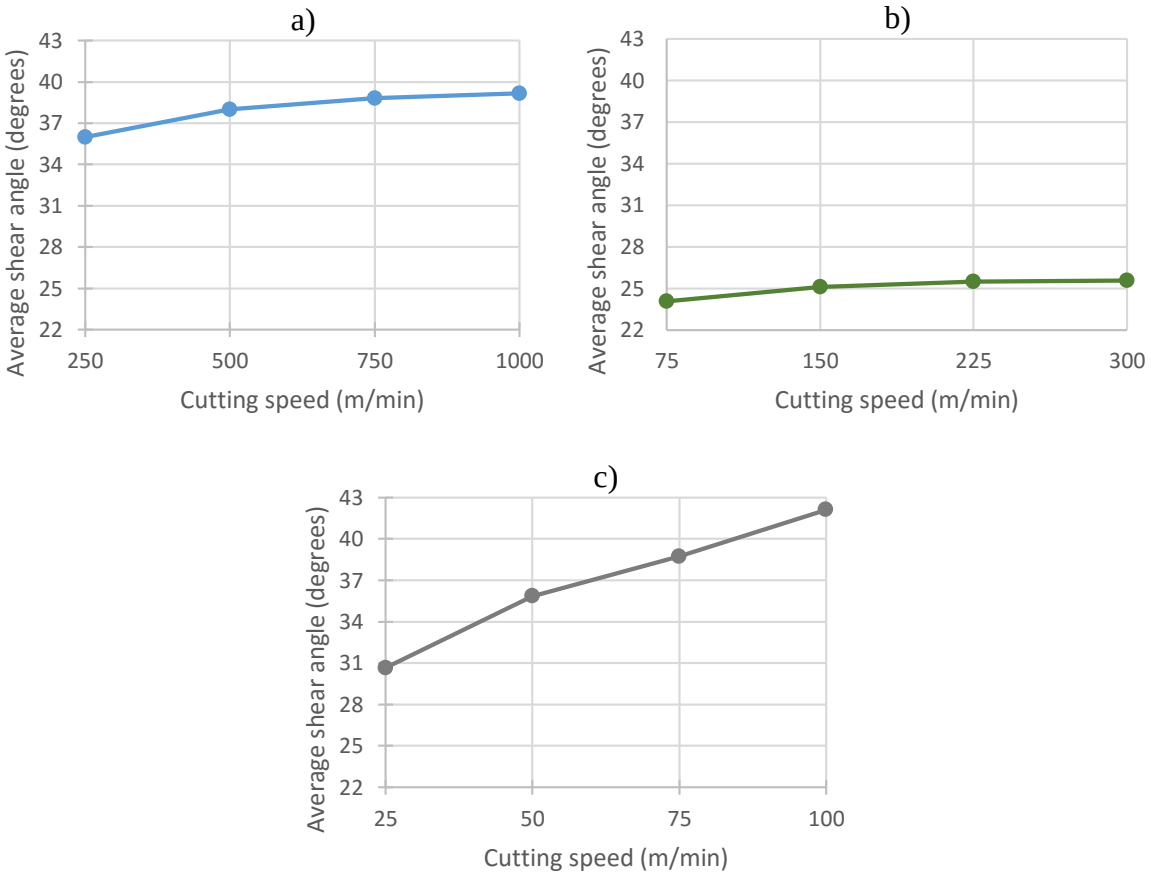

Figure 4.15 – Shear angle variation with cutting speed for three different metals:
a) Al7075 – T351; b) AISI316L; c) Ti6Al4V

The results of shear angle with cutting speed variation meet Oxley's analytical prediction that effective shear angle is smaller at lower speeds than at higher speeds, for given values of tool rake angle and tool-chip interface friction [72]. Cutting speed induces variations in the mean friction angle (β) as well as stress-strain characteristics of the workpiece material that contribute to the increase of the shear angle.

A smaller shear angle (Figure 4.16 – b)) implies a larger shear plane, which requires higher cutting forces when comparing to a bigger angle (Figure 4.16 – a)).

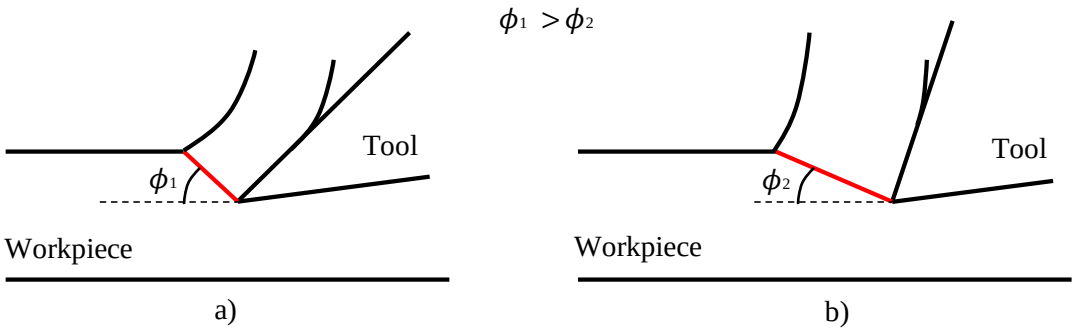

Figure 4.16 – Influence of shear angle on orthogonal cutting

4.3.1.5 Strain-Rate Results

Strain-rate is typically high in metal cutting processes. In order to obtain reasonable results, a big effort in material characterization is needed. High speed impact techniques such as Split-Hopkinson Pressure Bars or Kolsky Bars are currently used in order to do so. High strain rates (greater than 10^2 s^{-1}) can be characterized by their domains: high (10^2 to 10^4 s^{-1}), very high (10^4 to 10^6 s^{-1}) and ultra-high-strain-rate (> 10^6 s^{-1}) [73]. Figure 4.17 illustrates the ranges of strain-rate and corresponding technologies/principles to obtain those strain-rates.

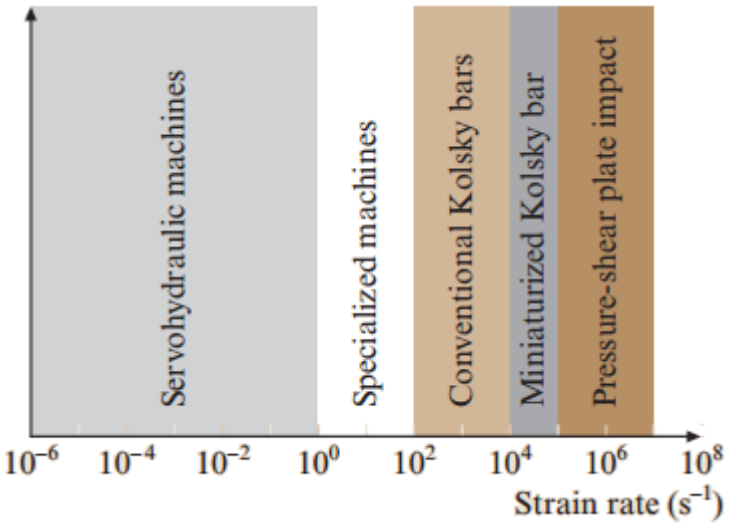

Figure 4.17 - Experimental techniques used for the development of controlled high strain rate deformations in materials [73]

Cutting speed is intimately related with strain-rate, contributing to how fast the material deforms plastically. Figure 4.18 illustrates the maximum strain-rates variation with time for each material as well as a strain rate field distribution, to allow understanding the locations of maximum strain rates, which are on the primary shear zone. It is important to note that the strain-rate magnitude obtained from these simulations is in the range of 10^4 to 10^6 which, according to Figure 4.17, corresponds to very demanding characterization scope.

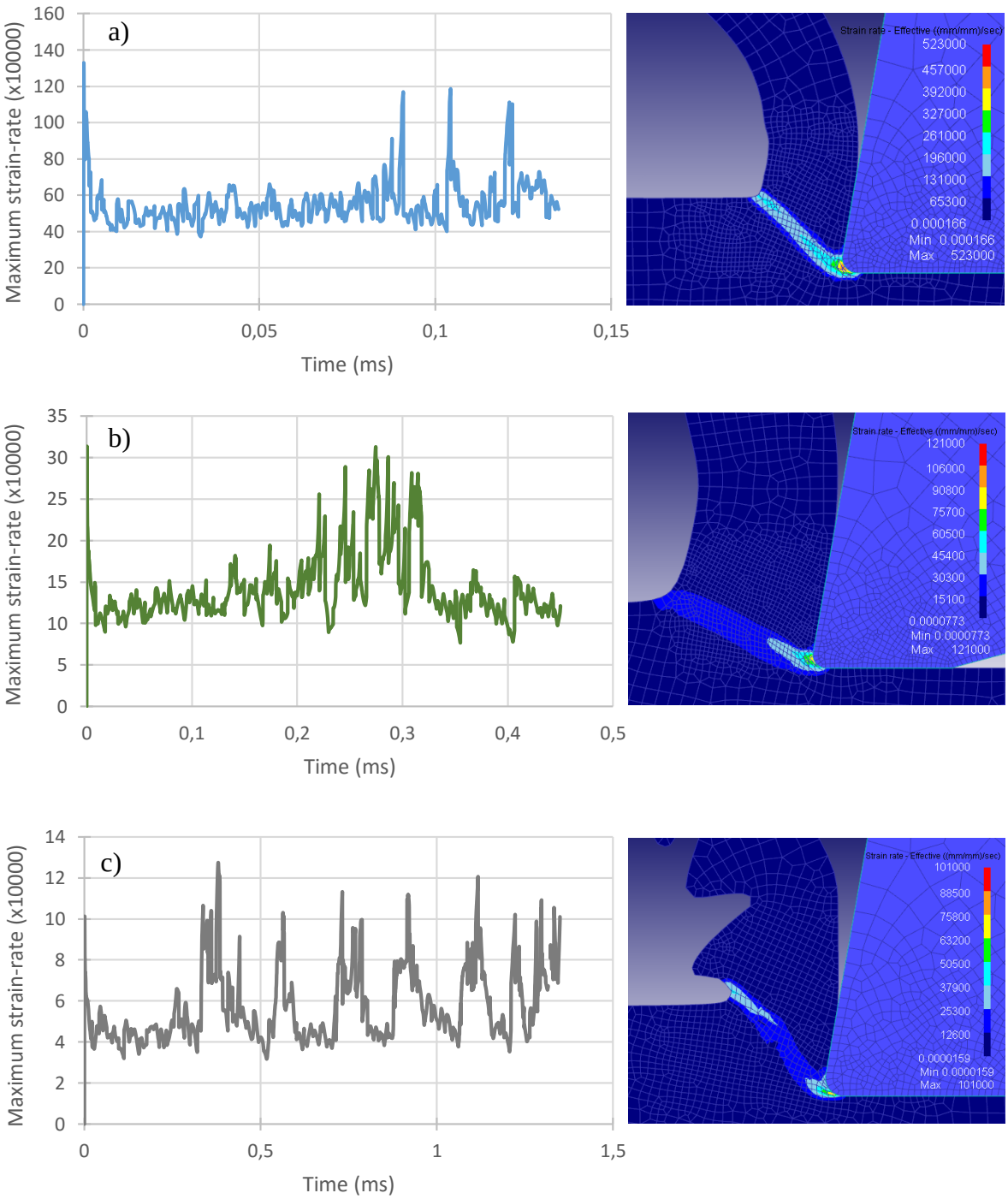

Figure 4.18 – Maximum strain-rate vs. time curves with strain-rate field distribution images for 3 different metals: a) Al7574-T351 (500m/min); b) AISI316L (150 m/min); c) Ti6Al4V (50 m/min)

Mesh regeneration steps have a very big impact on strain-rate vs. time curves. This is related with the very large deformation experienced by the workpiece's mesh. Curve peaks on graphs of Figure 4.18 correspond to remeshing steps making it difficult to understand how maximum strain rate varies with cutting speed. In an attempt of better perceiving the effect of cutting speed on maximum strain-rate, curve peaks were not taken into consideration, resulting in the graphs shown in Figure 4.19.

Three curves were, therefore, defined in Figure 4.19 and it is possible to infer that strain-rate always increases linearly with cutting speed increase for all considered metals. It is also noticed that for higher cutting speeds, the maximum strain rates are also higher.

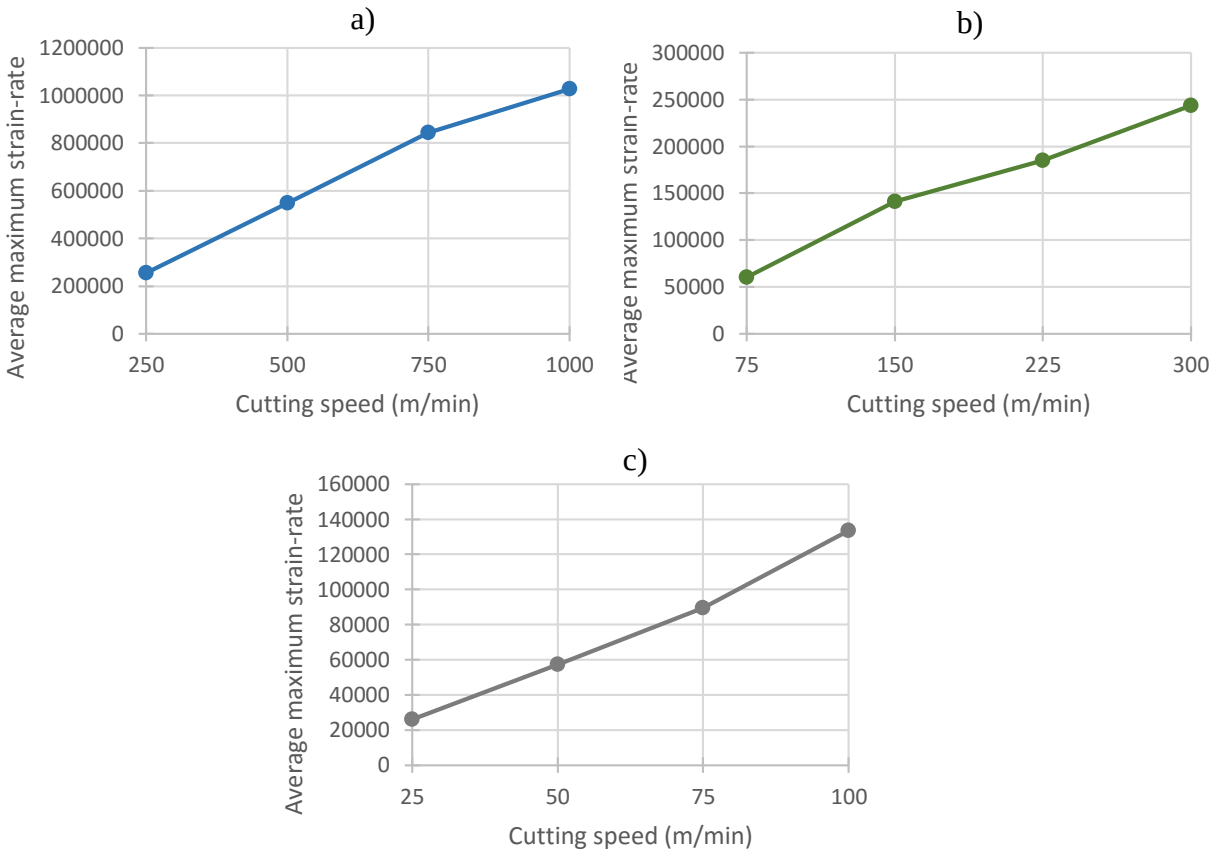

Figure 4.19 – Average strain-rate sensitivity on cutting speed variation for three different metals: a) Al7574-T351 (500m/min); b) AISI316L (150 m/min); c) Ti6Al4V (50 m/min)

4.3.2 Uncut chip thickness

Even though feed rate is closely related to cutting speed, it was this sensitivity analysis goal to study its separate effect. For that, three simulations with different uncut chip thicknesses were run, according to Table 4.2.

Table 4.2 – Summary of simulation parameters used in uncut chip thickness sensitivity analysis

Process	Cutting speed, v_c	100 m/min
	Uncut chip thickness, t	a) 0.1 mm b) 0.5 mm c) 1.0 mm
	Cutting length	1.125 mm
	Environment temperature	20ºC
	Environment convection coefficient	0,02 N/s/mm/ºC
Tool Parameters	Material	WC
	Mesh	a) 1092 elements b) 987 elements c) 1020 elements
	Dimensions	Figure 4.20
Workpiece Parameters	Material	Al7075 – T351 AISI316L Ti6Al4V
	Mesh	a)1548 elements b)1314 elements c)1314 elements
	Dimensions	a) 4.5x1.0 mm b)11.25x2.5 mm c) 22.5x5 mm
Contact	Friction (between Tool-Workpiece and Chip-Workpiece)	0.8 (Shear model)
	Heat transfer coefficient (T-W and C-W)	40 N/s/mm/ºC
	Separation Criterion	Default
Numeric	Iteration method	Direct
	Solver	Skyline

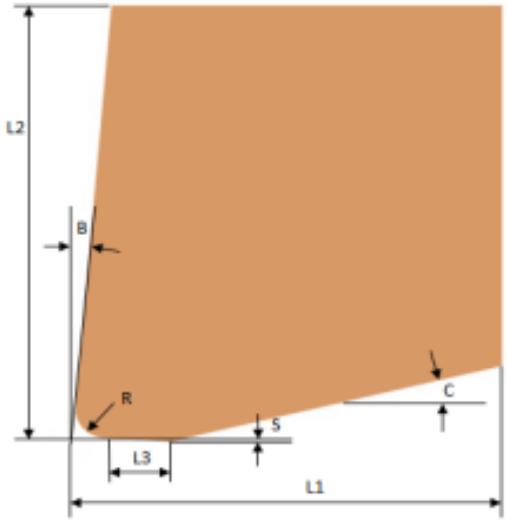

	a)	b)	c)
L1	1.1	2.75	5.5
L2	1.2	3	6
L3	0.2	0.5	1
B	10	10	10
S	0	0	0
C	15	15	15
R	0.02	0.02	0.02

Figure 4.20 – Tool geometry and dimensions used in uncut chip thickness sensitivity analysis (in millimetres or degrees)

DEFORM™ software does not make a distinction between uncut chip thickness and feed rate. Feed rate is a popular parameter in turning operation that indicates the velocity at which the tool advances against the workpiece. In Figure 6.1 of Chapter 6, a correspondence between the two concepts is made. Two-dimensional orthogonal cutting can depict a turning operation. What is called feed rate in 3D turning operation corresponds to the uncut chip thickness of orthogonal cutting.

It was assumed that uncut chip thickness should be at least 5 times smaller than workpiece height, in order to minimize the effect of different ratios between uncut chip thickness and workpiece height, to minimize the influence of distortion of the workpiece during the machining simulation and to achieve a good level of precision with the obtained results.

4.3.2.1 Average Load Results

From the results analysed in this thesis, uncut chip thickness is the parameter with greater influence on cutting and feed forces, as illustrated in Figure 4.21. As expected, cutting forces increase with the increase of uncut chip thickness and an approximate linear relation can be established for each metal.

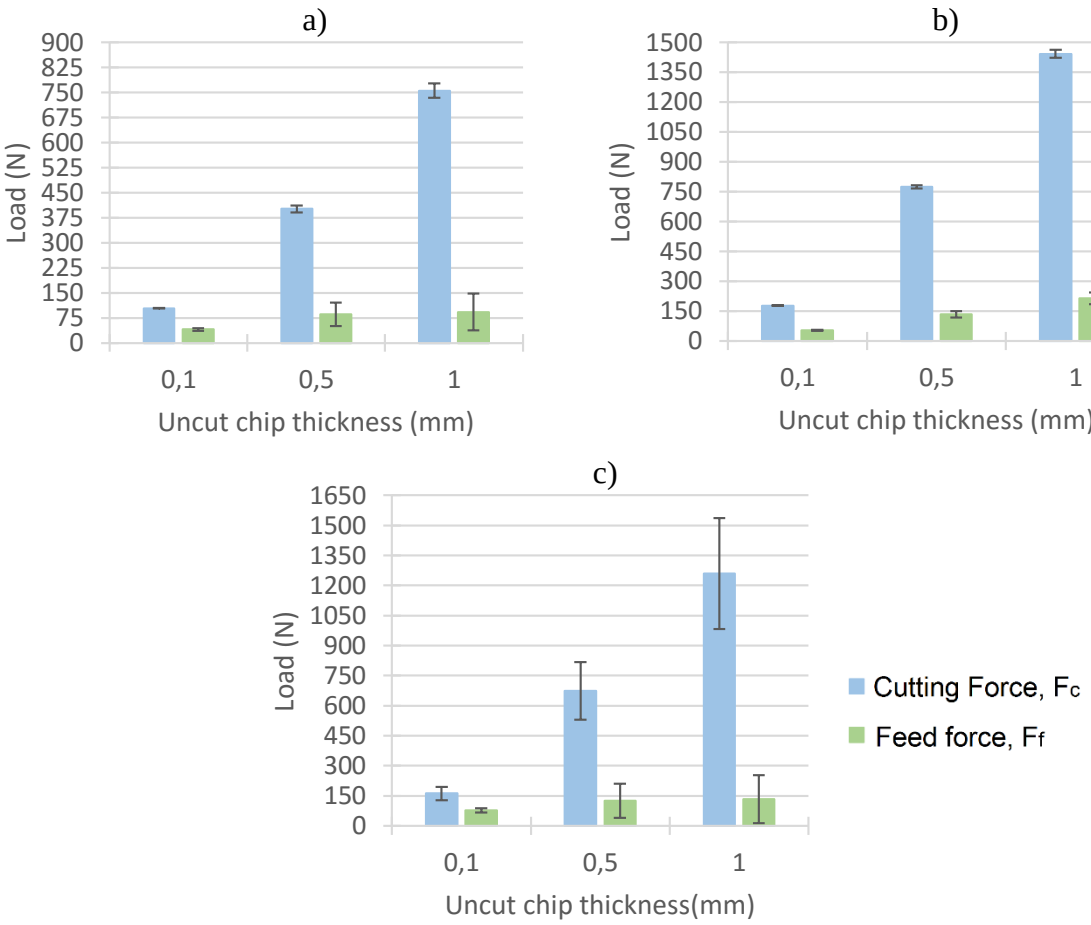

Figure 4.21 – Average load sensitivity on variable uncut chip thickness. a) Al7075-T351; b) AISI316L; c) Ti6Al4V

4.3.2.2 Chip geometry

Figure 4.22 to Figure 4.24 represent the chip geometries for the different simulation with distinct uncut chip thickness. It is important to note that for each material results are not shown in the same scale.

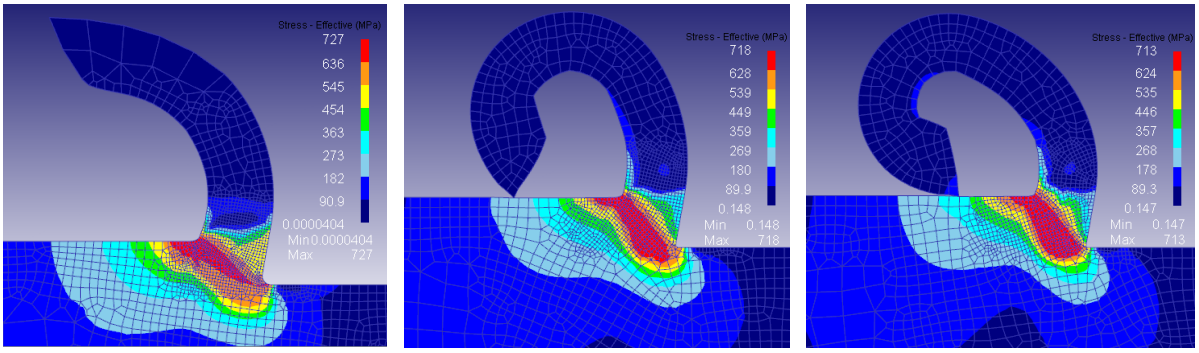

a) $\boldsymbol{t} = 0.1$ mm | b) $t = 0.5$ mm | c) $t = 1$ mm

Figure 4.22 – Chip geometry with stress field distribution for each uncut chip thickness (Al7075-T351)

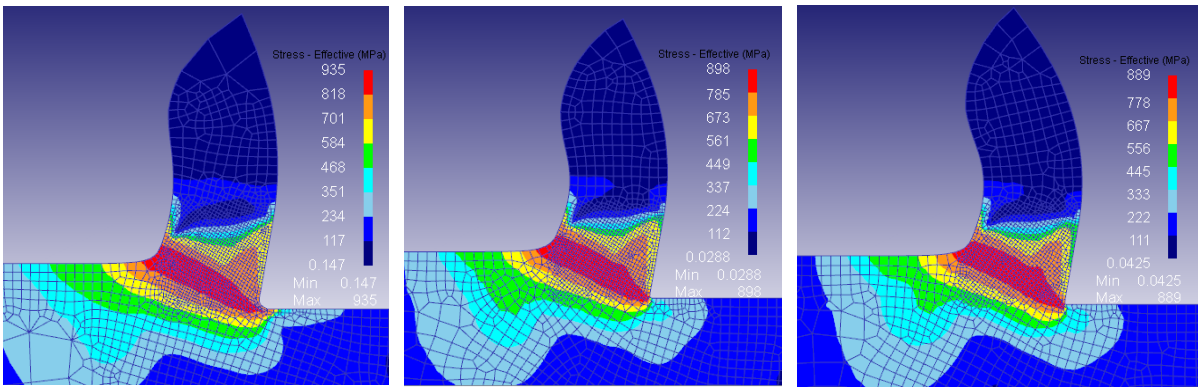

a) $\boldsymbol{t} = 0.1$ mm | b) $t = 0.5$ mm | c) $t = 1$ mm

Figure 4.23 – Chip geometry with stress field distribution for uncut chip thickness (AISI316L)

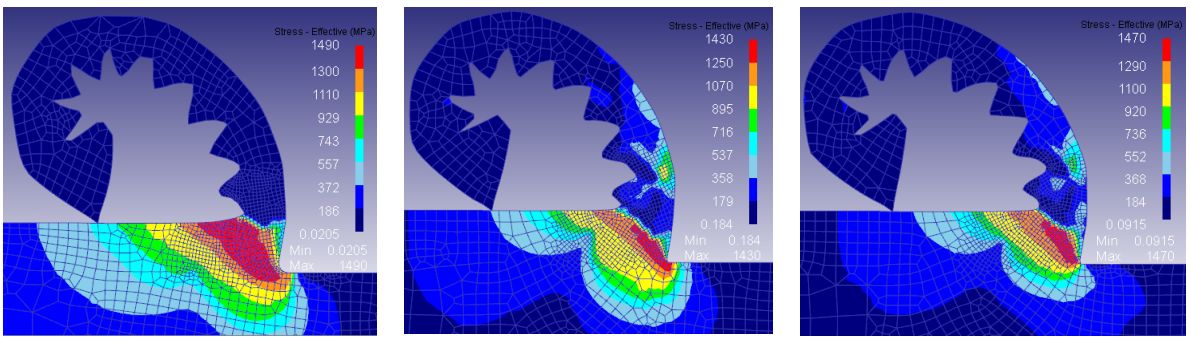

a) $\boldsymbol{t} = 0.1$ mm | b) $t = 0.5$ mm | c) $t = 1$ mm

Figure 4.24 – Chip geometry with stress field distribution for each uncut chip thickness (Ti6Al4V)

For Al7075-T351 and AISI316L, chip curvature tends to increase for bigger uncut chip thickness, being more evident in Aluminium chip formation, which would represent higher tendency for chip breakage. For the two mentioned metals it is also noticeable that maximum effective stress decreases with uncut chip thickness increase. It is important to underline that even though chip geometry of Titanium alloy seems to be the same for the 3 cases, overall dimensions differ, as pointed out in Figure 4.24.

4.3.2.3 Maximum temperature results

Figure 4.25 represents the maximum temperatures simulated in each cutting simulation for both tool and workpiece.

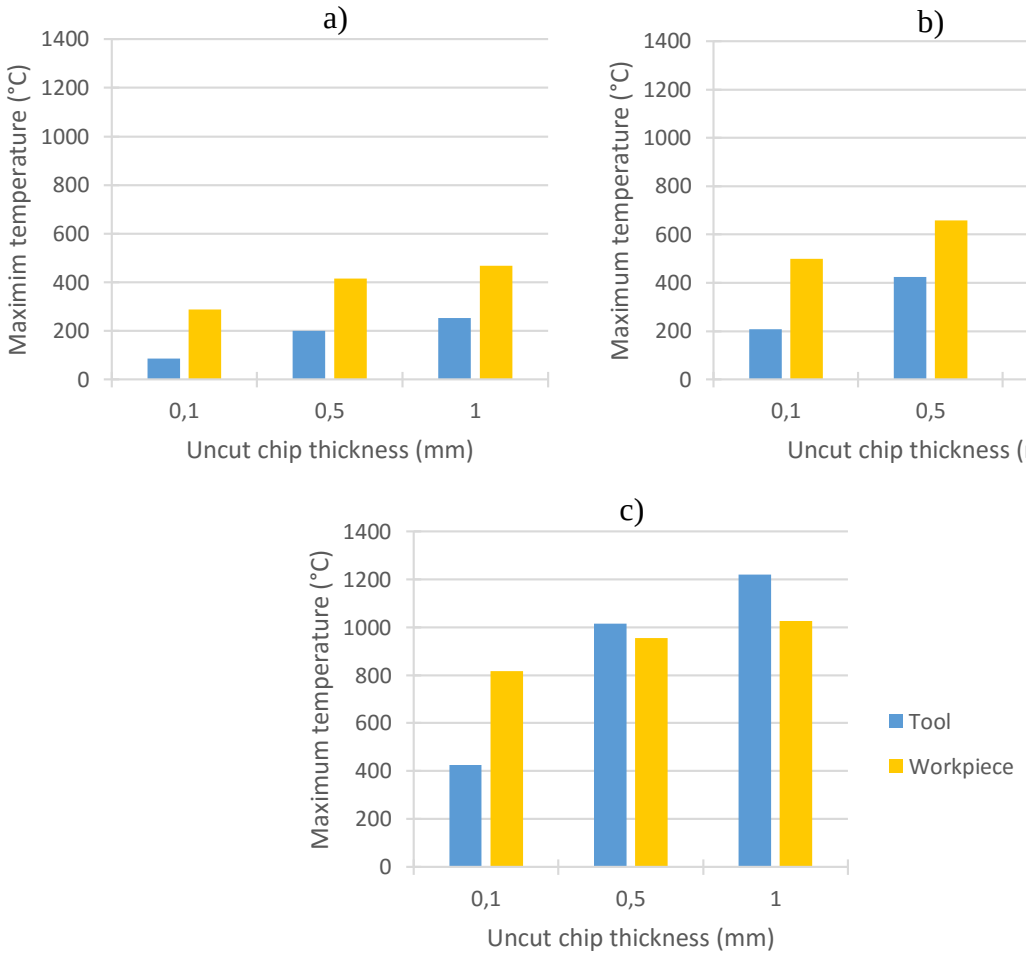

Figure 4.25 – Maximum workpiece and tool temperature sensitivity on variable uncut chip thickness. A) Al7075-T351; B) AISI316L; C) Ti6Al4V

Maximum temperatures for the mentioned cutting length are higher with uncut chip thickness increase. Workpiece material plays a significant role in determining its evolution and range of values. It is important to emphasize that at an incipient stage of the metal cutting operation, heat is transferred into workpiece to tool direction. However, at certain point this heat transfer direction is inverted. In Figure 4.25 it is noticeable that that point was reached for the Titanium simulation when uncut chip thickness was 0.5 and 1 mm. This can be related to the additional friction that saw tooth chip geometry generated on the tool.

4.3.2.4 Average Shear Angle Results

Figure 4.26 represents the evolution of the shear angle according the considered parameters, for each material.

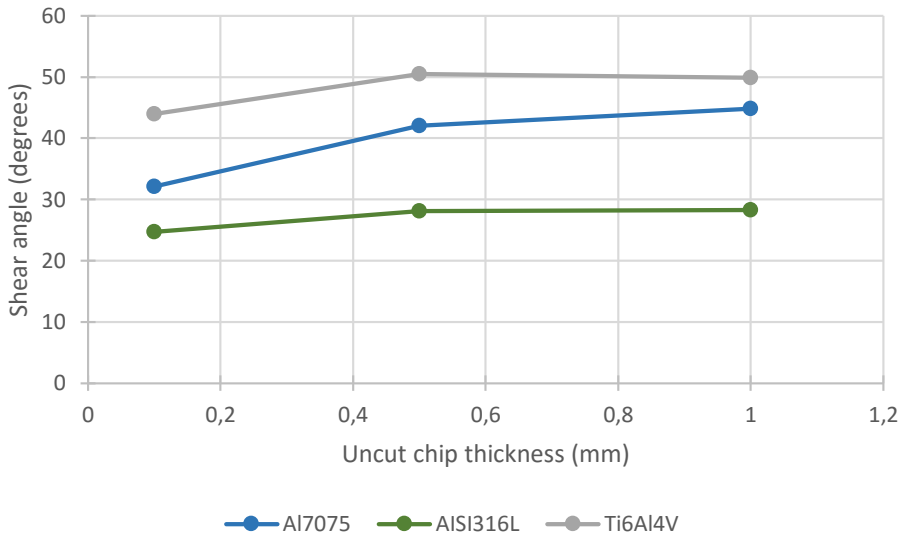

Figure 4.26 – Shear angle sensitivity on variable uncut chip thickness for three different metals

Unlike in cutting speed sensitivity analysis, a smaller shear angle does not mean higher cutting forces, for the simple reason that when increasing t, the section of chip to be cut increases, generating a bigger resistance thus, an increase in cutting forces. The variation of the average shear angle tends to stabilize for uncut chip thicknesses above 0.5 mm.

4.3.3 Tool rake angle

In this section the influence of the rake angle is investigated. Table 4.3 summarizes the simulation parameters used in this specific study. Figure 4.27 illustrates the tool geometry and the considered rake angle values in this study. Both negative and positive angle values were considered in this study.

Table 4.3 – Summary of simulation parameters used in tool rake angle sensitivity analysis

Process	Cutting speed, v_c	100 m/min
	Uncut chip thickness, t	0.1 mm/rev
	Cutting length	1.125 mm
	Environment temperature	20ºC
	Environment convection coefficient	0.02 N/s/mm/ºC
Tool Parameters	Material	WC
	Mesh	1092 elements
	Dimensions	Figure 4.27
Workpiece Parameters	Material	Al7075 – T351 AISI316L Ti6Al4V
	Mesh	1548 elements
	Dimensions	4.5x1.0 mm
Contact	Friction (between Tool-Workpiece and Chip-Workpiece)	0.8 (Shear model)
	Heat transfer coefficient (T-W and C-W)	40 N/s/mm/ºC
	Separation Criterion	Default
Numeric	Iteration method	Direct
	Solver	Skyline

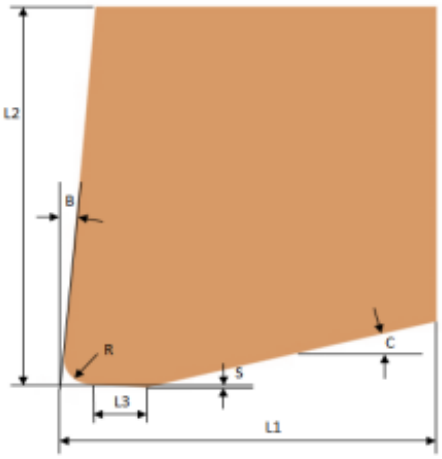

	a)	b)	c)	d)
L1	1.1	1.1	1.1	1.1
L2	1.2	1.2	1.2	1.2
L3	0.2	0.2	0.2	0.2
B	**-10**	**0**	**10**	**20**
S	0	0	0	0
C	15	15	15	15
R	0	0.02	0.02	0.02

Figure 4.27 – Tool geometry and dimensions used in tool rake angle sensitivity analysis (in millimetres or degrees)

4.3.3.1 Average Load Results

Figure 4.28 presents the average values of cutting forces for distinct rake angle values and materials.

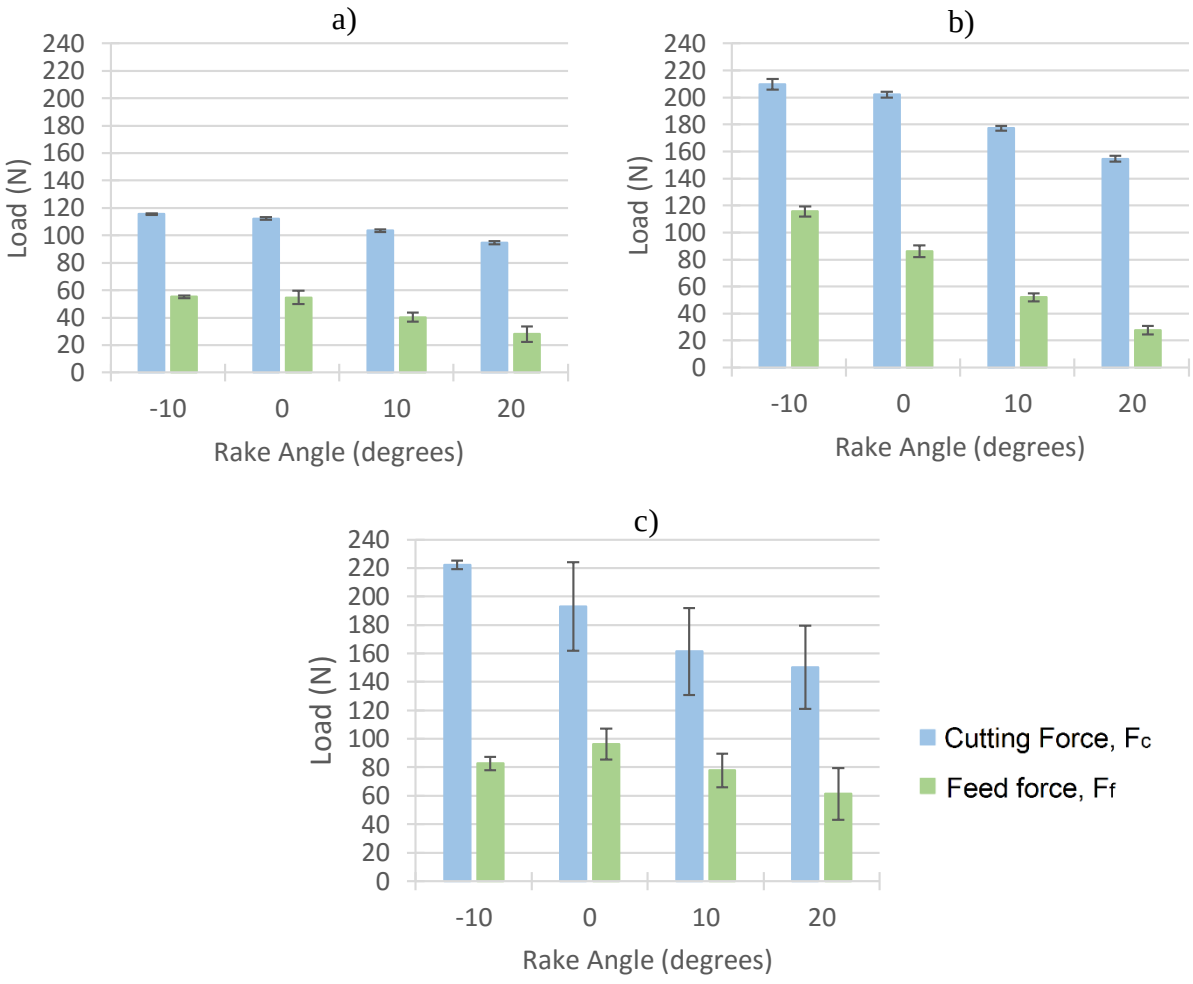

Figure 4.28 – Average load sensitivity on variable tool rake angle. a) Al7075-T351; b) AISI316L; c) Ti6Al4V

Positive rake angles induce smaller cutting forces when compared to negative cutting angles and that phenomenon has been verified in the conducted sensitivity analysis. It is also true that the bigger the rake angle is, the less resistant is the tool, as the small cutting edge may break. Numerical simulation allows cutting forces prediction and experimentation without tool damage possibility, which is convenient when trying to find a balance between cutting forces and tool rake angle.

The aluminium alloy showed the absolute lowest cutting forces and the influence of the rake angle is lower for this material than observed for AISI 315L and Ti6Al4V alloys. The scatter in the cutting force for the Titanium alloy is higher due to the effect of saw-tooth chip formation.

4.3.3.2 Chip Geometry

Chip geometry will certainly be influenced by tool rake face angle. With increasing rake angles, curvature radii of the obtained chips tends to be smaller. Also the chip thickness is influenced by the rake angle as verified by Figure 4.29 to Figure 4.30. This relation is well noticeable on aluminium alloy Al7075 and stainless steel AISI316L. For the titanium alloy with increasing rake angles, generated chip tends to grow more vertically before rolling and the periodicity of the serrated chip increases.

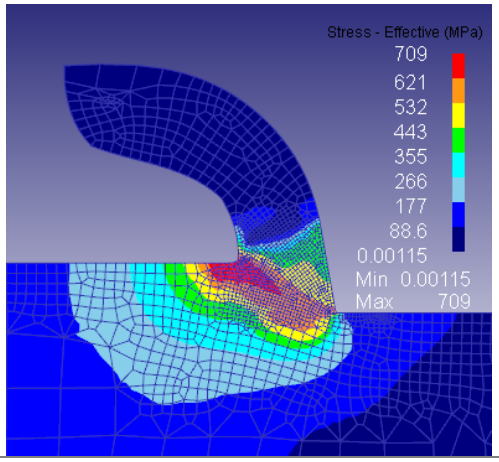

a) Rake angle: -10º

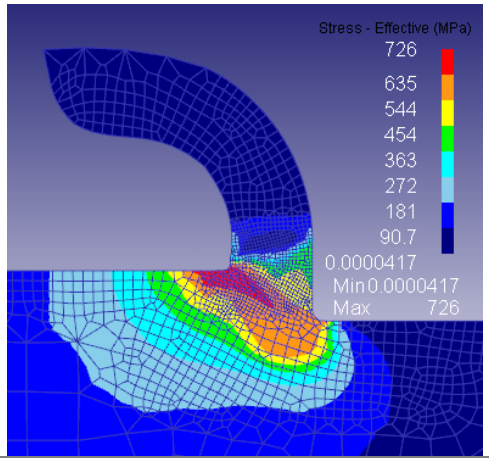

b) Rake angle: 0º

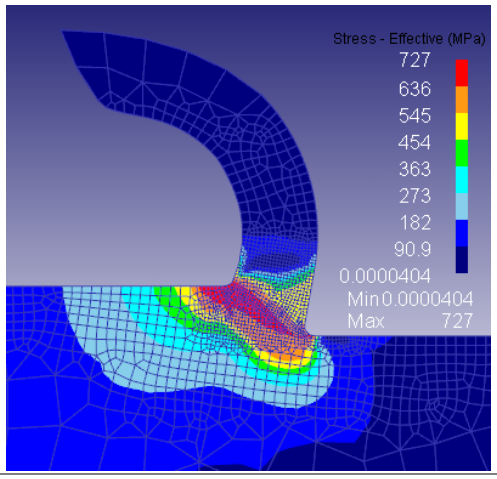

c) Rake angle: 10º

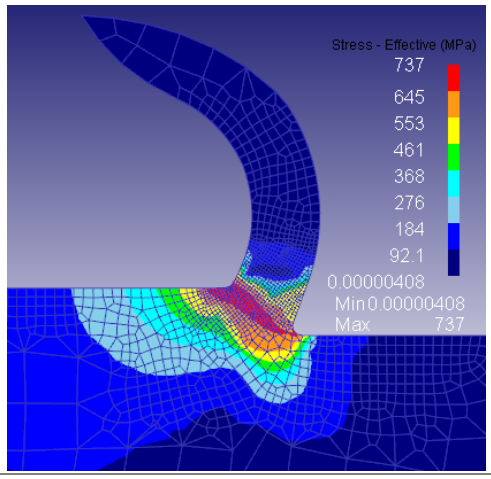

d) Rake angle: 20º

Figure 4.29 – Chip geometry with stress field distribution for each rake angle (Al7075-T351)

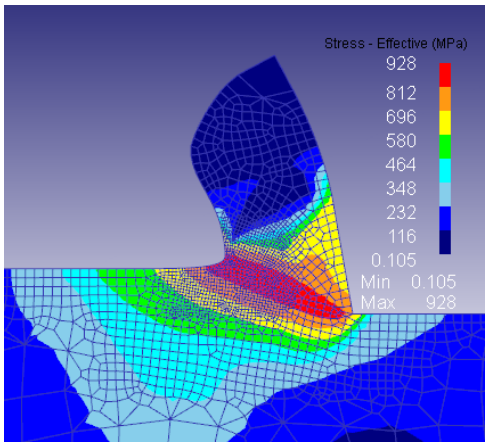

a) Rake angle: -10º

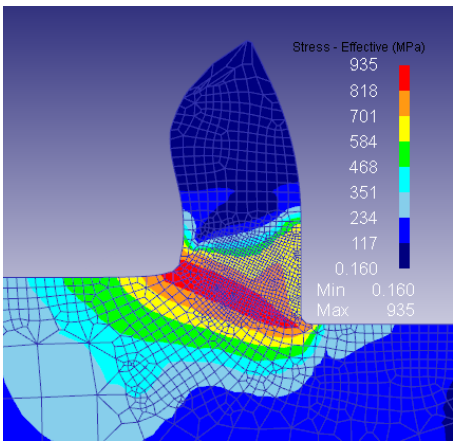

b) Rake angle: 0º

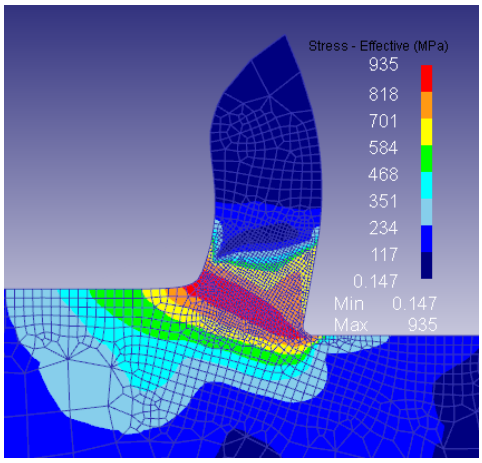

c) Rake angle: 10º

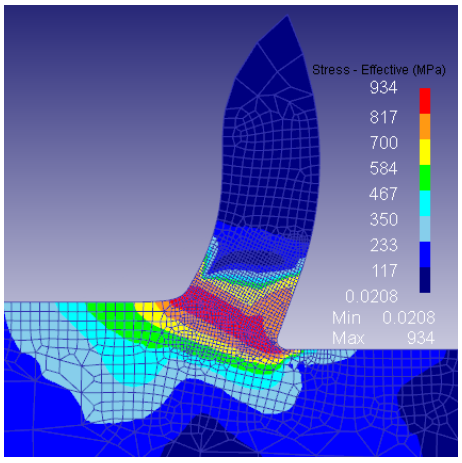

d) Rake angle: 20º

Figure 4.30 - Chip geometry with stress field distribution for each rake angle (AISI316L)

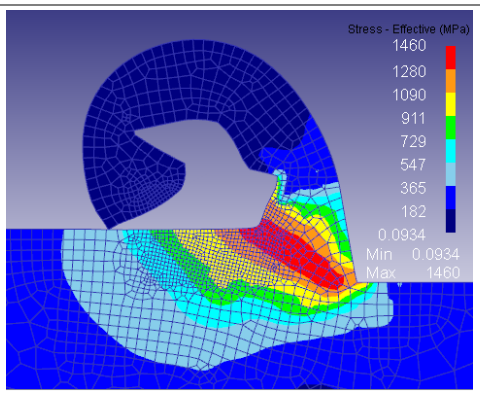

a) Rake angle: -10º

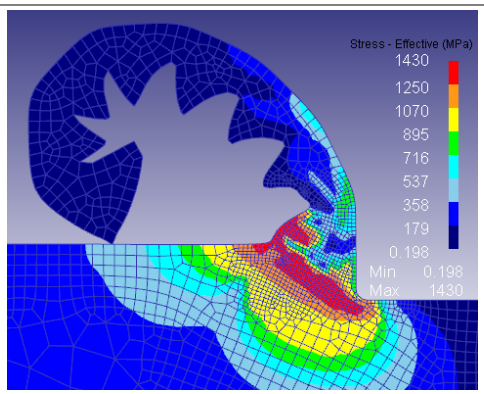

b) Rake angle: 0º

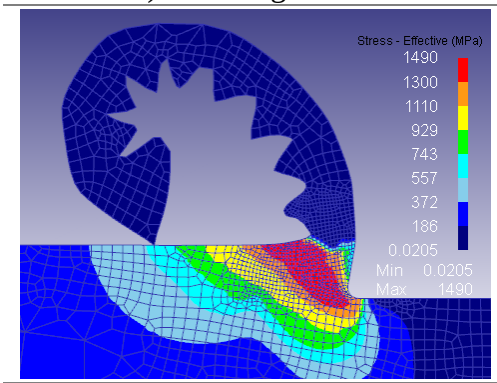

c) Rake angle: 10º

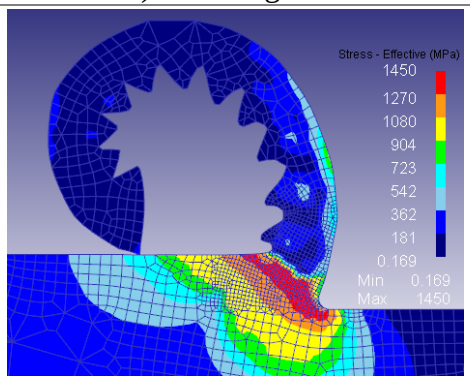

d) Rake angle: 20º

Figure 4.31 – Chip geometry with stress field distribution for each rake angle (Ti6Al4V)

4.3.3.3 Maximum Temperature Results

Figure 4.32 illustrates the maximum temperatures attained in the tool and workpiece for the different rake angles and materials.

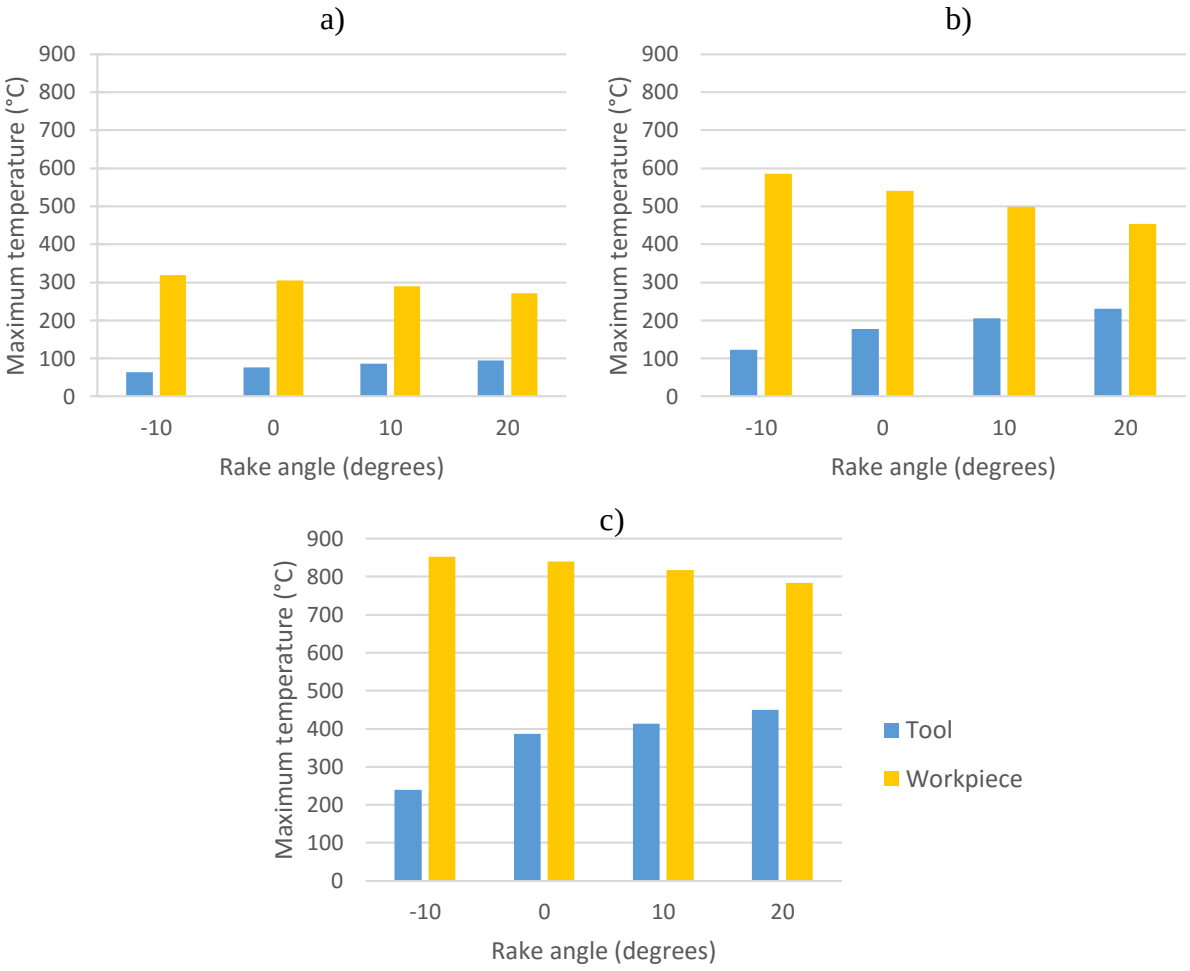

Figure 4.32 – Maximum workpiece and tool temperature sensitivity on variable tool rake angle. a) Al7075-T351; b) AISI316L; c) Ti6Al4V

Negative rake angles make the tool blunter, which increases friction and results in higher maximum reached temperatures in the orthogonal cutting operation. As supported by Figure 4.32, positive rake angles make the tool sharper, which results in less cut resistance and smaller maximum temperatures. However, it is interesting to note that tool increases its temperature with rake angle increasing.

4.3.3.4 Average Shear Angle Results

Figure 4.33 illustrates the shear angle evolution with the rake angle for three different materials.

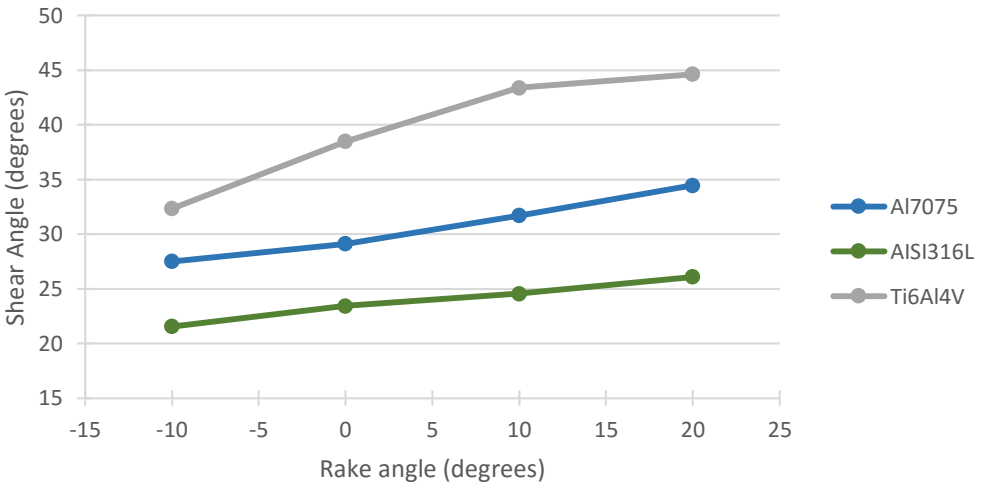

Figure 4.33 – Shear angle sensitivity on variable tool rake angle for three different metals

According to Merchant's theory mentioned in Chapter 2, an increase in rake angle means an increase of shear angle for the same friction angle. The conducted simulations validate that relationship. The simulated trend is approximately linear for the aluminium and AISI 316L stainless steel. For the Titanium alloy this trend seems to stabilize after a rake angle of 20º. The Titanium alloy showed the highest shear angle and AISI 316L alloy the lowest.

4.3.4 Tool cutting edge radius

Tool geometry is bound to have great influence on orthogonal cutting simulation. As a border between tool and workpiece, cutting edge radius is a parameter that should be taken into account in this sensitivity analysis. Table 4.4 summarizes the simulation parameters used in this study and Figure 4.34 summarizes the geometry features of the tool geometry. Cutting edge radius within 0,02 and 0,07 mm were considered in this simulations.

Table 4.4 – Summary of simulation parameters used in tool cutting edge sensitivity analysis

Process	Cutting speed, v_c	100 m/min
	Uncut chip thickness, t	0.1 mm/rev
	Cutting length	1.125 mm
	Environment temperature	20ºC
	Environment convection coefficient	0.02 N/s/mm/ºC
Tool Parameters	Material	WC
	Mesh	1092 elements
	Dimensions	Figure 4.34
Workpiece Parameters	Material	Al7075 – T351 AISI316L Ti6Al4V
	Mesh	1548 elements
	Dimensions	4.5x1.0 mm
Contact	Friction (between Tool-Workpiece and Chip-Workpiece)	0.8 (Shear model)
	Heat transfer coefficient (T-W and C-W)	40 N/s/mm/ºC
	Separation Criterion	Default
Numeric	Iteration method	Direct
	Solver	Skyline

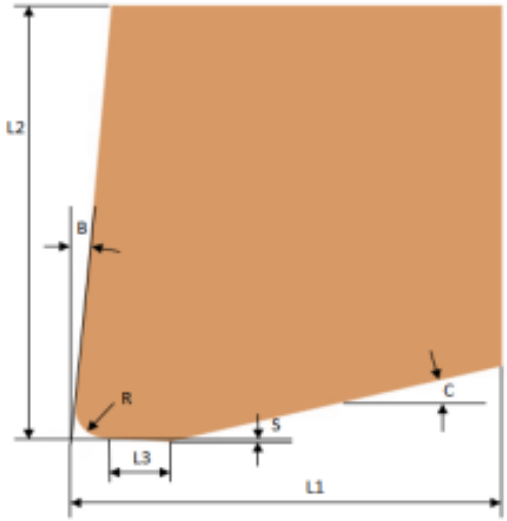

	a)	b)	c)
L1	1.1	1.1	1.1
L2	1.2	1.2	1.2
L3	0.2	0.2	0.2
B	10	10	10
S	0	0	0
C	15	15	15
R	0.02	0.03	0.07

Figure 4.34 - Tool geometry and dimensions used in tool cutting edge radius sensitivity analysis (in millimetres or degrees)

Outeiro [74] introduces the criterion of relative tool sharpness (RTS), which is the ratio between uncut chip thickness (t) and the radius of the cutting edge (r_n).

$$RTS = \frac{t}{r_n} \quad (53)$$

RTS should be kept higher than critical RTS, which corresponds to negligibly small influence of the cutting edge radius on the cutting process. Critical RTS was defined as 3, as an initial assumption. This way, three different radii were tested: two of those (0.02 and 0.03 mm) have a RTS greater than 3 while another (0.07) with a RTS smaller than the assumed critical value.

4.3.4.1 Average Load Results

Figure 4.35 presents the average loads versus the tool tip radius for distinct materials. In general, the average loads increase with the increase of cutting edge radius. However, a higher increase is more evident for cutting edge radius of 0,07 mm.

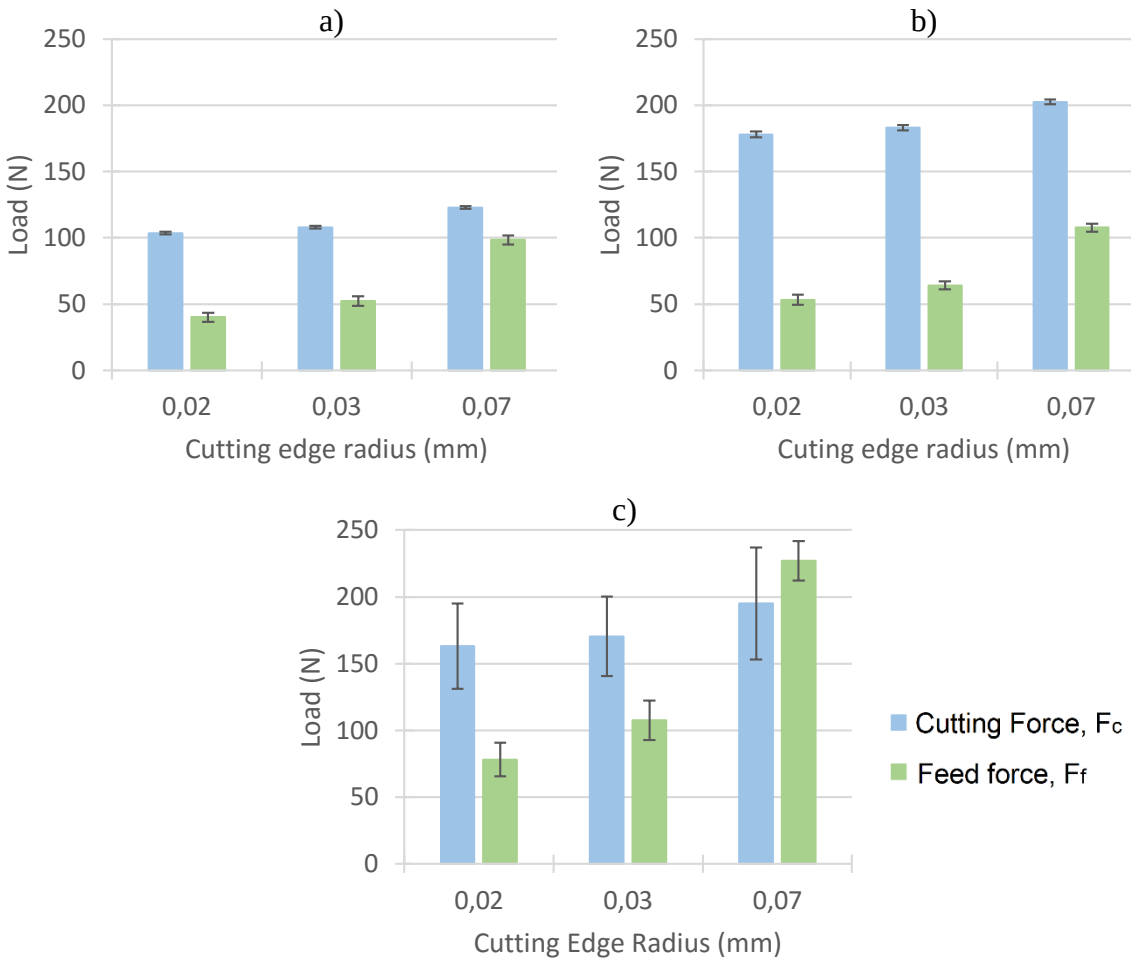

Figure 4.35 – Average load sensitivity on variable tool cutting edge. a) Al7075-T351; b) AISI316L; c) Ti6Al4V

When comparing loads of the two cutting edge radii that verify assumed critical RTS criterion, a small variation can be noticed. It is suggested by Outeiro that total uncut chip thickness can be divided in two parts: actual uncut chip thickness, t_1 and a burnished layer, h_p [74], see figure Figure 4.36 .

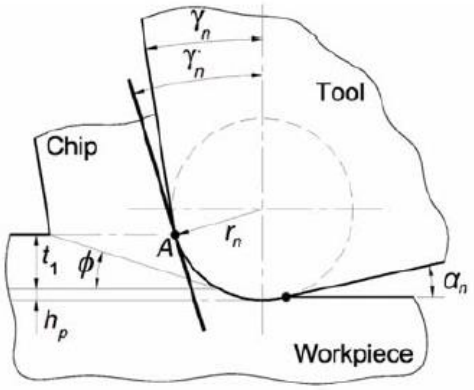

Figure 4.36 – Detail of round tool cutting edge in orthogonal cutting chip formation [74]

For a cutting edge radius of 0.07 mm it is noticeable a feed force significant increase. This is related with the fact that for bigger cutting edge radius burnishing layer increases meaning higher feed forces.

4.3.4.2 Chip Geometry

Figure 4.37 to Figure 4.39 illustrate the chip geometry and equivalent stress fiends for the different cutting edge radius and materials.

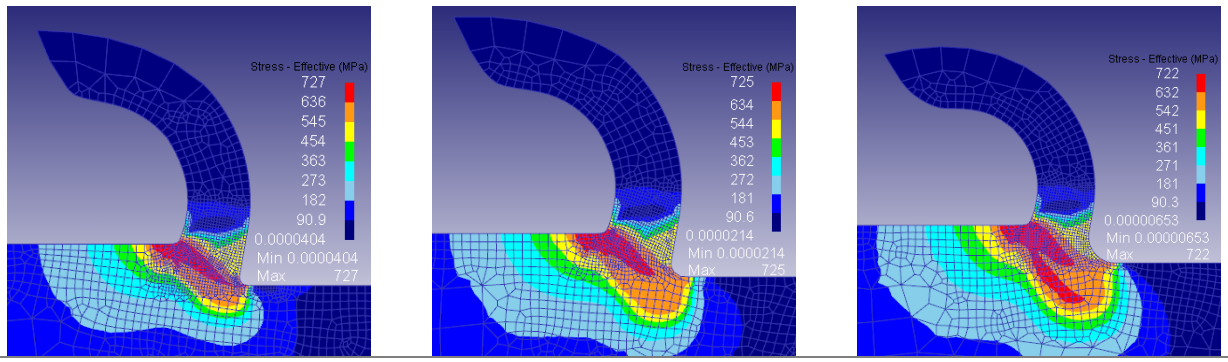

a) Cutting edge radius: 0.02 mm b) Cutting edge radius: 0.03 mm c) Cutting edge radius: 0.07 mm

Figure 4.37 – Chip geometry with stress field distribution for tool cutting radius analysis (Al7075-T351)

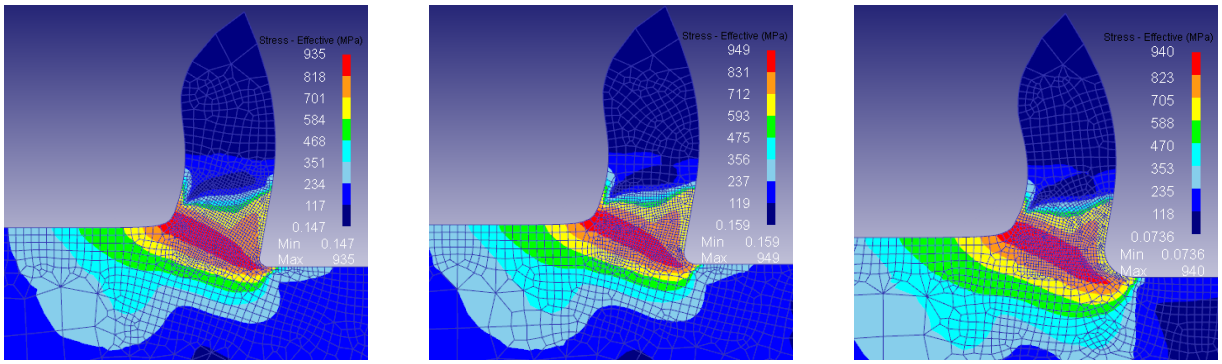

a) Cutting edge radius: 0.02 mm b) Cutting edge radius: 0.03 mm c) Cutting edge radius: 0.07 mm

Figure 4.38 – Chip geometry with stress field distribution for tool cutting radius analysis (AISI316L)

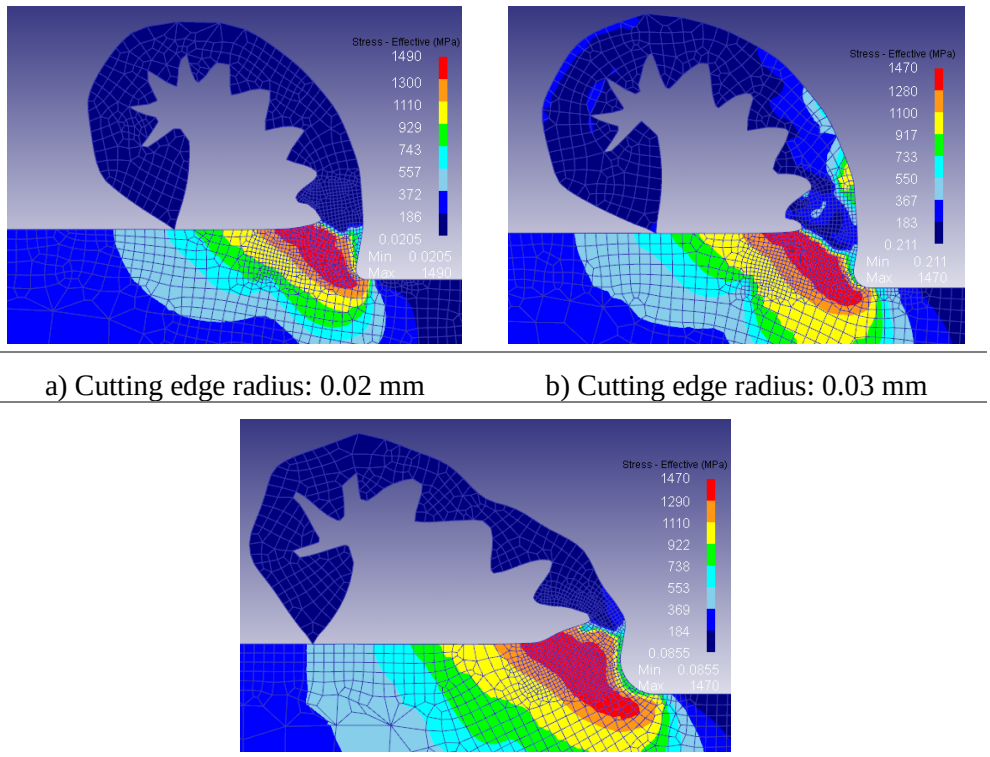

a) Cutting edge radius: 0.02 mm b) Cutting edge radius: 0.03 mm

c) Cutting edge radius: 0.07 mm

Figure 4.39 – Chip geometry with stress field distribution for tool cutting radius analysis (Ti6Al4V)

Even though that for cases a) and b) of Figure 4.37, Figure 4.38 and Figure 4.39 almost no difference can be identified in chip morphology, when compared with case c), a small increase on chip's curvature is noticeable. This supports the idea of a critical RTF since for cases a) and b), RTF is greater than 3.

4.3.4.3 Maximum Temperature Results

The maximum temperatures registered for the tool and workpiece are represented in the Figure 4.40.

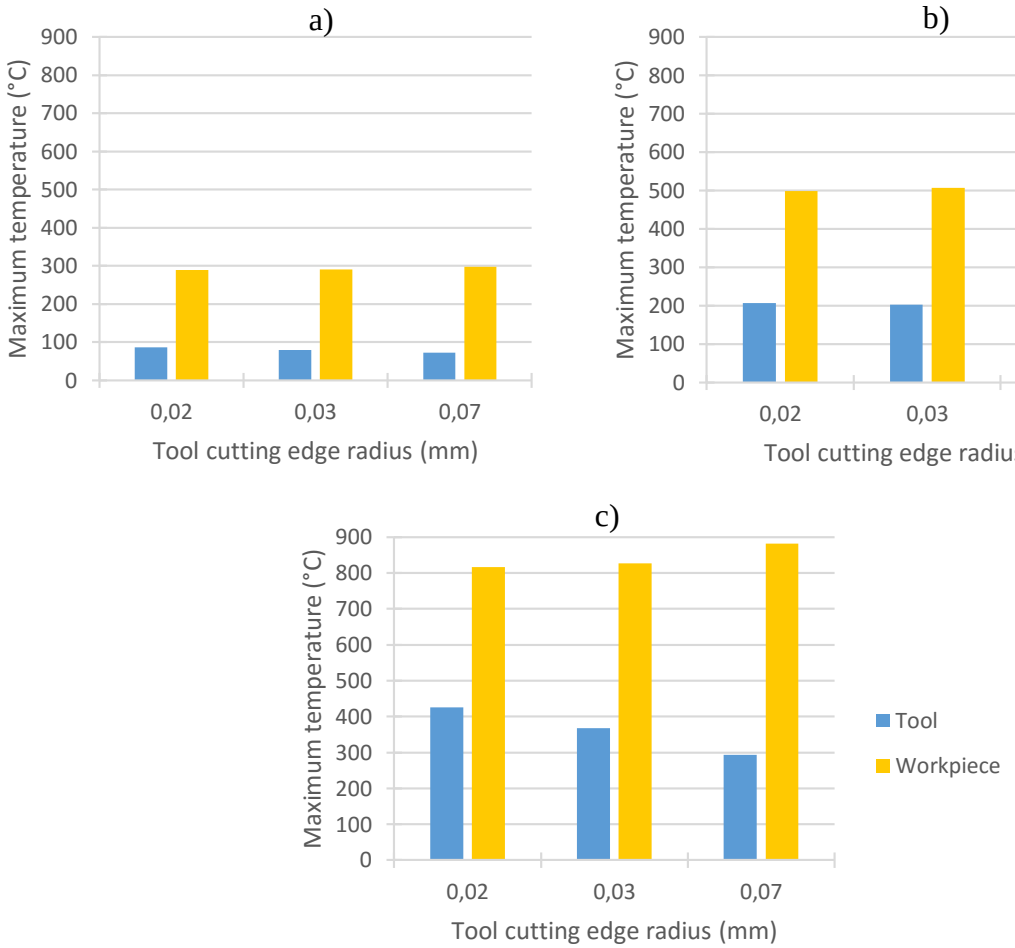

Figure 4.40 - Maximum workpiece and tool temperature sensitivity on variable tool cutting edge. a) Al7075-T351; b) AISI316L; c) Ti6Al4V

Similarly to the other analysed parameters, concerning the maximum reached temperature, there is almost no different between case a) and b) (0.02 and 0.03 mm, respectively). However, for a cutting edge radius of 0.07 mm, maximum temperature on the workpiece tends to increase while on the tool it tends to decrease for the 3 simulated metals. For the Ti alloy the tool temperature tends to decrease with tool cutting edge radius.

4.3.4.4 Average Shear Angle Results

Figure 4.41 represents the evaluation of the average shear angle with the cutting edge radius for the 3 simulated materials.

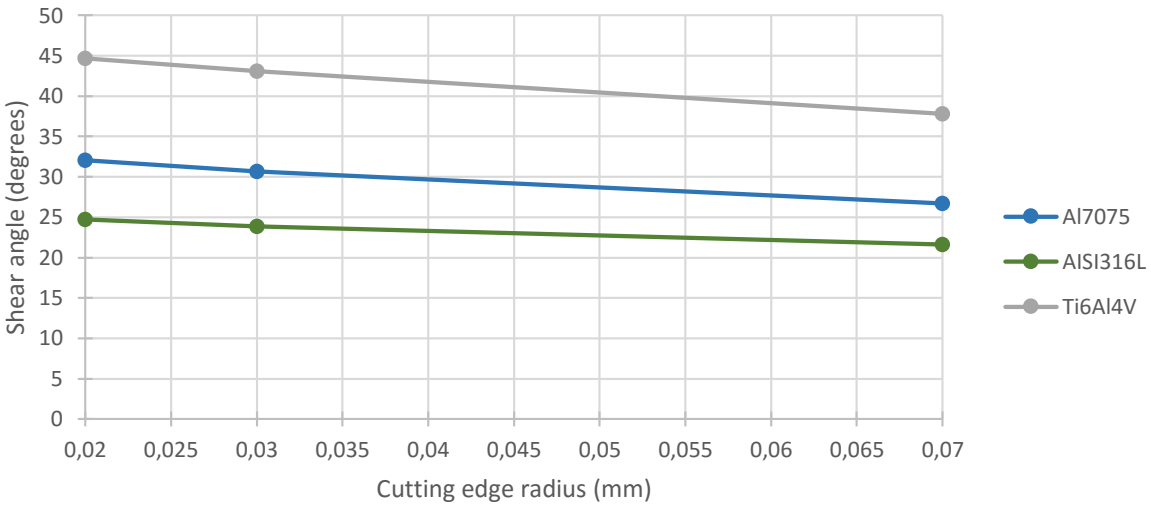

Figure 4.41 – Shear angle sensitivity on variable tool cutting edge radius for three different metals

Shear angle curve in Figure 4.41 supports load results for this sensitivity analysis: a smaller shear angle results in a bigger shear plane area. Since the shear strength is applied in this area, the shear force required to chip generation will increase. A decrease in the shear angle with the cutting radius is observed.

4.3.5 Friction

Shear friction is the predefined friction model on DEFORM™ 2D/3D. In this section, the shear friction coefficient variation is investigated in order to understand its influence on the tool load, chip geometry, maximum temperature and shear angle. Table 4.5 summarizes the considered parameters in the friction sensitivity analysis.

Table 4.5 – Summary of simulation parameters used in friction sensitivity analysis

Process	Cutting speed, v_c	100 m/min
	Uncut chip thickness, t	0.1 mm/rev
	Cutting length	1.125 mm
	Environment temperature	20ºC
	Environment convection coefficient	0.02 N/s/mm/ºC
Tool Parameters	Material	WC
	Mesh	1092 elements
	Dimensions	Figure 4.8
Workpiece Parameters	Material	Al7075 – T351 AISI316L Ti6Al4V
	Mesh	1548 elements
	Dimensions	4.5x1.0 mm
Contact	Friction (between Tool-Workpiece and Chip-Workpiece)	a) 0.4 (Shear model) b) 0.5 (Shear model) c) 0.6 (Shear model) d) 0.7 (Shear model) e) 0.8 (Shear model)
	Heat transfer coefficient (T-W and C-W)	40 N/s/mm/ºC
	Separation Criterion	Default
Numeric	Iteration method	Direct
	Solver	Skyline

4.3.5.1 Average Load Results

Figure 4.42 represents the average loads as a function of the shear friction coefficient for distinct materials, along with the scatter bands.

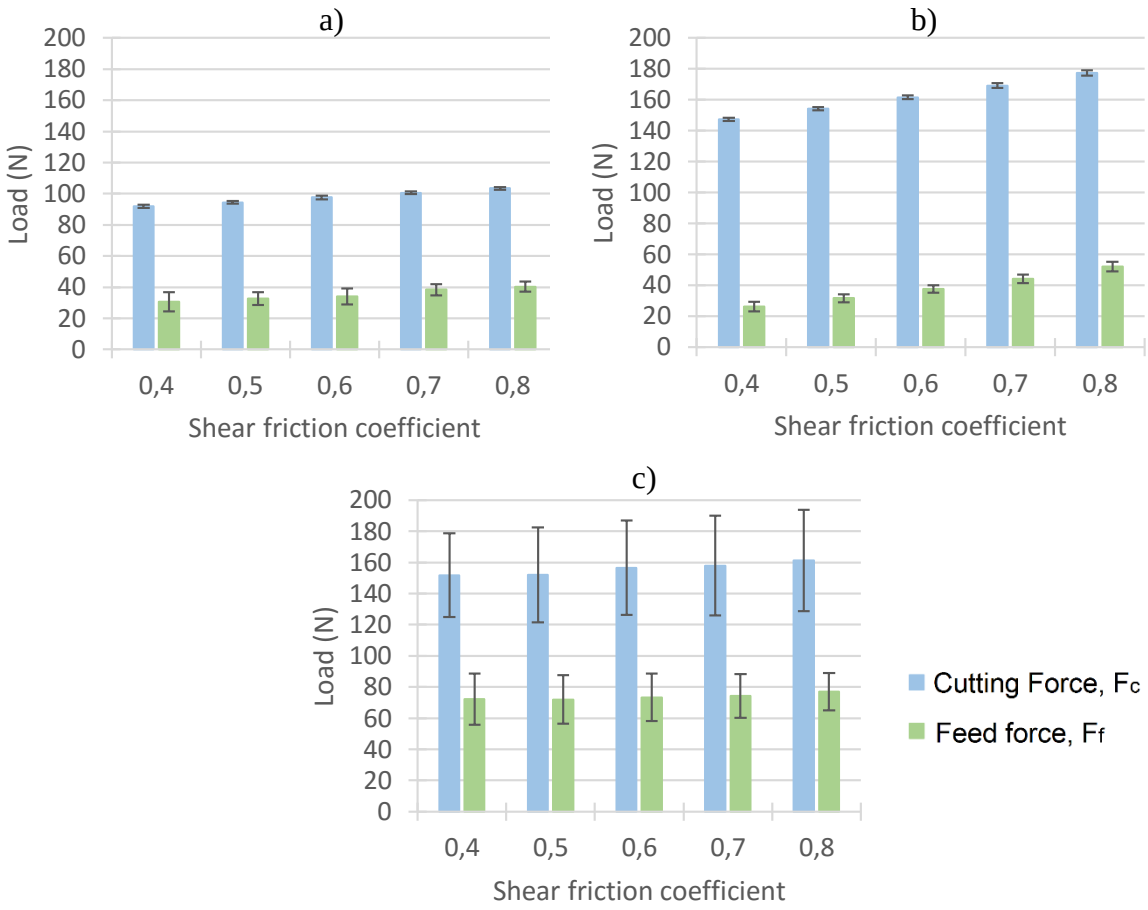

Figure 4.42 – Average load sensitivity on variable shear friction coefficient.

a) Al7075-T351; b) AISI316L; c) Ti6Al4V

In general, an increase in the cutting loads (cutting and feed force) with the shear friction coefficient is observed. However, in some cases, these increments in the cutting loads are not very significant for the range of shear friction coefficient tested.

4.3.5.2 Chip Geometry

Figure 4.43 to Figure 4.45 represent the chip geometry for various shear friction coefficients and covering three distinct materials.

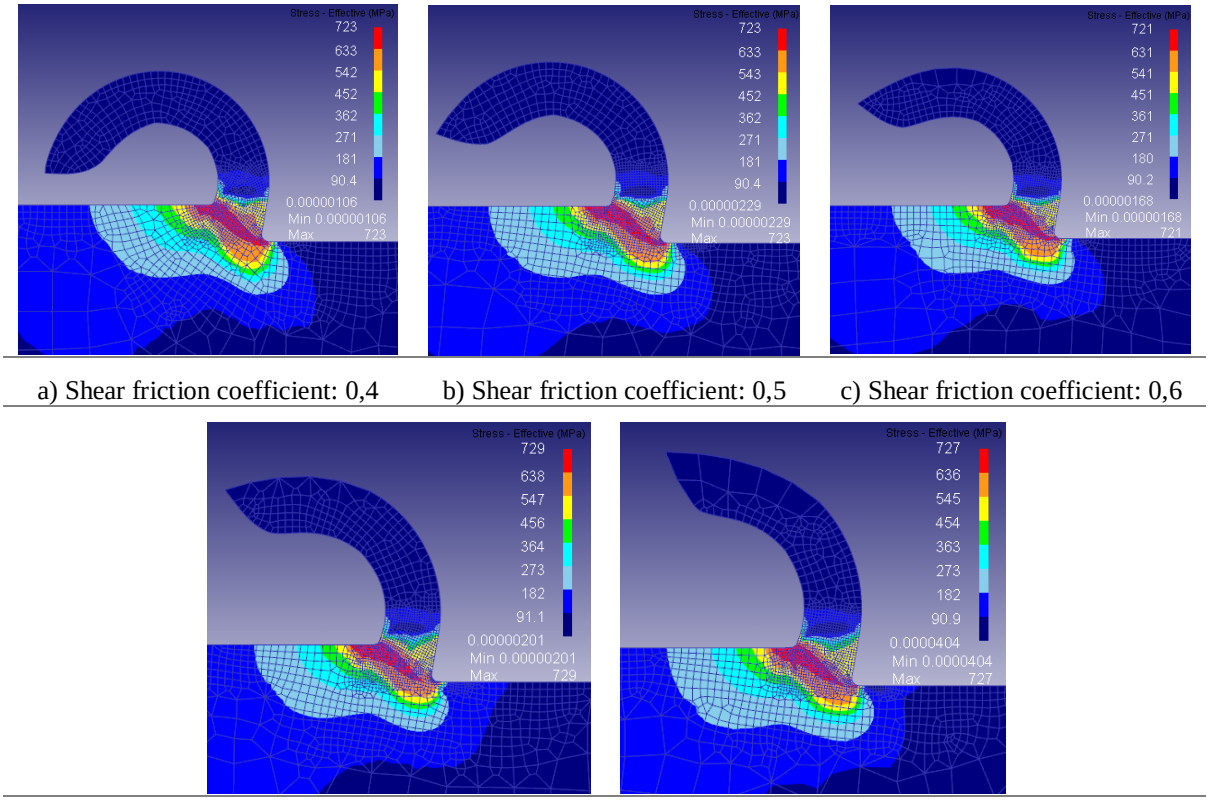

a) Shear friction coefficient: 0,4 b) Shear friction coefficient: 0,5 c) Shear friction coefficient: 0,6

d) Shear friction coefficient: 0,7 e) Shear friction coefficient: 0,8

Figure 4.43 – Chip geometry with stress field distribution for distinct shear friction coefficients (Al7075-T351)

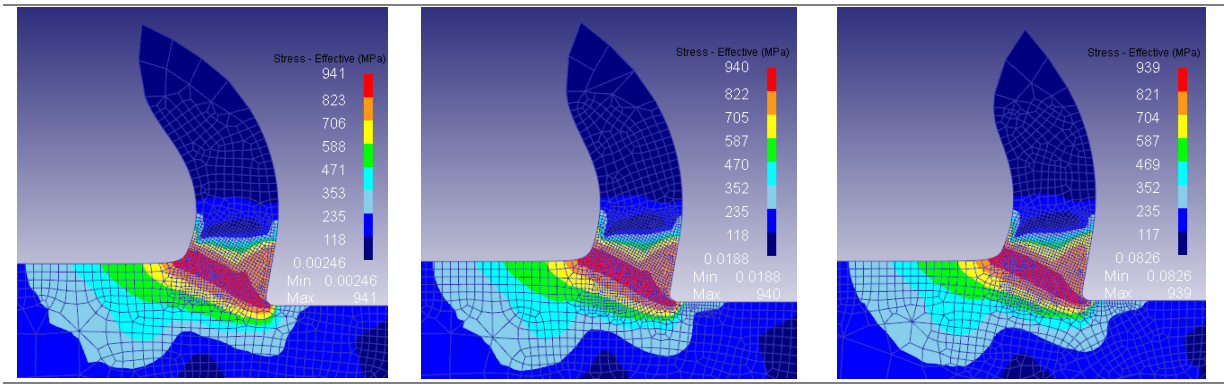

a) Shear friction coefficient: 0.4 b) Shear friction coefficient: 0.5 c) Shear friction coefficient: 0.6

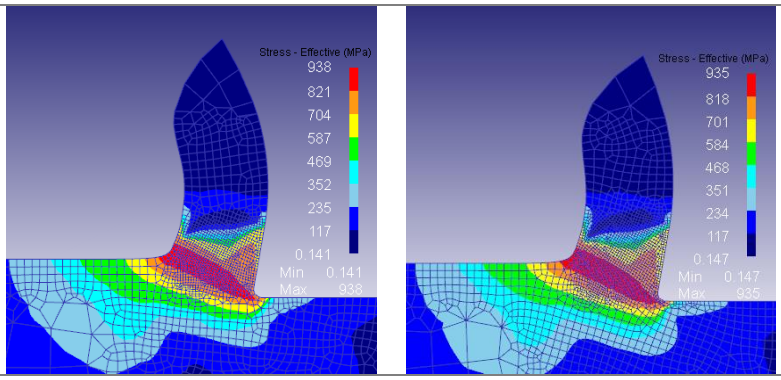

d) Shear friction coefficient: 0.7 e) Shear friction coefficient: 0.8

Figure 4.44 – Chip geometry with stress field distribution for distinct shear friction coefficients (AISI316L)

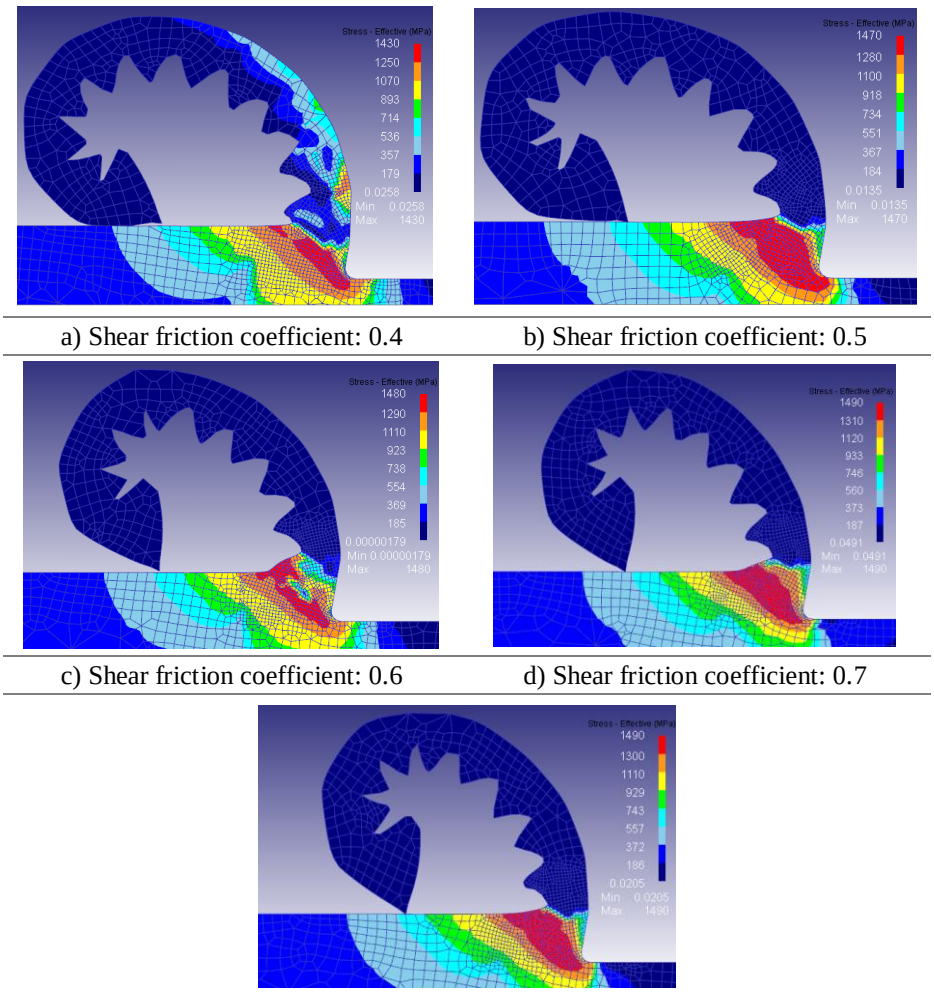

a) Shear friction coefficient: 0.4 b) Shear friction coefficient: 0.5

c) Shear friction coefficient: 0.6 d) Shear friction coefficient: 0.7

e) Shear friction coefficient: 0.8

Figure 4.45 – Chip geometry with stress field distribution for distinct shear friction coefficients (Ti6Al4V)

In general, the decrease in the shear friction coefficient results in an increase in the chip curvature.

4.3.5.3 Maximum Temperature Results

Figure 4.42 shows the maximum temperatures for both workpiece and tool registered for distinct shear friction coefficients.

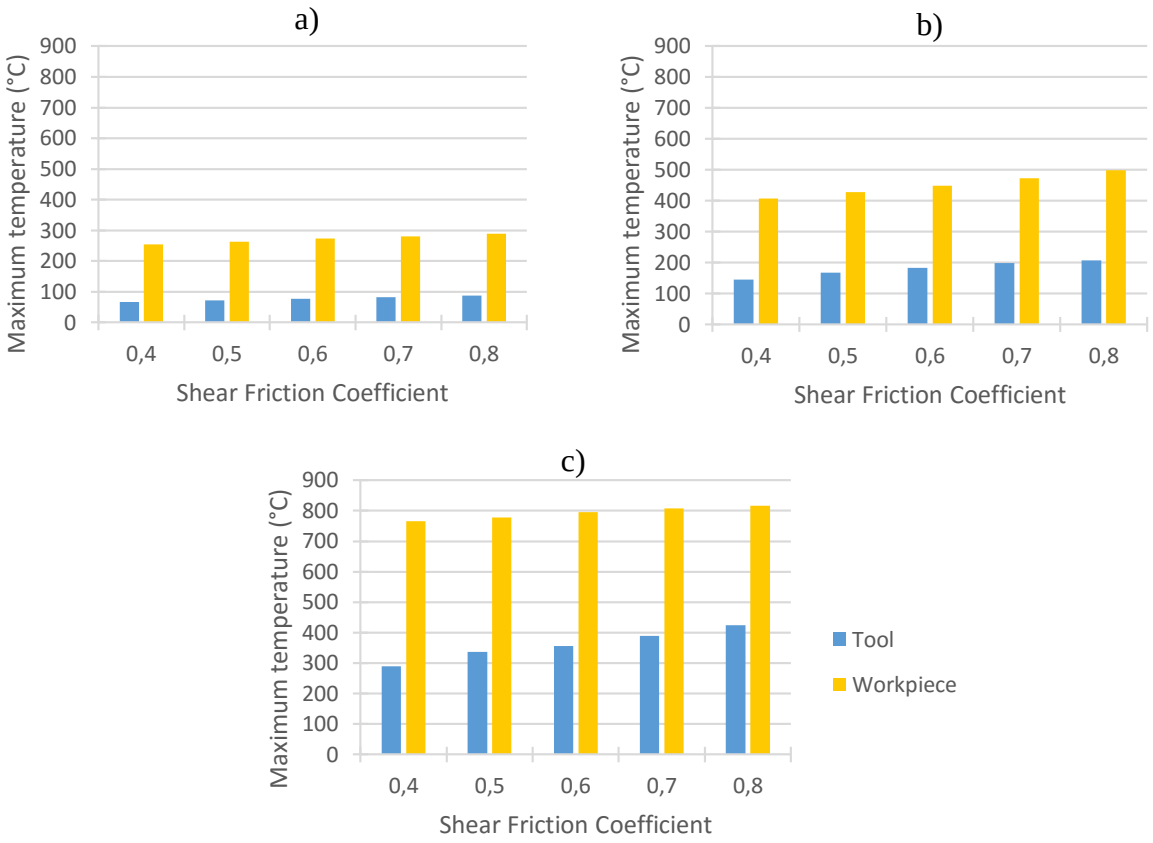

Figure 4.46 – Maximum workpiece and tool temperature sensitivity on shear friction coefficient.
a) Al7075-T351; c) AISI316L; d) Ti6Al4V

As expected, with the increase of shear friction coefficient, an increase in maximum reached temperature for both workpiece and tool are noticed.

4.3.5.4 Average Shear Angle Results

Finally, Figure 4.47 illustrates the evolution of the shear angle with the shear friction coefficient.

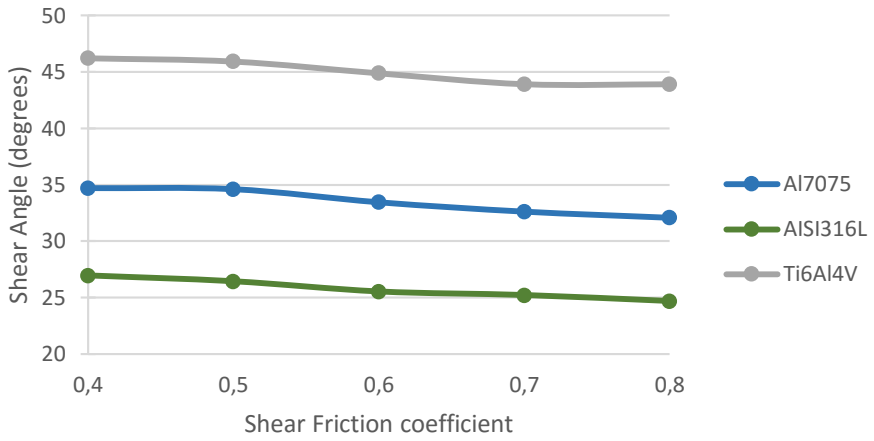

Figure 4.47 – Shear angle sensitivity on shear friction coefficient variation of three different metals

Due to the increase of the cutting forces caused by the increase of friction coefficient, a decrease of the shear angle is expected, which is supported by the obtained results shown in Figure 4.47.

4.3.6 Heat Transfer Coefficient

Understanding the influence of the heat transfer coefficient between the tool and workpiece is of great importance. This parameter was included in the sensitivity analysis in order to try to establish specific parameters for dry and wet conditions metal cutting. Table 4.6 summarizes the parameters considered in the sensitivity study.

Table 4.6 – Summary of simulation parameters used in heat transfer coefficient sensitivity analysis

Process	Cutting speed, v_c	100 m/min
	Uncut chip thickness, t	0.1 mm/rev
	Cutting length	1.125 mm
	Environment temperature	20ºC
	Environment convection coefficient	0.02 N/s/mm/ºC
Tool Parameters	Material	WC
	Mesh	1092 elements
	Dimensions	Figure 4.8
Workpiece Parameters	Material	Al7075 – T351 AISI316L Ti6Al4V
	Mesh	1548 elements
	Dimensions	4.5x1.0 mm
Contact	Friction (between Tool-Workpiece and Chip-Workpiece)	0.8 (Shear model)
	Heat transfer coefficient (T-W and C-W)	a) 20 N/s/mm/ºC b) 30 N/s/mm/ºC c) 40 N/s/mm/ºC d) 50 N/s/mm/ºC
	Separation Criterion	Default
Numeric	Iteration method	Direct
	Solver	Skyline

4.3.6.1 Average Load Results

Figure 4.48 represents the average cutting forces for different heat transfer coefficients. The analysis of the figure, shows inexistent or very small variation in the cutting forces.

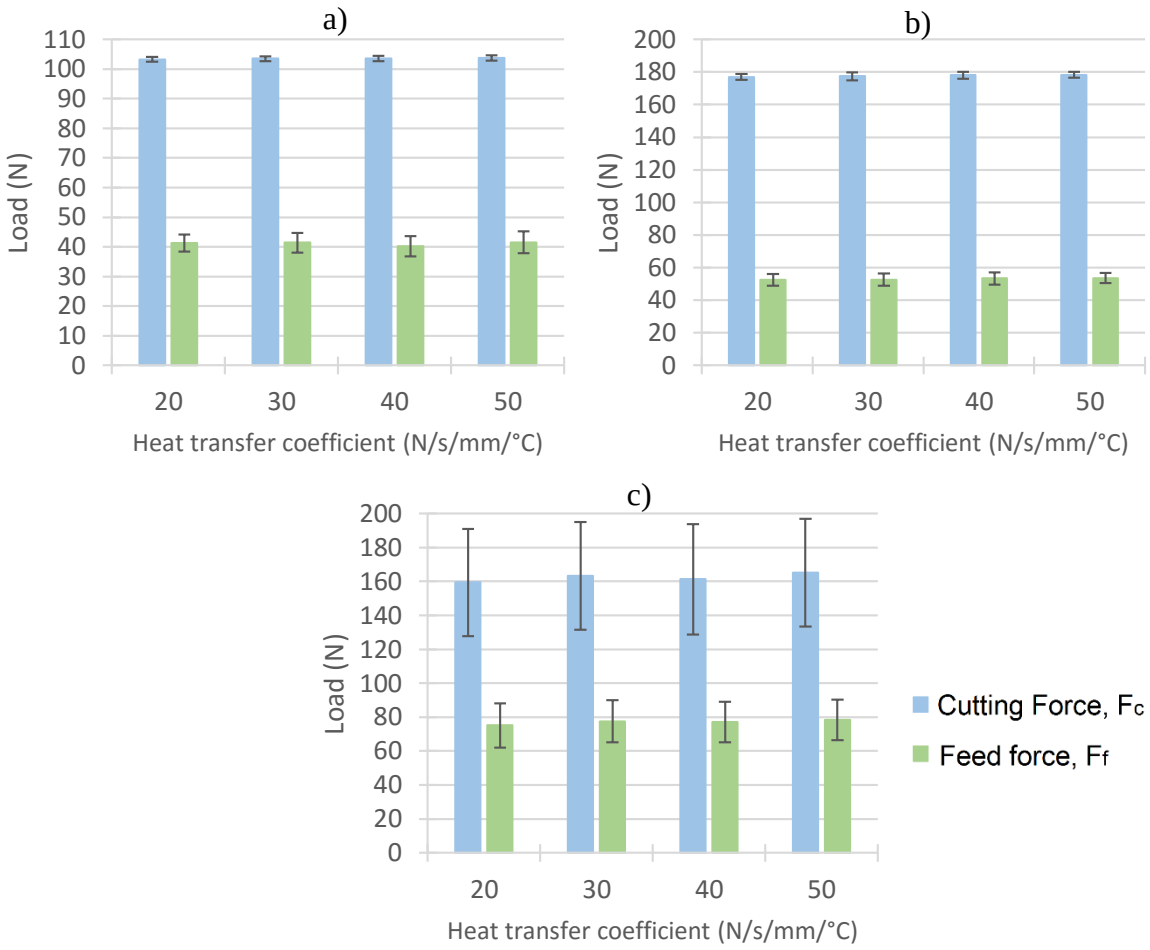

Figure 4.48 – Average loads obtained for variable heat transfer coefficient.
a) Al7075-T351; b) AISI316L; c) Ti6Al4V

The low variation of the cutting forces for different heat transfer coefficients suggests that a more complex combination of thermal and friction parameters needs to be achieved in order to simulate metal cutting in wet conditions.

Since the variation of heat transfer coefficient does not play a significant influence on the obtained results for maximum temperature, chip geometry and average shear angle, those will be omitted.

4.4 Numerical parameters

4.4.1 Mesh element size

Due to the large computation time of metal cutting finite element simulations with DEFORM™ it is relevant to understand mesh element size influence on the simulation process: if a finer mesh contributes to a significant improve in precision and/or accuracy of results and what should be the ideal element size?

For this purpose, two different combinations of element size for tool and workpiece (described in Table 4.7) were tested: MS1 and MS2.

Table 4.7 – Summary of simulation parameters used in element size sensitivity analysis

Process	Cutting speed, v_c	100 m/min
	Uncut chip thickness, t	0.1 mm/rev
	Cutting length	1.125 mm
	Environment temperature	20ºC
	Environment convection coefficient	0.02 N/s/mm/ºC
Tool Parameters	Material	WC
	Mesh	a) 1092 elements (MS1) b) 5111 elements (MS2)
	Dimensions	Figure 4.8
Workpiece Parameters	Material	Al7075 – T351 AISI316L Ti6Al4V
	Mesh	a) 1548 elements (MS1) b) 3391 elements (MS2)
	Dimensions	4.5x1.0 mm
Contact	Friction (between Tool-Workpiece and Chip-Workpiece)	0.8 (Shear model)
	Heat transfer coefficient (T-W and C-W)	40 N/s/mm/ºC
	Separation Criterion	Default
Numeric	Iteration method	Direct
	Solver	Skyline

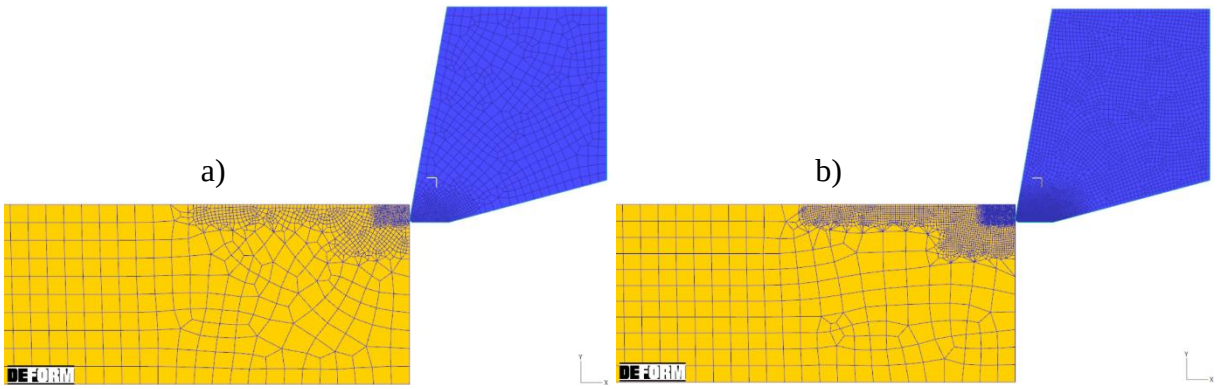

Figure 4.50 – Defined meshes for mesh element size sensitivity analysis. MS1(a) and MS2(b)

4.4.1.1 Average Load Results

Figure 4.51 represents the evolution of the cutting loads with the mesh size.

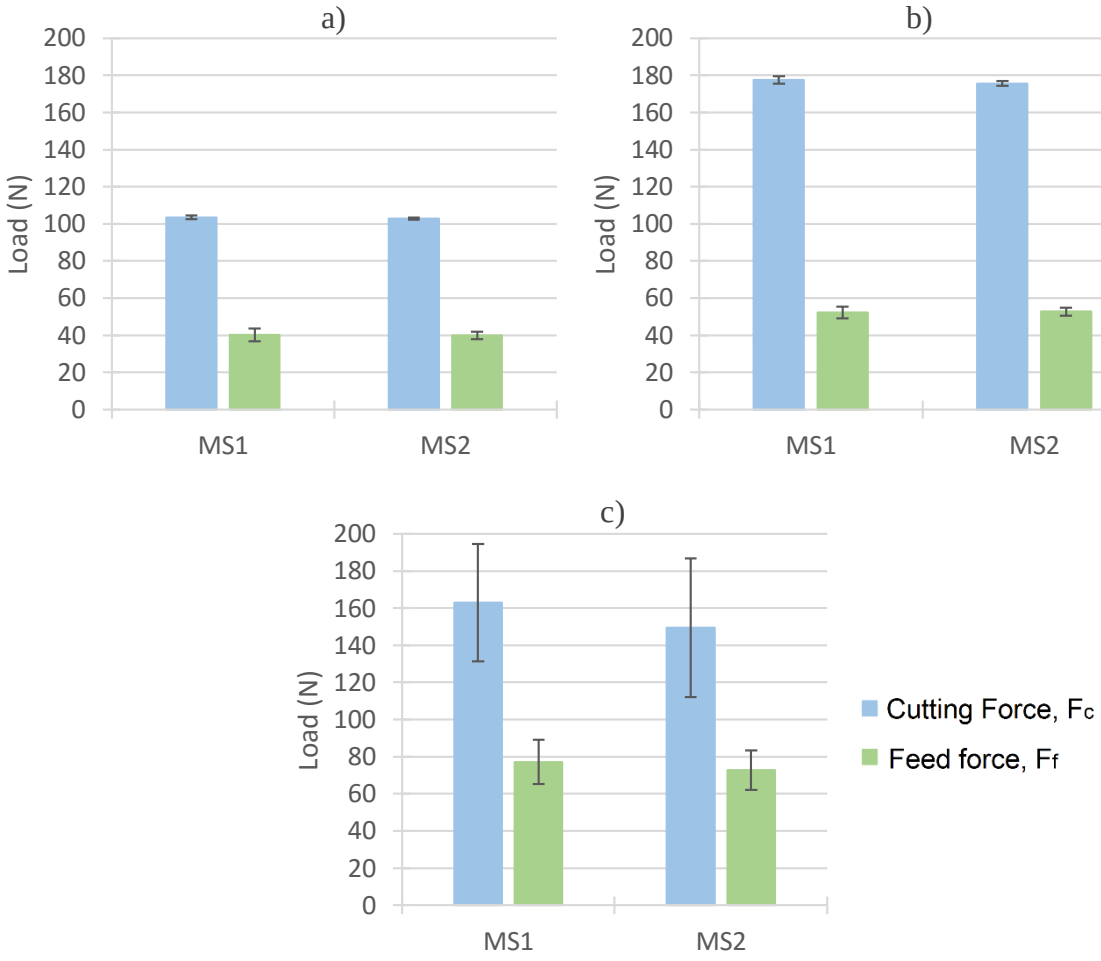

Figure 4.51 – Average load sensitivity on variable mesh element size for the tool and workpiece.

a) Al7075-T351; b) AISI316L; c) Ti6Al4V

Concerning the simulation of the aluminium alloy, negligible differences in the cutting loads were observed. The same result is also appointed for the AISI316L steel. For the Titanium alloy a very slight difference in feed and cutting forces can be noticed. This is related with the fact that the software's intuitive interface gives the user the possibility of mesh element size choice from a range which the minimum (MS1) is already an appropriate mesh when it comes to

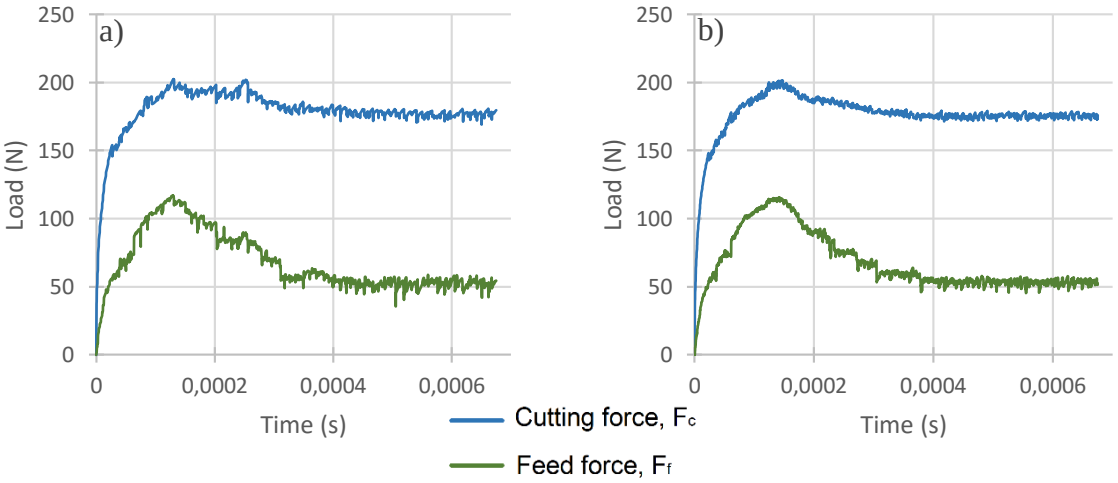

Figure 4.52 – Load-time curves for AISI316L with mesh settings MS1 (a) and MS2 (b)

Load curves displayed on Figure 4.52 show that with more refined mesh, mesh regeneration steps have less influence on fluctuation of output results.

Load curves show small fluctuation caused by mesh regeneration steps throughout the simulation. Increasing the number of elements results in a smaller size for each element and therefore a finer mesh.

Concerning the chip geometry, maximum temperatures and shear angle computations, the two mesh sizes did not produce significant changes worth to be reported. Therefore, the respective results are not shown in this section.

4.4.2 Iteration Method

This section focus on the simulation of the same numerical models varying the used iteration method. As seen it Table 4.8, these can vary between Direct iteration method and Newton-Raphson.

Table 4.8 – Summary of simulation parameters used in iteration method sensitivity analysis

Process	Cutting speed, v_c	100 m/min
	Uncut chip thickness, t	0.1 mm/rev
	Cutting length	1.125 mm
	Environment temperature	20ºC
	Environment convection coefficient	0.02 N/s/mm/ºC
Tool Parameters	Material	WC
	Mesh	1092 elements
	Dimensions	Figure 4.8
Workpiece Parameters	Material	Al7075 – T351 AISI316L Ti6Al4V
	Mesh	1548 elements
	Dimensions	4.5x1.0 mm
Contact	Friction (between Tool-Workpiece and Chip-Workpiece)	0.8 (Shear model)
	Heat transfer coefficient (T-W and C-W)	40 N/s/mm/ºC
	Separation Criterion	Default
Numeric	Iteration method	a) Direct b) Newton-Raphson
	Solver	Skyline

4.4.2.1 Average Load Results

Figure 4.53 shows the average load results for two different iteration methods available in the software for three distinct metals.

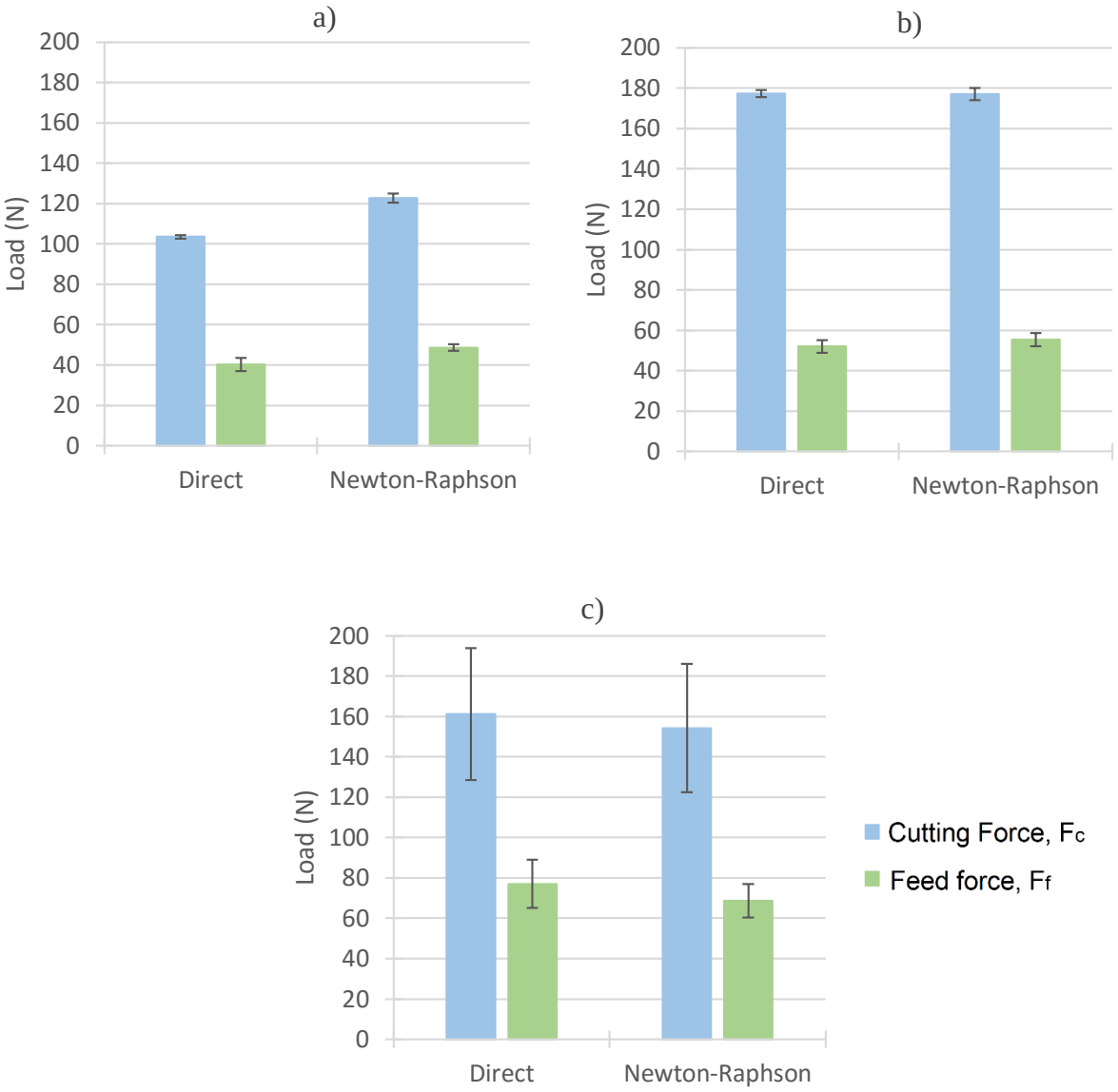

Figure 4.53 – Average load sensitivity on variable iteration method for the tool and workpiece.
a) Al7075-T351; b) AISI316L; c) Ti6Al4V

It is observed that, despite small changes, the iterative method does not have a big influence on the average load results. However, it is interesting that depending on the material, average load forces with a different iterative method can either increase, decrease or not change at all.

5 EXPERIMENTAL PROCEDURE

5.1 Material characterization for turning simulation

The goal of this chapter is to characterize the aluminium alloy AlSi9Cu3 that was subject of a machinability study in [75]. This alloy exclusively obtained by casting is suitable for applications that demand good mechanical properties at elevated temperatures and low thermal expansion coefficient. Table 5.1 summarizes the expected chemical composition of this cast alloy.

Table 5.1 – Chemical composition of cast aluminium alloy AlSi9Cu3 according to NP EN 1706 [76]

Chemical composition (mass %)														
	Si	Fe	Cu	Mn	Mg	Cr	Ni	Zn	Pb	Sn	Ti	Other		Al
Minimum	8.0		2.0		0.05							Each	Total	
Maximum	11.0	1.3	4.0	0.55	0.55	0.15	0.55	1.2	0.35	0.25	0.25	0.05	0.25	Rest

In the current study, two types of tests were performed with this material. The first type, aiming for material characterization consisted of compression tests performed at quasi-static conditions and room temperature. The second type consisted of machining tests, aiming friction coefficient evaluation, where the orthogonal cutting conditions were considered.

5.1.1 Compression tests

Experimental compression tests in quasi-static conditions were conducted in order to characterize the material flow stress. For this purpose, small cylindrical test specimens were placed in the compression system equipped with a load cell connected to a computer for force/pressure and displacement acquisition. Small ϕ6x6 mm test specimen cylinders (Figure 5.1) were machined from bigger cast aluminium cylinders, using a lathe.

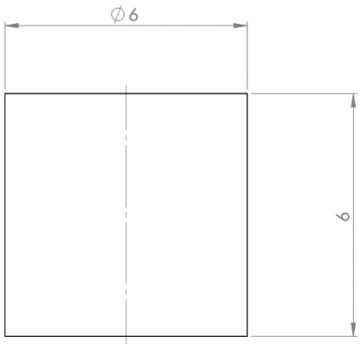

Figure 5.1 – Test specimen used in upsetting test

The experimental procedure was the following:

- Initial test specimen diameter and height measurements;
- Cleaning and lubrication of test specimen;
- Placing the test specimen in the centre of the lower compression plate;
- Compression test with load and displacement data acquisition;
- Final diameter and height measurement.

Figure 5.2 illustrates the experimental testing system (a), the specimen before (b) and after testing (c).

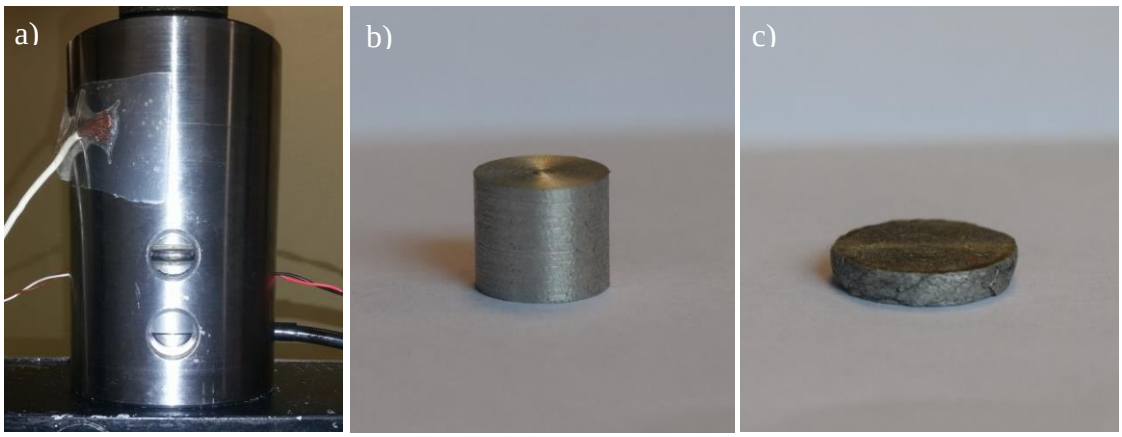

Figure 5.2 – a) Compressed test specimen inside compression system; b) test specimen before compression; c) test specimen after compression

Four tests were successfully conducted and the obtained stress-strain curves show reasonable repeatability. It is possible to observe in the specimen after testing some cracks at the external surface of the specimen. Figure 5.3 illustrates the resulting true stress-strain curves obtained for the test specimens which were obtained until a strain of 1.

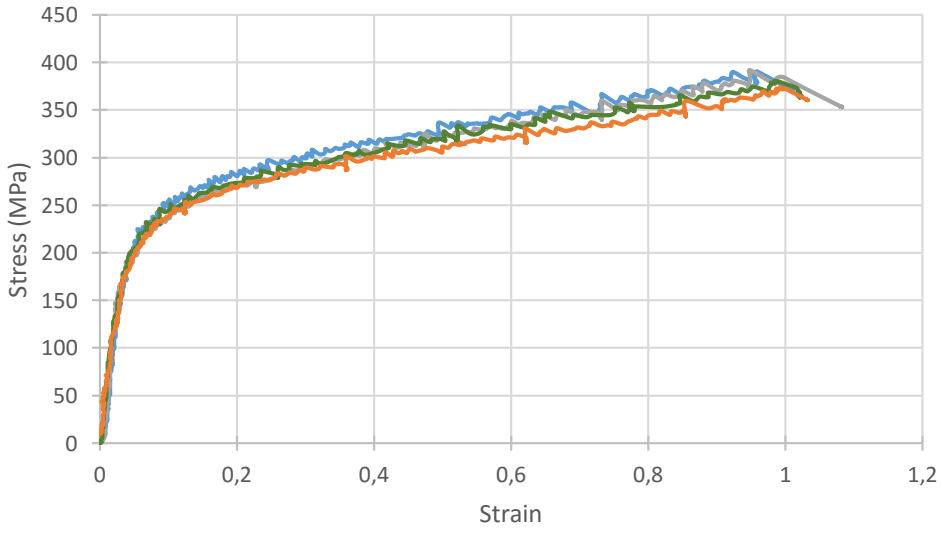

Figure 5.3 – Stress-strain curves for the 4 compression tests

5.2 Friction characterization for turning simulation

Main purpose of recreating orthogonal cutting in a lathe machine is to measure cutting and feed forces for similar cutting parameters of the study led by Rui Soares [75]. These can be used in friction coefficient determination that works as an input for FEM simulations to be presented in Chapter 6. In order to recreate orthogonal cutting in a turning operation, a tool with a rake angle of 0º was approached to the workpiece with a cutting edge position angle of 90º relatively to the direction of feed. This way, there is only two force components: cutting and feed forces. It is important to mention that these forces act on the contact area between tool and workpiece. However, for simplification purposes it is considered that the resultant forces are applied in a single point.

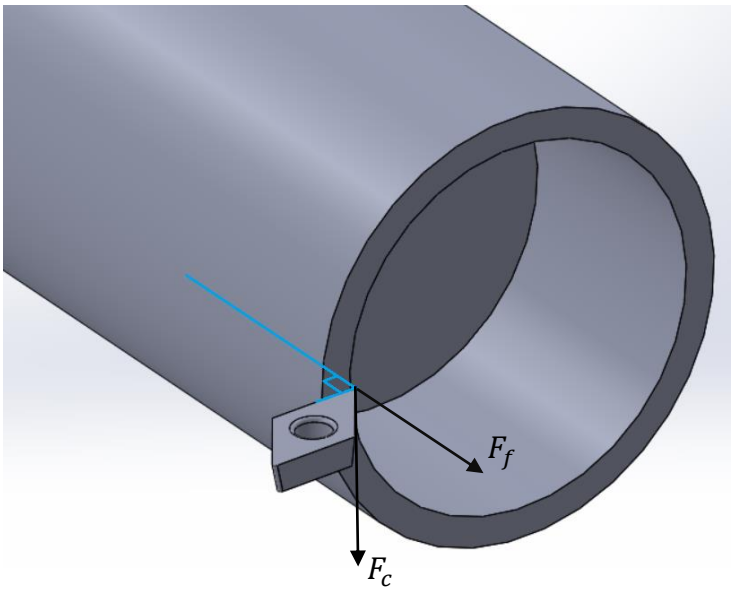

Figure 5.4 – Geometry and forces of orthogonal cutting through face turning

As reviewed in Chapter 2, by Merchant's circle diagram, friction coefficient μ is defined analytically by Eq. 7,

$$\mu = \frac{F_c \tan\alpha + F_f}{F_c - F_f \tan\alpha} \quad (7)$$

where F_{tc} is the cutting or thrust force and F_{fc} the feed or tangential force.

Tool's rake angle being zero ($\alpha = 0$), simplifies Eq. 7, which results directly in:

$$\mu = \frac{F_f}{F_c} \quad (54)$$

5.2.1 Orthogonal cutting tests

In order to achieve the best possible conditions of orthogonal cutting, cylindrical hollow specimens with a wall thickness equal to the insert's cutting edge was prepared. In order to keep a stable cutting operation, the hollow length described as "*" in Figure 5.5 was increased according to the elapse of the process.

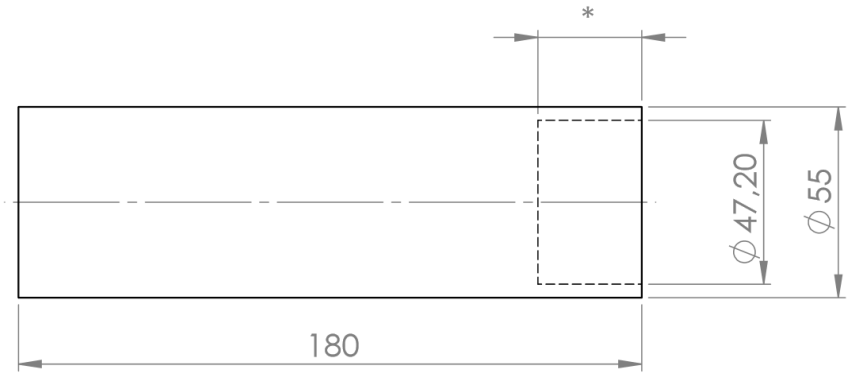

Figure 5.5 –Specimens for orthogonal cutting tests

To keep orthogonal cutting tests conditions as close as possible to the machinability tests simulated in Chapter 6, the same PCD inserts were used. The used cutting parameters, shown in Table 5.2, allow measuring friction coefficient in the same speed range of the already mentioned machinability tests of Chapter 6. It is important to note that the displayed cutting speed is based on measured dimensions of the specimen from Figure 5.5.

Table 5.2 – Cutting parameters used in orthogonal cutting tests

Test Name Code	n(rpm)	f (mm/rev)	v_c (m/min)
O.3.1.1	2500	0.05	424 - 369 Average: 396
O.3.12		0.14	424 - 369 Average:396
O.3.1.3		0.25	424 - 369 Average:396
O.3.2.1	900	0.05	153 - 133 Average:143
O.3.2.2		0.14	153 - 133 Average:143
O.3.2.3		0.25	153 - 133 Average:143

The tests were conducted in a mechanical parallel lathe EFI DU20 with 5.9 kW of power and 2500 rpm of maximum speed, in the machine workshops of DEMec. Force determination requires usage of different components. Load cells, signal amplifiers and data acquisition system were also used (see Figure 5.6 and Table 5.3).

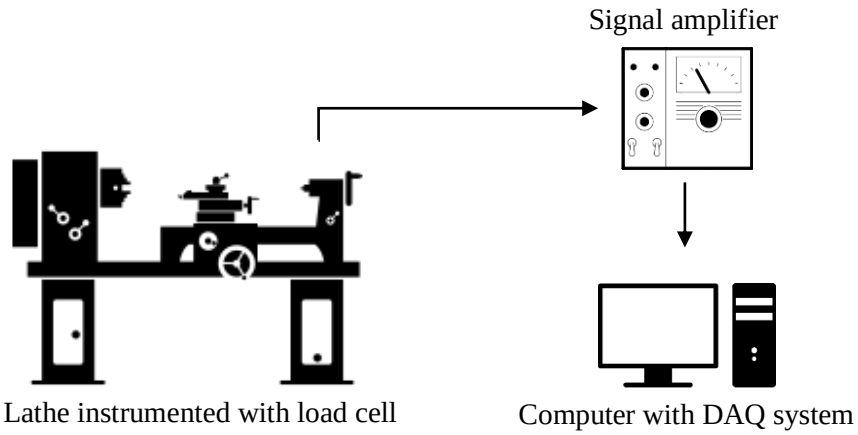

Figure 5.6 – Scheme of different used components

Table 5.3 – Technical designation of used components

Components	
Load cell	*KISTLER 9257B*
Signal amplifier	*KISTLER 5807A*
Data acquisition system	*HBM Spider8*

Figure 5.7 gives a detail view of the experimental setup.

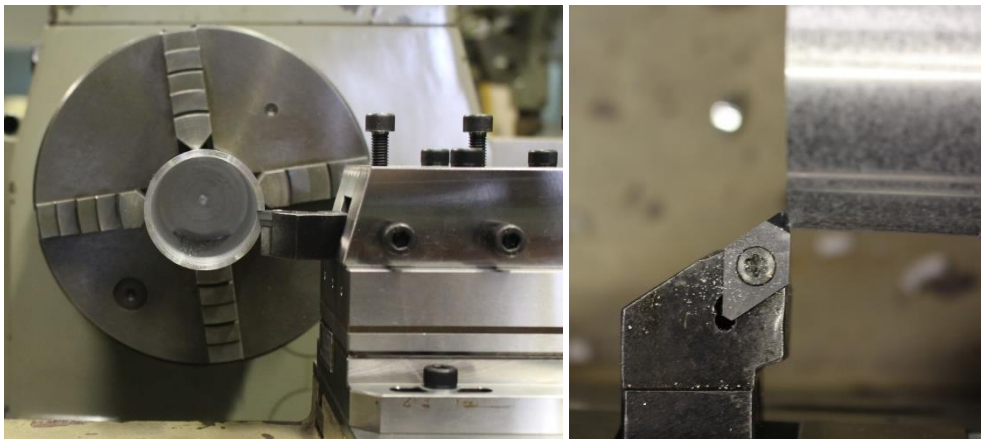

Figure 5.7 – Detailed setup of orthogonal cutting tests

The obtained data was organised in series of graphs like the one shown in Figure 5.8. As it was mentioned before, in an attempt of creating orthogonal cutting conditions, radial force should be zero, which is successfully achieved.

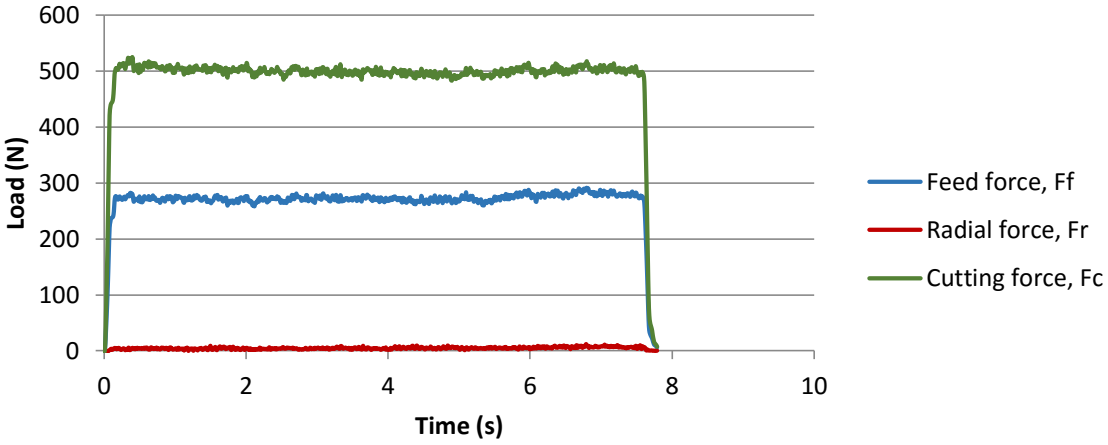

Figure 5.8 – Example of obtained results for cutting conditions of v_c=143 m/min (avg) and f=0.25 mm/rev (O.3.2.3)

In order to obtain less deviated average forces, initial and final force values were not taken into consideration, which means that the average results shown in Table 5.4 correspond only to about 90% of the total machining time for each test.

Table 5.4 – Average loads and calculated friction coefficient for each test

Test name code	Average Load (N)		Friction coefficient $\boldsymbol{\mu} = \left(\frac{F_f}{F_c}\right)$
	F_f	F_c	
O.3.1.1	87.0	134.5	0.65
O.3.1.2	151.3	295.6	0.51
O.3.1.3	219.9	476.6	0.46
O.3.2.1	83.0	141.5	0.59
O.3.2.2	179.9	316.5	0.57
O.3.2.3	273.5	500.9	0.56
Average:	-	-	**0.56**

Figure 5.9 and Figure 5.10 exhibit average loads and friction coefficients for each test. It is observed that cutting and feed forces increase with feed rate, while friction coefficient decreases. However, the effect of feed is less important for lower cutting speeds than for higher cutting speeds. Additionally, a relationship between average cutting speed and average friction coefficient can be established: for higher cutting speeds, a bigger deviation of friction coefficient values is noticed.

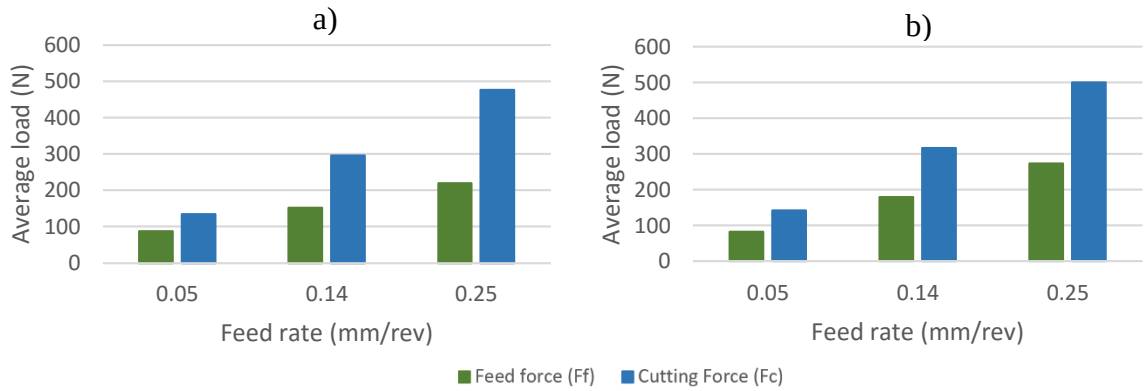

Figure 5.9 – Average loads for each feed rate and cutting speed:

a) 390 m/min, tests O.3.1.1 to O.3.1.3

b) 143 m/min, tests O.3.2.1 to O.3.2.3

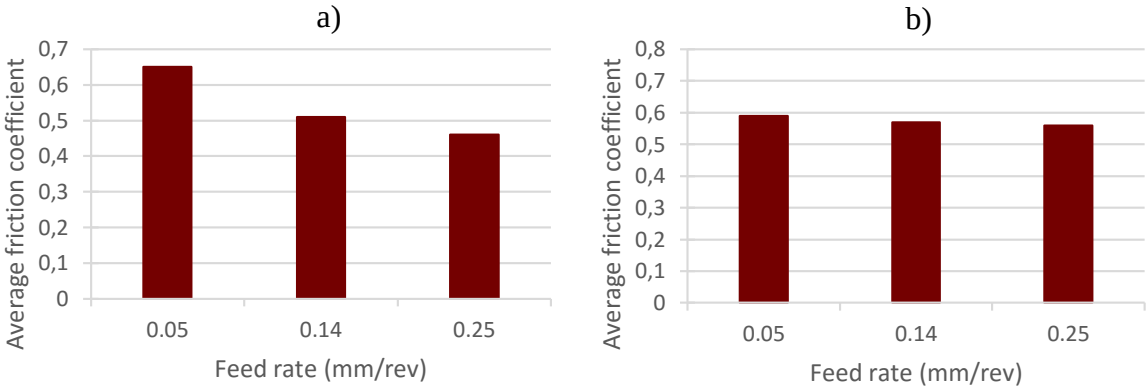

Figure 5.10 – Friction coefficient for each feed rate and cutting speed:

a) 390 m/min, tests O.3.1.1 to O.3.1.3

b) 143 m/min, tests O.3.2.1 to O.3.2.3

It was observed that the friction coefficient varied between values of 0.47 and 0.64 with an average value of 0.56.

6 TURNING SIMULATION WITH EXPERIMENTAL VALIDATION

6.1 Introduction

In this section, in order to verify the capabilities of the commercial FEM software DEFORM™, 2D and 3D turning simulations are conducted in order to recreate the experimental machinability study led by Rui Soares [75], on the cast aluminium alloy AlSi9Cu3. Also, this is a first step aiming toward the simulation of 3D metal cutting tests on the mentioned aluminium alloy with PCD inserts with 3D chip breakers. However, in this thesis, the PCD inserts with flat rake face were used for simulation purposes. Table 6.1 summarizes the cutting parameters tested in [75] for this insert.

Table 6.1 – Cutting parameters used in machining tests [75]

n (rpm)	Depth of cut (mm)	Feed rate (mm/rev)	Cutting speed (m/min)
2500	0.25	0.05	432
		0.14	428
		0.25	424
	0.5	0.05	420
		0.14	412
		0.25	404
	1.5	0.05	397
		0.14	373
		0.25	350
900	0.25	0.05	117
		0.14	116
		0.25	115
	0.5	0.05	113
		0.14	110
		0.25	107
	1.5	0.05	105
		0.14	96
		0.25	88

As mentioned in the first chapter, orthogonal cutting is considered a reasonable depiction of machining operations. Creating 2D and 3D models for the same operation (turning) with the same cutting parameters, will allow the evaluation of how precise that portrayal is. It is, however, necessary to establish a relationship between the two different processes.

Figure 6.1 gives an equivalence between the 2D orthogonal cutting model and the 3D turning operation.

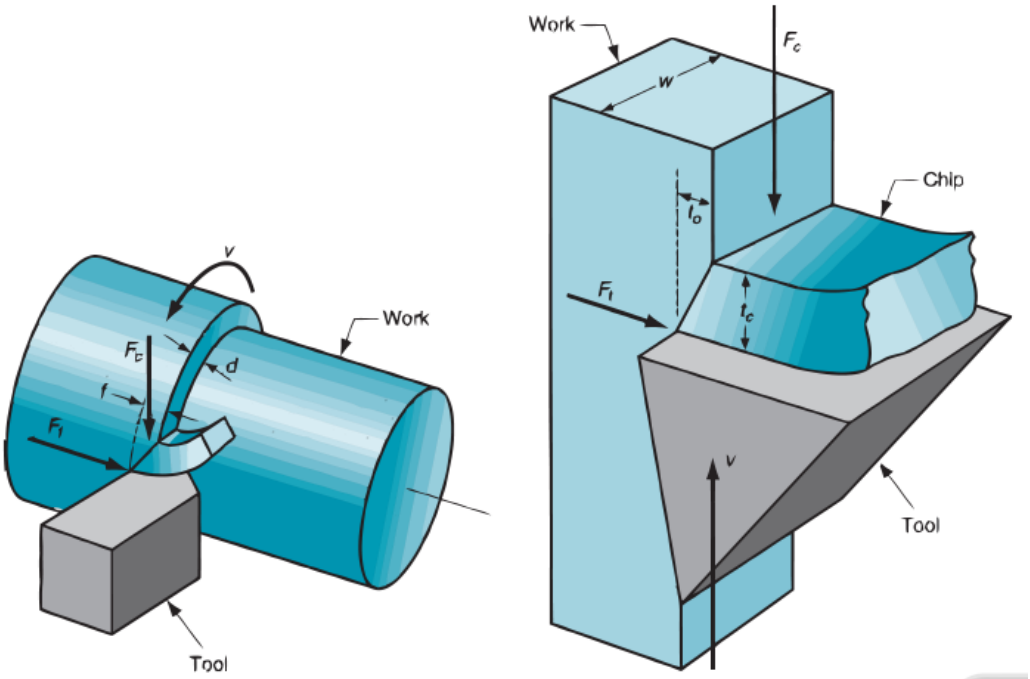

Turning		**Orthogonal cutting**
Feed rate, f	=	Uncut chip thickness, t
Depth of cut, d	=	Width of cut, w
Cutting speed, v	=	Cutting speed, v
Feed force, F_f	=	Thrust force F_t

Figure 6.1 – Correspondence between turning and orthogonal cutting models [79]

6.2 Workpiece material and geometry

With the aim of understanding the weight that workpiece material component has on the results of machining simulation, two different workpiece materials are going to be used. In Chapter 5, an attempt to mechanically characterize cast aluminium alloy AlSi9Cu3 was done for this exact purpose. Even though that characterization was at a quasi-static condition, high strain-rate effect was accounted in the flow stress curves using an empirical approach based on other similar materials data.

Also, the most similar material from software's library was selected in order to establish a reference standard. A Silicon based cast aluminium alloy (Al20Si) was chosen for this purpose. It is important to note that even though it is the only Silicon based cast aluminium alloy in the software material library, it has twice the Silicon content of the aluminium alloy used in the experimental tests.

6.2.1 AlSi20

This section presents the flow stress curves available in DEFORM™ material library for the cast aluminium alloy AlSi20. The flow stress is characterized for different strain-rates and temperatures. The data is, however, defined in a tabular form. Figure 6.2 and Figure 6.3 illustrate that data in graphical form.

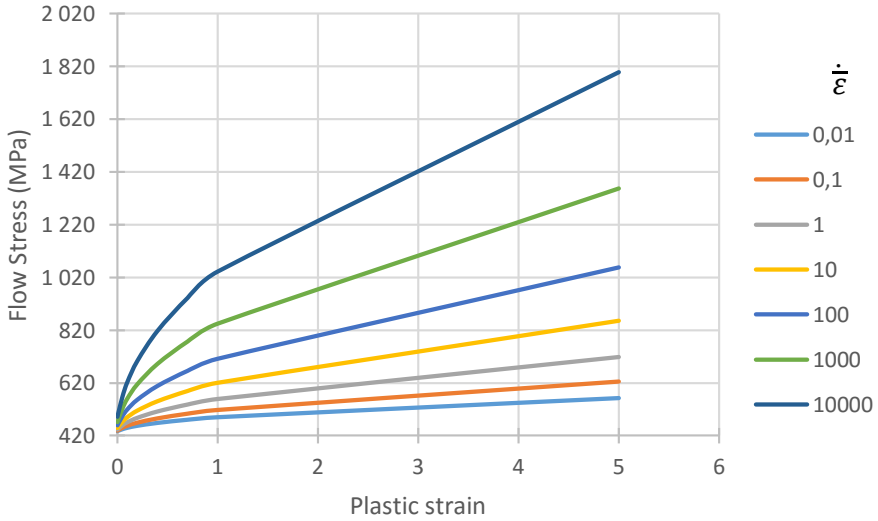

Figure 6.2 – Flow stress curves of AlSi20 for different strain rates and a fixed temperature of 20ºC

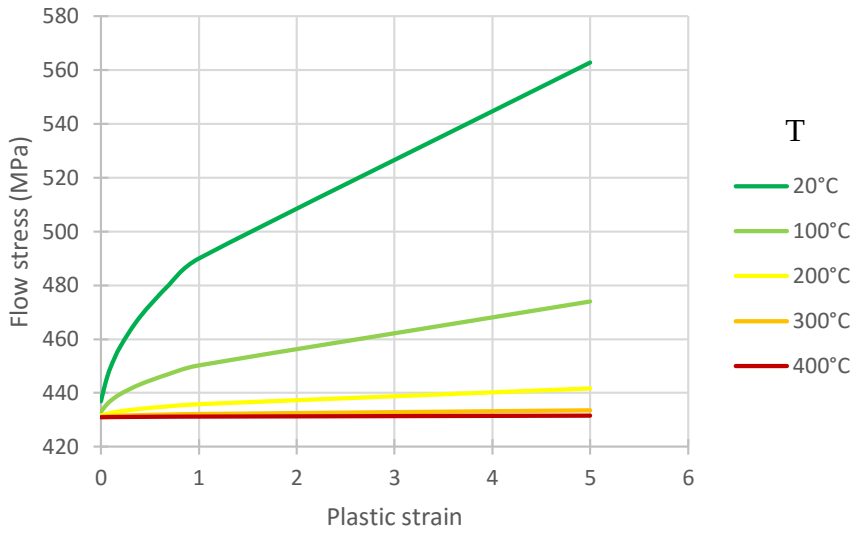

Figure 6.3 – Flow stress curves of AlSi20 for different temperatures and a fixed strain rate (0,01)

This material shows a significantly higher initial flow stress than the measured for the AlSi9Cu3 alloy at room temperature and low strain-rate.

6.2.2 AlSi9Cu3

Unlike the previous material, the cast aluminium alloy AlSi9Cu3 is not available in DEFORM™ material library. Therefore, an effort to define the material's flow stress at high strains, strain-rates and temperature was made. Compression tests shown in Chapter 5 were the starting point of this iterative/inverse material characterization.

In order to use Johnson and Cook flow stress material model to obtain flow stress values for high strain-rates, elastic strain effect is not taken in consideration. For that, elastic strain was calculated according to the relation between stress and strain shown in Eq. 55 and then subtracted to the total strain, to result the plastic strain.

$$\varepsilon = \frac{\sigma}{E} \tag{55}$$

It is important to mention that elasticity modulus was underestimated by the compression tests. Therefore, in Eq. 55 an apparent elasticity modulus, determined by compression results examination, was used.

For the obtained stress-strain curves free of elastic strain, a power trend line was defined (see Figure 6.4), which allowed to get average B and n parameters of the Johnson-Cook flow stress model:

$$\overline{\sigma} = \underbrace{[A + B(\overline{\varepsilon})^n]}_{\text{Elasto-Plastic term}} \quad \underbrace{\left[1 + C\ ln\left(\frac{\dot{\overline{\varepsilon}}}{\dot{\varepsilon}_0}\right)\right]}_{\text{Viscosity term}} \quad \underbrace{\left[1 - \left(\frac{T - T_{room}}{T_{melt} - T_{room}}\right)^m\right]}_{\text{Thermal softening term}} \tag{32}$$

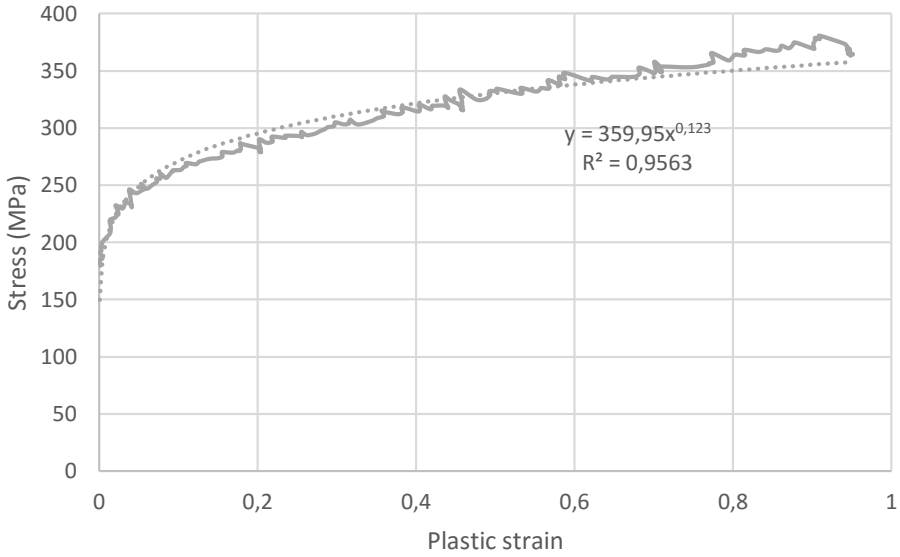

Figure 6.4 – Stress-plastic strain curve and its power trend line (flow stress curve) for the AlSi9Cu3 material

Table 6.2 – Obtained parameters for the first term of Johnson-Cook material flow model equation

	A[MPa]	**B[MPa]**	**C**	**n**	**m**
Compression test curve #1	178.64	359.95	-	0.123	-
Compression test curve #2	174.08	352.51	-	0.128	-
Compression test curve #3	179.86	356.05	-	0.119	-
Compression test curve #4	159.83	366.1	-	0.124	-
Average	**173.1**	**358.65**	**0.1**	**0.124**	**1.01**

Table 6.2 summarizes the parameters for the Johnson and Cook model. It is observed AlSi9Cu3 aluminium cast alloy has an initial flow stress that is about half of the flow stress of AlSi20 for the same strain-rate (quasi-static) and temperature (20ºC) conditions.

For the viscosity term of Johnson-Cook material model, C, an inverse analysis was conducted having the fully characterized AlSi20 aluminium alloy from DEFORM™ material library.

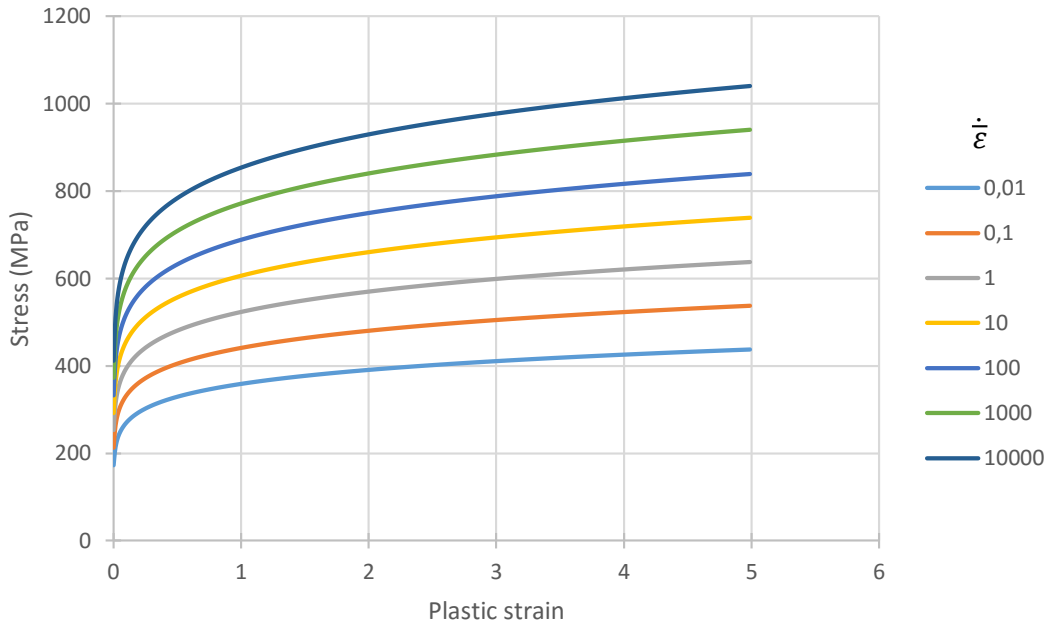

Figure 6.5 – Stress-plastic strain curves of aluminium alloy AlSi9Cu3 for different strain rates at a fixed temperature (20ºC) obtained from available data for AlSi20 alloy

For the thermal term a similar inverse analysis having AlSi20 as a reference resulted in different temperature softening for each specified strain-rate, leading to the m parameter shown in Table 6.2.

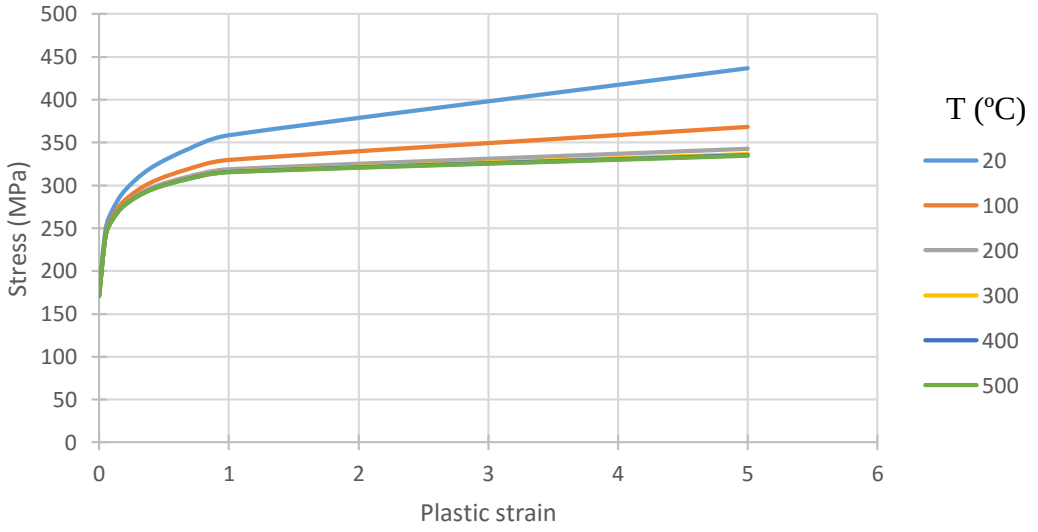

Figure 6.6 – Stress-plastic strain curves of aluminium alloy AlSi9Cu3 for different temperatures at a fixed strain rate (0.01) obtained from available data for AlSi20 alloy

Figure 6.5 and Figure 6.6 illustrate the used data for AlSi9Cu3 alloy simulation. Future tests are required in order to obtain more accurate data regarding this material.

6.2.3 Workpiece geometry

When it comes to workpiece geometry for 2D simulation, a default rectangle of XxY was defined, as represented in Figure 6.7.

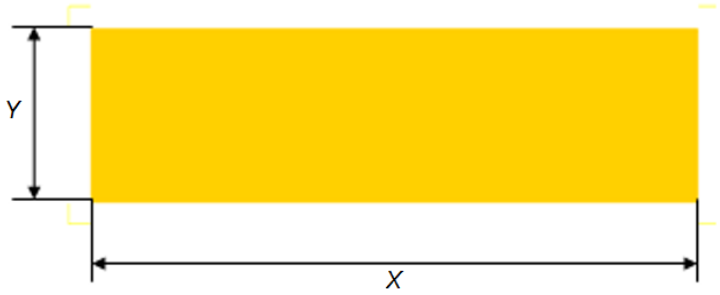

Figure 6.7 – Workpiece geometry for 2D simulation

For 3D turning simulation, according to the defined process parameters (feed rate, depth of cut and length of cut), workpiece geometry is automatically generated by the software. In Figure 6.8 the analysis domain is shown (blue). Analysis domain is notoriously small when compared to the complete turning operation. Due to the long computational time characteristic of machining simulation, only a small portion of the turning operation is simulated.

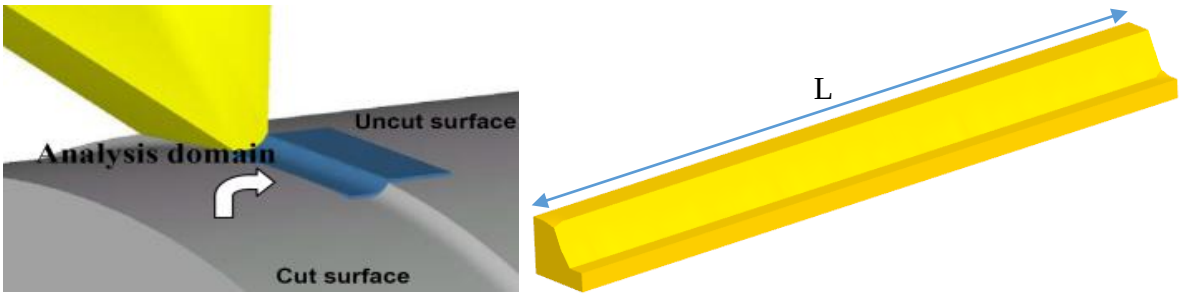

Figure 6.8 – Definition of workpiece geometry for 3D simulation

It is important to mention that due to the different performed simulations, the dimensions of the defined workpieces (X, Y in Figure 6.7 and L in Figure 6.8) will depend on cutting parameter combinations and will be summarized further, for each case.

6.2.4 Tool material and geometry

Polycrystalline diamond (PCD) tools were used in the machinability studies shown in Table 6.1. Being under extreme pressure and temperature conditions during use, materials for cutting tools require appropriate properties to resist plastic deformation, fracture, abrasion, chemical attack, wear mechanisms and maintain a sharp edge for a prolonged period of time. Hardness is the most basic requirement of a tool material, and in this regard, diamond is unequalled [77]. PCD inserts are composed of a WC-Co substrate with PCD plate brazed on the substrate, as schematically illustrated in Figure 6.9, the dimensions corresponding to the tool used in the present study.

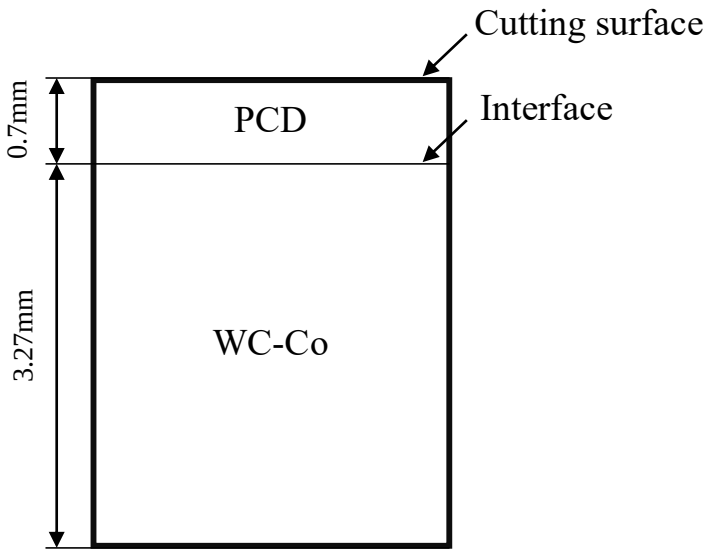

Figure 6.9 – Geometry of PCD layer and WC-Co substrate

Due to the geometry of PCD turning tools and since one of the goals of this dissertation is the exploratory work and sensitivity analysis of DEFORM™ 2D/3D machining software, two different approaches for tool material modelling were considered:

i) WC as tool material and PCD as tool coating;
ii) PCD as tool material.

For tool material approach i), WC was assigned to the tool material and, since the thickness of the PCD layer was of 0.7 mm [75] a coating of that same thickness was also assigned to the tool. On the second material approach, ii), PCD was assigned to the tool material.

Both tungsten carbide (WC) and polycrystalline diamond (PCD) are fully characterized on the software's material library. That mechanical and physical characterization is shown in Table 6.3.

Table 6.3 – Mechanical and physical properties of PCD and WC in DEFORM™ material library

Material	Density ($kg.m^{-3}$)	T. Conductivity ($W.m^{-1}.^oC^{-1}$)	Vol. heat capacity ($MJ.m^{-3}.^oC^{-1}$)	Thermal expansion coefficient ($10^{-6}K^{-1}$)	Elasticity M. (GPa)	Poisson ratio
PCD	3500	540	2.11	0	850	0.3
WC	15000	100	15	5.0	650	0.25

Given the cutting tool without chip breaker used in machinability studies led by Rui Soares [75] (see Figure 6.10) and according to the online catalogue of MAPAL [78] it was possible to build the 2D and 3D geometry of the tool resorting to CAD software.

Specification	Dimensions (mm)			
	d	s	r	d_1
DCGW 11T304 F01N-0AA	9.52	3.97	0.4	3.9

Figure 6.10 – Insert's geometry and dimensions

With a rake angle of 0º and a relief angle o 7º, tool geometry is shown in Figure 6.11 a) and b), for 2D and 3D simulations, respectively.

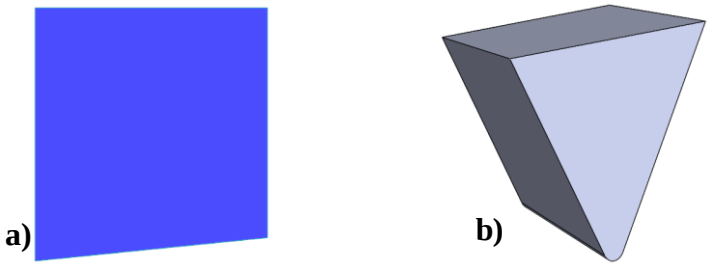

Figure 6.11 – Tool geometry used in turning simulation, 2D (a) and 3D (b)

In order to save computational time and since there is no need to depict the full geometry of the tool, the used geometry for 3D simulation included only part of the full insert.

6.3 Results

In order to capture a reasonable scope of the cutting parameters of Table 6.1, tests with maximum and minimum cutting speeds, as well as uncut chip thickness are selected which result in 4 different combinations of cutting parameters. The following sections of this dissertation focus on the simulation of those parameters with different material approaches.

6.3.1 AlSi20 as workpiece material

6.3.1.1 2D simulation with WC as tool material and PCD as coating material

Table 6.4 summarizes the used parameters for each of the four simulations with different cutting conditions combination. For those simulations, aluminium alloy AlSi20 was the selected workpiece material and the tool material was WC with a PCD coating (0.7 mm).

Table 6.4 – Summary of 2D turning simulations of AlSi20 with WC tool (PCD coated)

	2D simulation code:		**2D-a**	**2D-b**	**2D-c**	**2D-d**
Process	Cutting speed, v_c (m/min)		88	105	350	397
	Uncut chip thickness, t (mm)		0.25	0.05	0.25	0.05
	Cutting length, l (mm)		2.38	1.25	2.38	1.25
Tool	Mesh	Elements number	1051	1030	1051	1030
		Nodes number	1112	1089	1112	1089
Workpiece	Mesh	Elements number	1703	1703	2851	2851
		Nodes number	1891	1891	3005	3005
	Dimensions (XxY)		7.5x1.75	1.5x0.35	7.5x1.75	1.5x0.35
Contact	Friction (shear model)	Tool-Workpiece	0.6			
		Workpiece-Workpiece				
	Heat transfer coefficient (N/s/mm/ºC)	Tool-Workpiece	45			
		Workpiece-Workpiece				
	Separation Criterion		Default			
Numerical	Simulation type		Lagrangian Incremental			
	Iteration method		Direct			
	Solver		Skyline			

Figure 6.12 illustrates cutting force curve resultant from each FEM simulation (blue), comparing it to the experimentally obtained cutting forces curves (orange) for the same cutting conditions. It is important to mention that each graph contains 2 horizontal axes due to the magnitude difference of time between experimental tests and simulations.

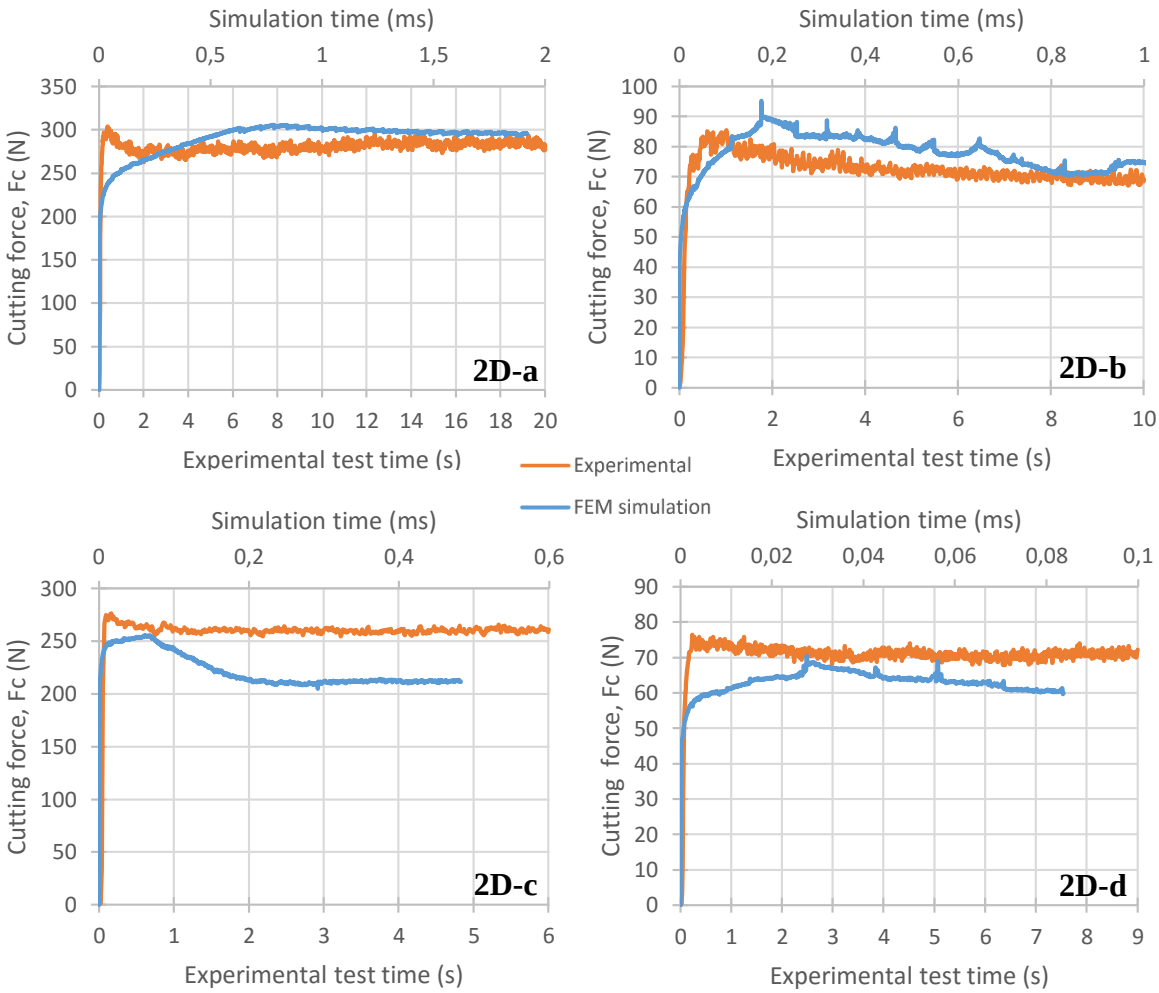

Figure 6.12 - Cutting forces curves for AlSi20 turning simulation (2D) with WC as tool material and PCD coating

In order to compare the two curves, Table 6.5 shows for both FEM simulation and experimental approaches, the average cutting forces for the same cutting conditions. It is important to note that average results were taken from a stabilized excerpt of the curves, in order to ignore cutting forces resultant from initial transient chip formation.

Table 6.5 – Cutting forces average results (N) for AlSi20 turning simulation (2D) with WC tool and PCD coating

	2D-a	**2D-b**	**2D-c**	**2D-d**
Experimental	281.6	77.7	260.1	72.6
FEM simulation	299.1	79.1	211.5	63.7
Relative error	6.21%	1.80%	-18.7%	-1.60%

6.3.1.2 2D simulation with PCD as tool material

Table 6.6 summarizes the used parameters for each of the four two-dimensional simulations with different cutting conditions combination. For those simulations, aluminium alloy AlSi20 was the selected workpiece material and PCD was assigned to the tool material.

Table 6.6 - Summary of 2D turning simulations of AlSi20 with full PCD tool

	2D simulation code:		**2D-e**	**2D-f**	**2D-g**	**2D-h**
Process	Cutting speed, v_c (m/min)		88	105	350	397
	Uncut chip thickness, t (mm)		0.25	0.05	0.25	0.05
	Cutting length, l (mm)		2.38	1.25	2.38	1.25
Tool	Mesh	Elements number	1051	1030	1051	1030
		Nodes number	1112	1089	1112	1089
Workpiece	Mesh	Elements number	1992	2454	1992	2454
		Nodes number	2103	2643	2103	2643
	Dimensions (XxY)		7.5x1.75	1.5x0.35	7.5x1.75	1.5x0.35
Contact	Friction (shear model)	Tool-Workpiece	0.6			
		Workpiece-Workpiece				
	Heat transfer coefficient (N/s/mm/ºC)	Tool-Workpiece	45			
		Workpiece-Workpiece				
	Separation Criterion		Default			
Numerical	Simulation type		Lagrangian Incremental			
	Iteration method		Direct			
	Solver		Skyline			

Figure 6.13 illustrates cutting force curves resultant from each FEM simulation (blue), comparing it to the experimentally obtained cutting forces curves (orange) for the same cutting conditions for 2D simulation with PCD as tool material and AlSi20 as workpiece material.

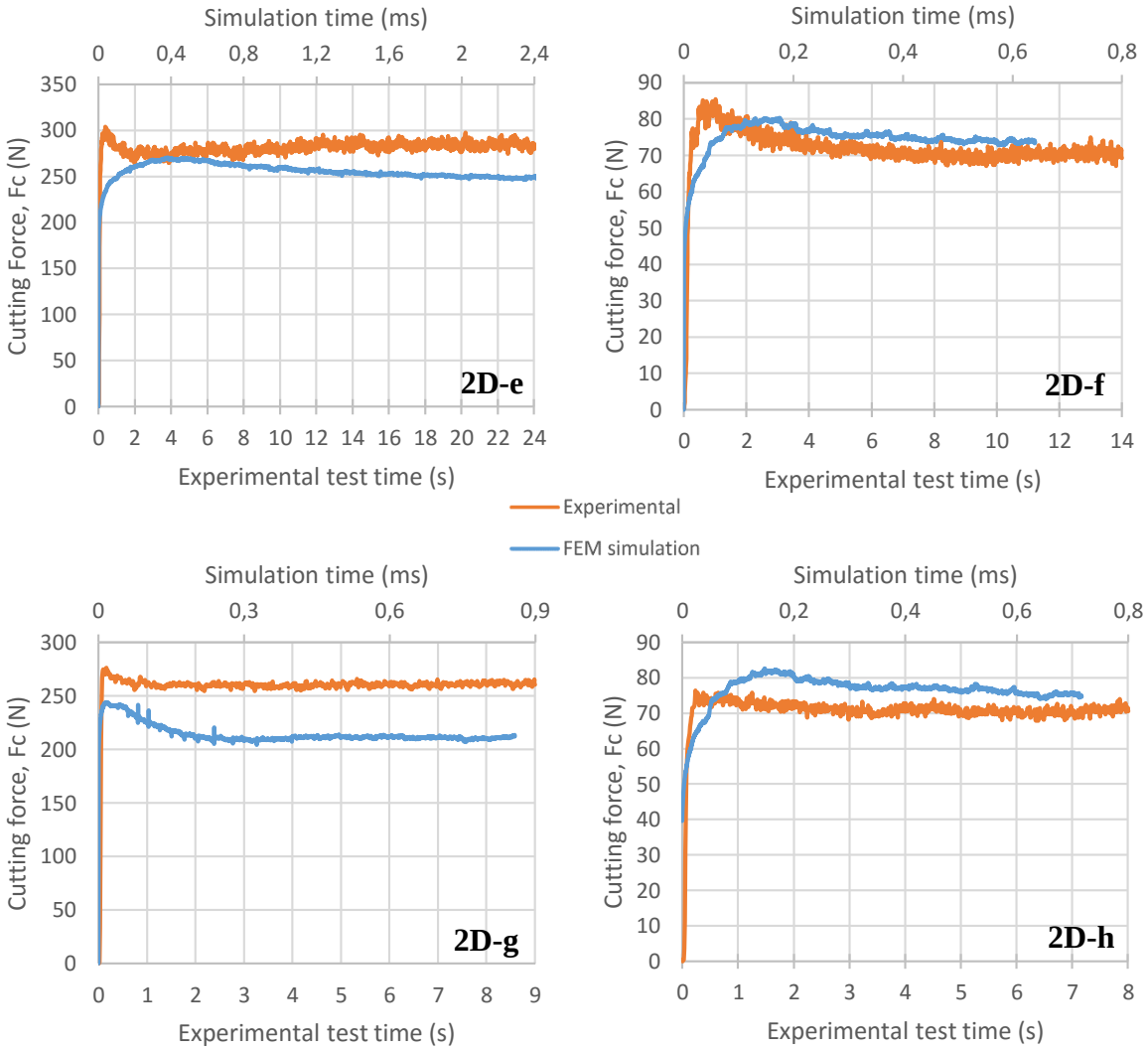

Figure 6.13 - Cutting forces curves for AlSi20 turning simulation (2D) with PCD as tool material

In order to compare the two curves, Table 6.7 shows for both FEM simulation and experimental approaches, the average cutting forces for the same cutting conditions.

Table 6.7 – Cutting forces average results (N) for AlSi20 turning simulation (2D) with PCD tool

	2D-a	2D-b	2D-c	2D-d
Experimental	281.6	77.7	260.1	72.6
FEM simulation	253.8	75.3	214.6	77.0
Relative error	-9.87%	3.09%	-17.5%	6.06%

6.3.1.3 3D simulation with WC as tool material and PCD as coating material

Similarly to the two-dimensional approach, two different ranges of feed rate (0.25 and 0.05 mm) and depth of cut (1.5 and 0.25 mm) were tested for four different values of speed. The four parameter combinations are presented in Table 6.8. In this section, aluminium alloy AlSi20 was defined as workpiece material. Tool material was WC with PCD coating of 0.7 mm.

Table 6.8 – Summary of 3D turning simulation of AlSi20 with WC tool (PCD coated)

3D simulation code:			**3D-a**	**3D-b**	**3D-c**	**3D-d**
Process	Cutting speed, v_c (m/min)		88	117	350	432
	Feed rate, f (mm/rev)		0.25	0.05	0.25	0.05
	Depth of cut, w (mm)		1.5	0.25	1.5	0.25
	Cutting length, l (mm)		15			
Tool	Mesh	Elements number	45168			
		Nodes number	9158			
		Minimum element size (mm)	0.05	0.05	0.05	0.05
Workpiece	Mesh	Elements number	10788	15721	10788	15721
		Nodes number	2697	4379	2697	4379
		Minimum element size (mm)	0.025	0.0075	0.025	0.0075
	Length, L (mm)		30			
Contact	Friction (hybrid model)	Tool-Workpiece	0.6 (Coulomb) 0.7 (Shear)			
		Workpiece-Workpiece				
	Heat transfer coefficient (N/s/mm/ºC)	Tool-Workpiece	40			
		Workpiece-Workpiece				
	Separation Criterion		Default			
Numerical	Simulation type		Lagrangian Incremental			
	Iteration method		Direct			
	Solver		Skyline			

Figure 6.14 illustrates cutting force curve resultant from each FEM simulation (blue), comparing it to the experimentally obtained cutting forces curves (orange) for the same cutting conditions for 3D simulation with WC tool material, PCD as coating material and AlSi20 as workpiece material for 3D simulation with WC as tool material, PCD as coating material and AlSi9Cu3 as workpiece material.

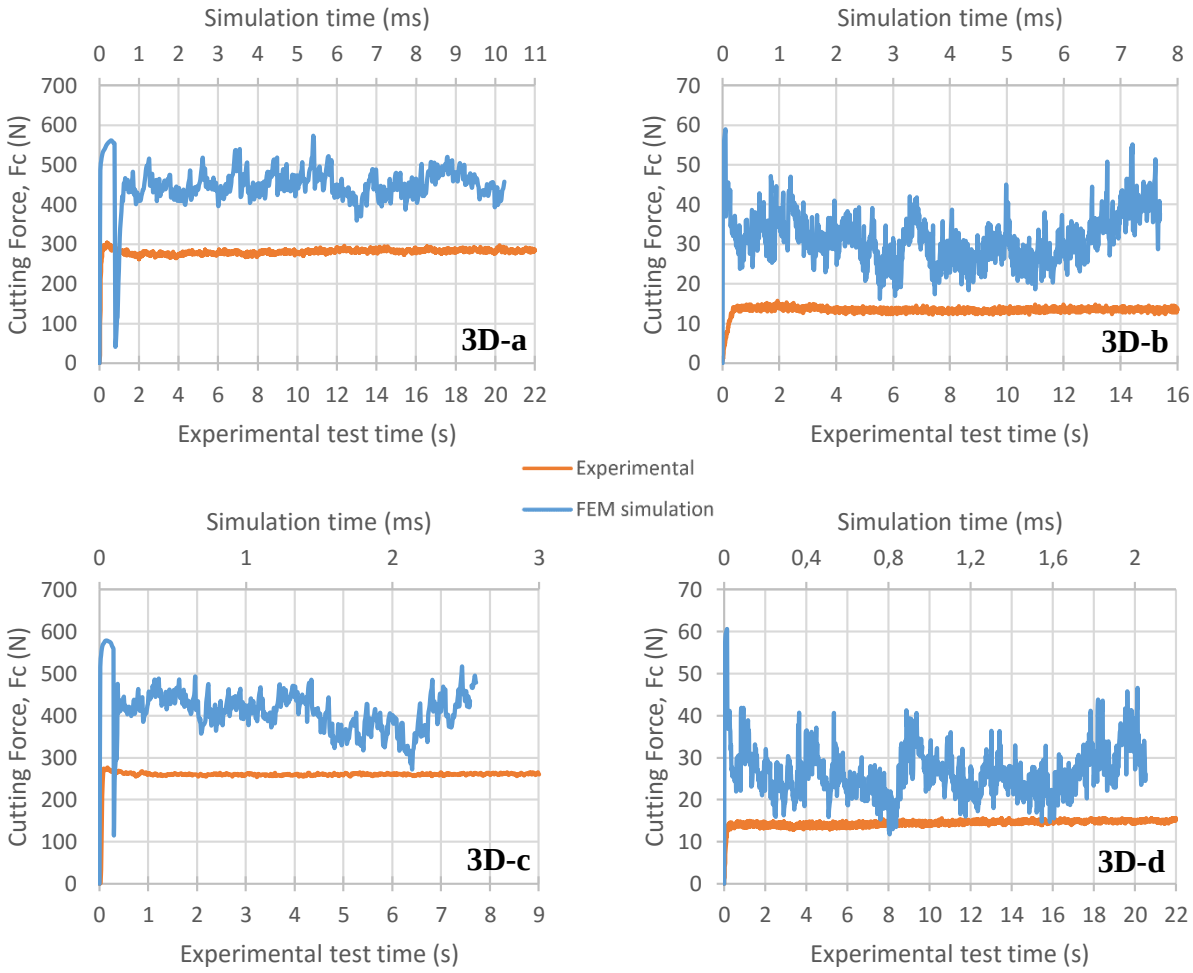

Figure 6.14 - Cutting forces curves for AlSi20 turning simulation (3D) with WC as tool material and PCD coating

In order to compare the two curves, Table 6.9 shows for both FEM simulation and experimental approaches, the average cutting forces for the same cutting conditions as well as the relative error between them.

Table 6.9 - Cutting forces average results (N) for AlSi20 turning simulation (3D) with WC tool and PCD coating

	3D-a	**3D-b**	**3D-c**	**3D-d**
Experimental	281.6	14.5	260.1	14.9
FEM simulation	452.4	29.8	404.7	24.9
Relative error	60.7%	105.5%	55.6%	67.1%

Figure 6.15 shows for each of the simulation from Table 6.8 chip geometry and temperature field distribution, indicating maximum reached temperature.

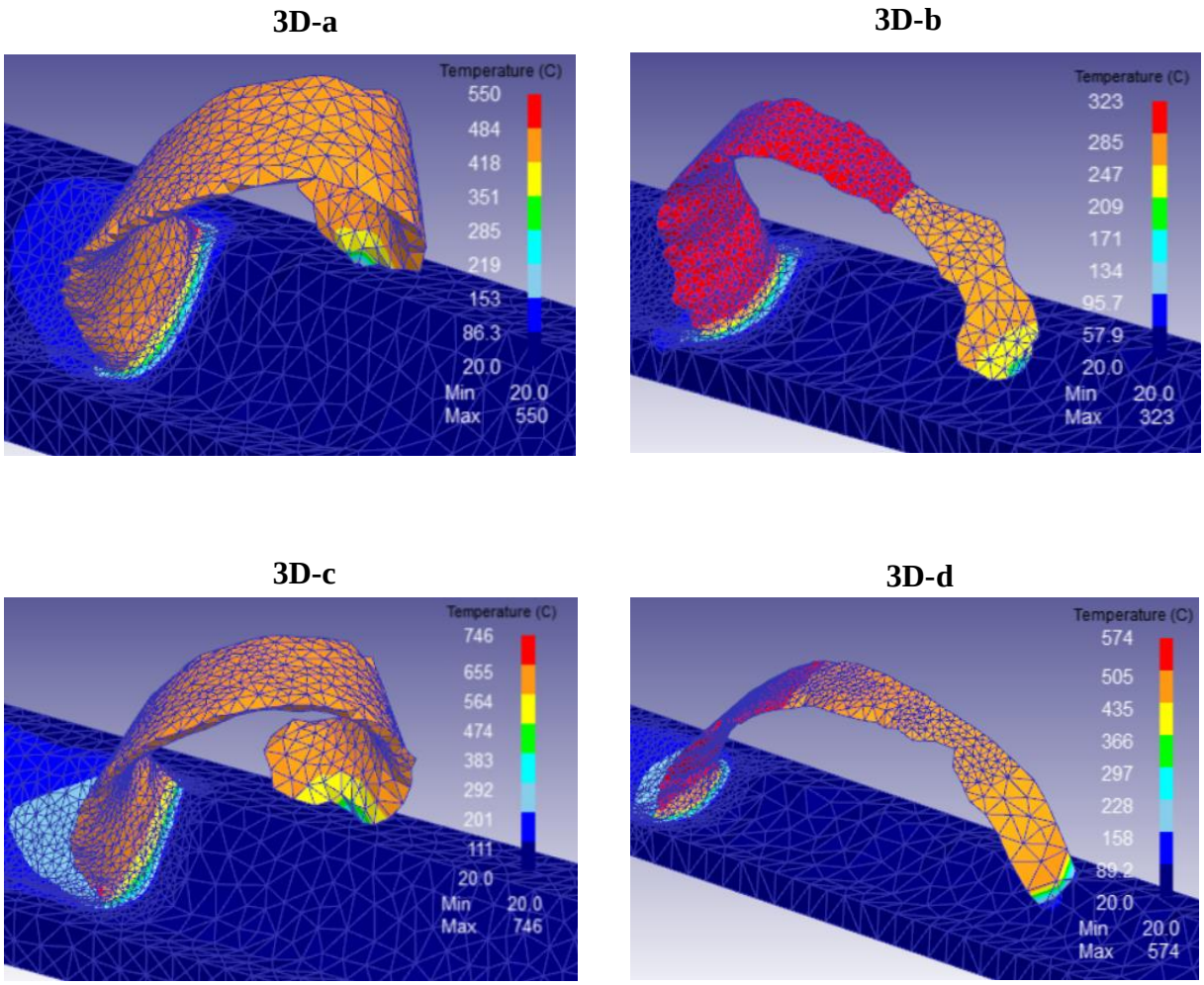

Figure 6.15 – Chip geometry and temperature field distribution for each simulation of AlSi20 3D turning with WC tool and PCD coating

6.3.1.4 3D simulation with PCD as tool material

Table 6.10 summarizes the used parameters for each of the four three-dimensional simulations with different cutting conditions combination. For those simulations, aluminium alloy AlSi20 was the selected workpiece material and PCD was assigned to the tool material.

Table 6.10 – Summary of 3D turning simulation of AlSi20 with full PCD tool

3D simulation code:			**3D-e**	**3D-f**	**3D-g**	**3D-h**
Process	Cutting speed, v_c (m/min)		88	117	350	432
	Feed rate, f (mm/rev)		0.25	0.05	0.25	0.05
	Depth of cut, w (mm)		1.5	0.25	1.5	0.25
	Cutting length, l (mm)		15	5	15	5
Tool	Mesh	Elements number	41474	27570	41474	27739
		Nodes number	9236	6223	9236	6250
		Minimum element size (mm)	0.05			
Workpiece	Mesh	Elements number	4792	15721	4816	15959
		Nodes number	1256	4379	1273	4419
		Minimum element size (mm)	0.0375	0.0075	0.035	0.0075
	Length, L (mm)		30			
Contact	Friction (hybrid model)	Tool-Workpiece	0.6 (Coulomb) 0.7 (Shear)			
		Workpiece-Workpiece				
	Heat transfer coefficient (N/s/mm/ºC)	Tool-Workpiece	40			
		Workpiece-Workpiece				
	Separation Criterion		Default			
Numerical	Simulation type		Lagrangian Incremental			
	Iteration method		Direct			
	Solver		Skyline			

Figure 6.16 illustrates cutting force curve resultant from each FEM simulation (blue), comparing it to the experimentally obtained cutting forces curves (orange) for the same cutting conditions for 3D simulation with PCD as tool material and AlSi20 as workpiece material.

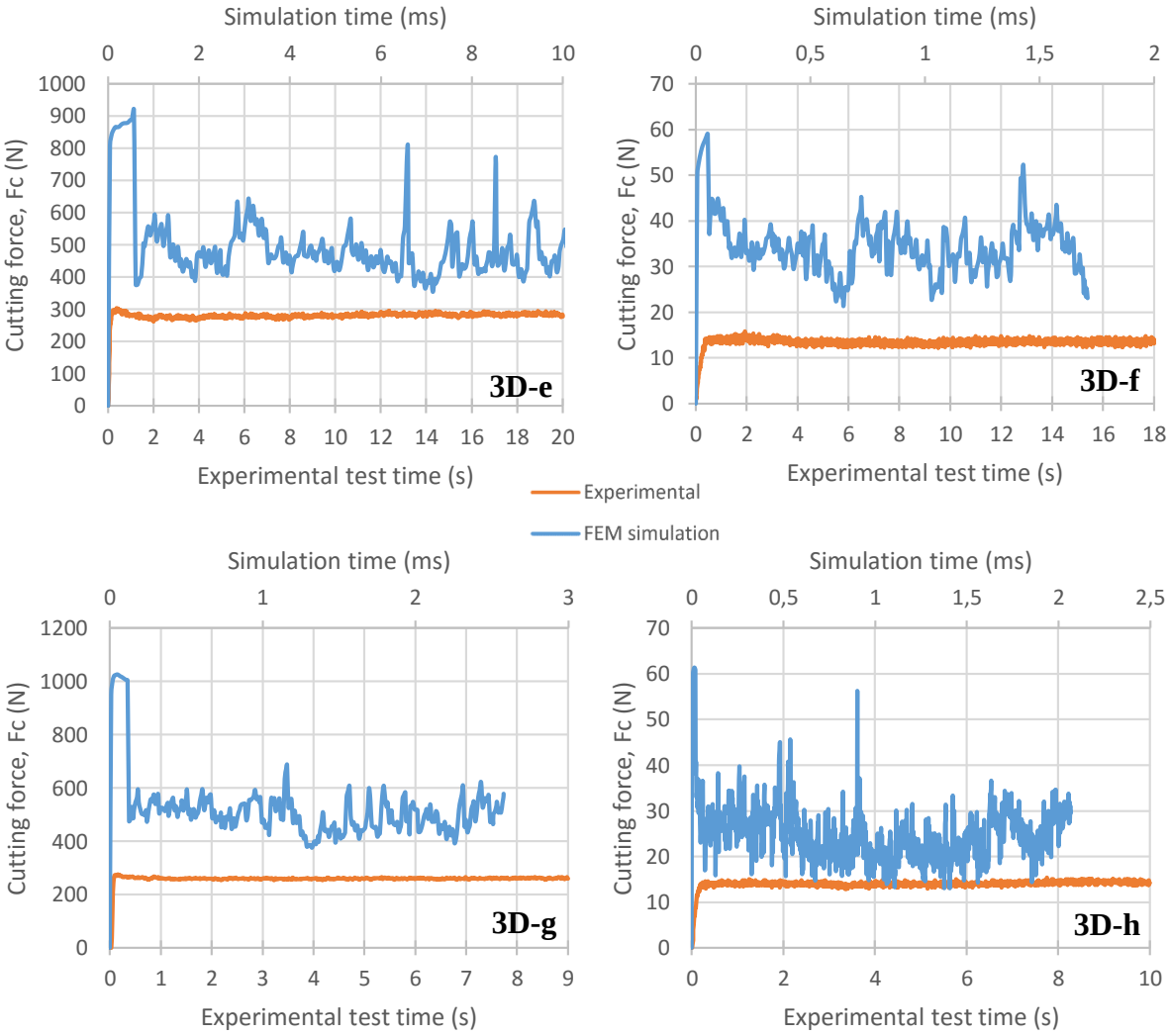

Figure 6.16 – Cutting forces curves for AlSi20 turning simulation (3D) with PCD as tool material

Table 6.11 shows the cutting force averages values for both experimental machining tests and the performed simulations as well as the relative error between the two.

Table 6.11 – Cutting forces average (N) results for AlSi20 turning simulation (3D) with PCD tool

	3D-e	3D-f	3D-g	3D-h
Experimental	281.6	14.5	260.1	14.9
FEM simulation	477.2	33.4	498.5	24.5
Relative error	69.4%	130.3%	91.7%	64.4%

Figure 6.17 shows for each of the simulation from Table 6.10 chip geometry and temperature field distribution, indicating maximum reached temperature.

3D-e

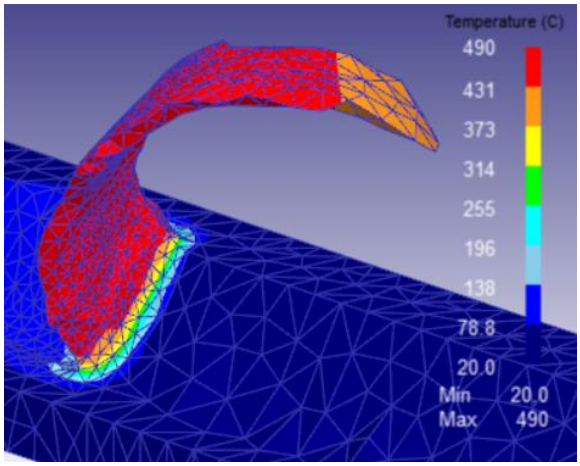

3D-f

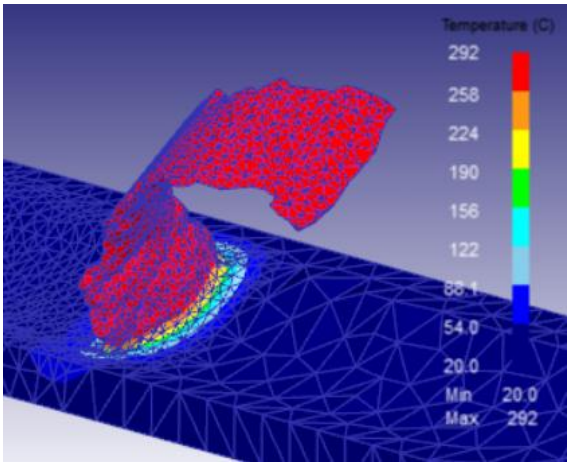

3D-g

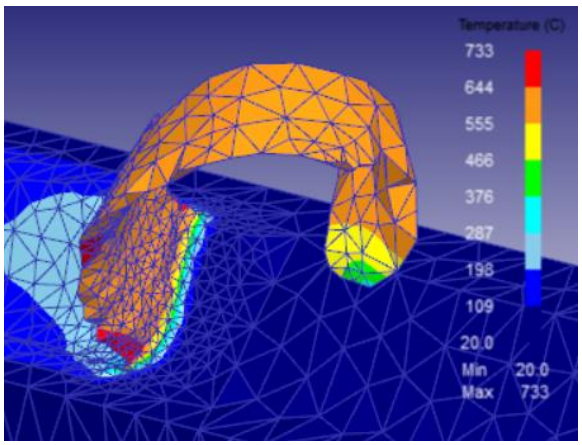

3D-h

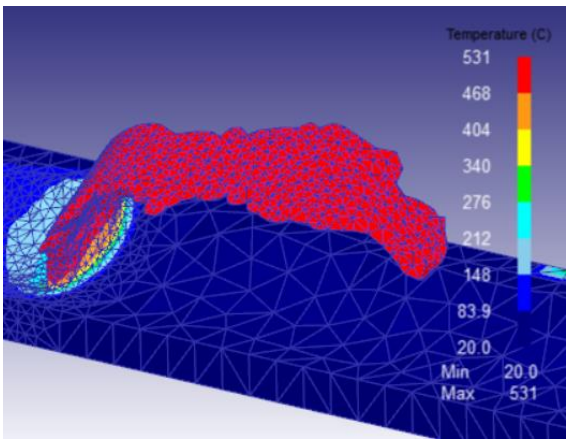

Figure 6.17 – Chip geometry and temperature field distribution for each simulation of AlS20i 3D turning with full PCD tool

6.3.2 AlSi9Cu3 as workpiece material

Similarly to the previous section, 4 different combinations of cutting parameters are selected which result in 4 different simulations that capture a scope of 2 different magnitudes of cutting speed and uncut chip thickness. The selected combinations of these two parameters are the same as the simulated for AlSi20 aluminium alloy in the previous section.

6.3.2.1 2D simulation with WC-Co as workpiece material and PCD as coating material

Table 6.12 summarizes the used parameters for each of the four simulations with different cutting conditions combination. For those simulations, aluminium alloy AlSi9Cu3 was the selected workpiece material and the tool material was WC with a PCD coating (0.7 mm).

Table 6.12 – Summary of 2D turning simulations of AlSi9Cu3 with WC tool (PCD coated)

	2D simulation code:		**2D-a**	**2D-b**	**2D-c**	**2D-d**
Process	Cutting speed, v_c (m/min)		88	105	350	397
	Uncut chip thickness, t (mm)		0.25	0.05	0.25	0.05
	Cutting length, l (mm)		3.75	0.75	3.75	0.75
Tool	Mesh	Elements number	1051	1030	1051	1030
		Nodes number	1112	1089	1112	1089
Workpiece	Mesh	Elements number	1669	1669	2909	2869
		Nodes number	1761	1761	3020	2982
	Dimensions (XxY)		7.5x1.75	1.5x0.35	7.5x1.75	1.5x0.35
Contact	Friction (shear model)	Tool-Workpiece	0.6			
		Workpiece-Workpiece				
	Heat transfer coefficient (N/s/mm/ºC)	Tool-Workpiece	45			
		Workpiece-Workpiece				
	Separation Criterion		Default			
Numerical	Simulation type		Lagrangian Incremental			
	Iteration method		Direct			
	Solver		Skyline			

Figure 6.18 illustrates cutting force curve resultant from each FEM simulation (blue), comparing it to the experimentally obtained cutting forces curves (orange) for the same cutting conditions for 2D simulation with WC as tool material, PCD as coating material and AlSi9Cu3 as workpiece material.

Simulations 2D-c and 2D-d, with higher cutting speed (350 and 397 m/min, respectively), did not converged.

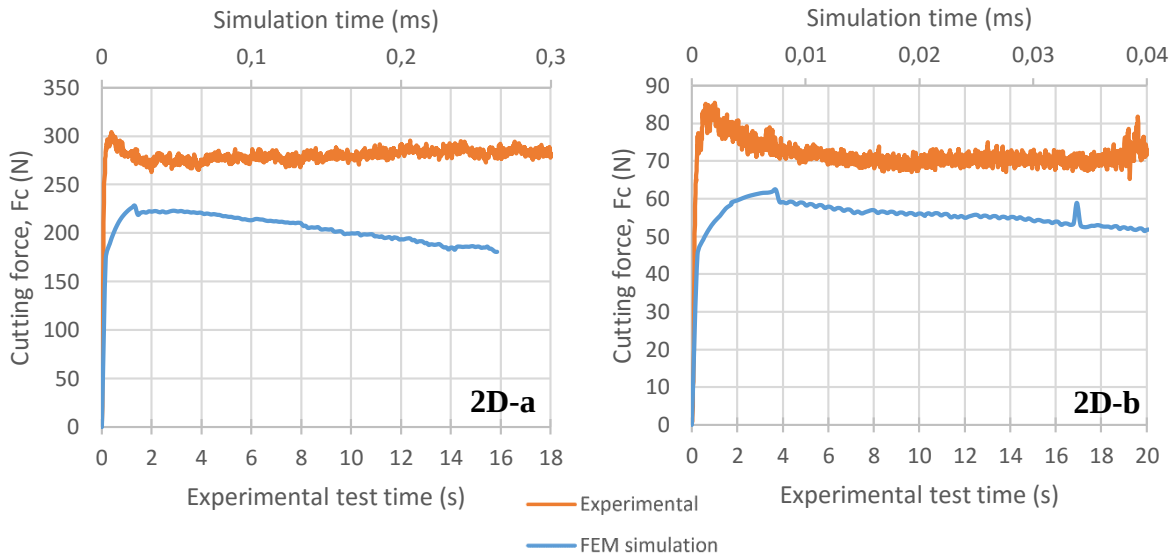

Figure 6.18 – Cutting forces curves for AlSi9Cu3 turning simulation (2D) with WC as tool material and PCD coating

In order to compare the two curves, Table 6.13 shows for both FEM simulation and experimental approaches, the average cutting forces for each set of cutting parameters.

Table 6.13 – Cutting forces average results (N) for AlSi9Cu3 turning simulation (2D) with WC tool (PCD coated)

	2D-a	**2D-b**	**2D-c**	**2D-d**
Experimental	281.6	77.7	260.1	72.6
FEM simulation	203.8	54.9	-	-
Relative error	-27.6%	-29.3%	-	-

6.3.2.2 2D simulation with PCD as tool material

Table 6.14 summarizes the used parameters for each of the four two-dimensional simulations with different cutting conditions combination. For those simulations, aluminium alloy AlSi9Cu3 was the selected workpiece material and PCD was assigned to the tool material.

Table 6.14 – Summary of 2D turning simulations of AlSi9Cu3 with PCD tool

	2D simulation code:		**2D-e**	**2D-f**	**2D-g**	**2D-h**
Process	Cutting speed, v_c (m/min)		88	105	350	397
	Uncut chip thickness, t (mm)		0.25	0.05	0.25	0.05
	Cutting length, l (mm)		3.75	0.75	3.75	0.75
Tool	Mesh	Elements number	1051	1030	1051	1030
		Nodes number	1112	1089	1112	1089
Workpiece	Mesh	Elements number	1992	1994	2785	3431
		Nodes number	2103	2105	2896	3547
	Dimensions (XxY)		7.5x1.75	1.5x0.35	7.5x1.75	1.5x0.35
Contact	Friction (shear model)	Tool-Workpiece	0.6			
		Workpiece-Workpiece				
	Heat transfer coefficient (N/s/mm/ºC)	Tool-Workpiece	45			
		Workpiece-Workpiece				
	Separation Criterion		Default			
Numerical	Simulation type		Lagrangian Incremental			
	Iteration method		Direct			
	Solver		Skyline			

Figure 6.19 illustrates cutting force curve resultant from each FEM simulation (blue), comparing it to the experimentally obtained cutting forces curves (orange) for the same cutting conditions for 2D simulation with PCD as tool material and AlSi9Cu3 as workpiece material.

Simulations 2D-g and 2D-h, with higher cutting speed (350 and 397 m/min, respectively), did not converged.

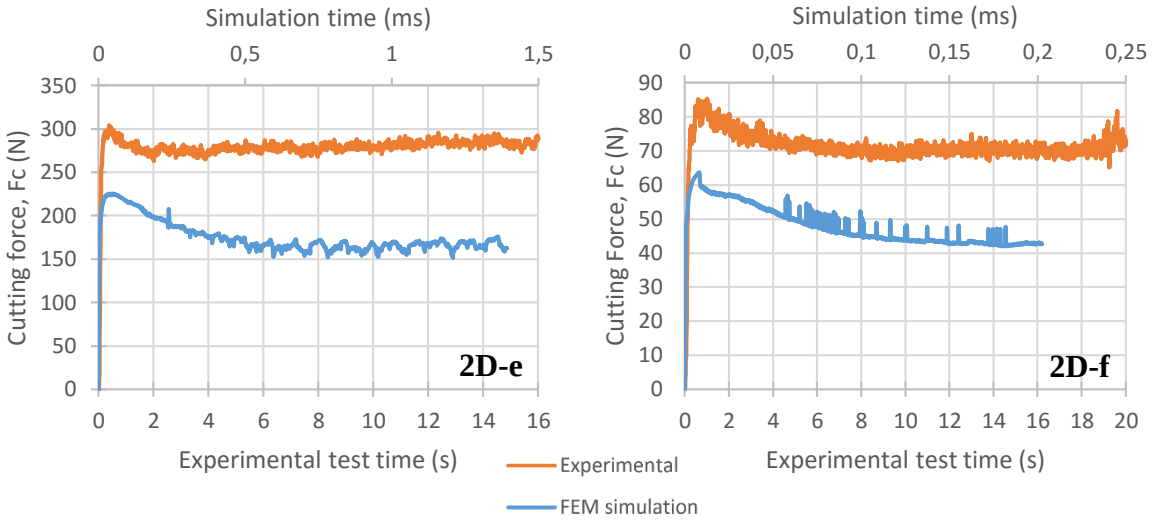

Figure 6.19 – Cutting forces curves for AlSi9Cu3 turning simulation (2D) with PCD as tool material

In order to compare the two curves, Table 6.15 shows for both FEM simulation and experimental approaches, the average cutting forces for each set of cutting parameters.

Table 6.15 – Cutting forces average results (N) for AlSi9Cu3 turning simulation (2D) with PCD tool

	2D-a	**2D-b**	**2D-c**	**2D-d**
Experimental	281.6	77.7	260.1	72.6
FEM simulation	167.2	45.4	-	-
Relative error	-40.6%	-41.6%	-	-

6.3.2.3 3D simulation with WC as tool material and PCD as coating material

In this section, two different ranges of feed rate (0.25 and 0.05 mm) and depth of cut (1.5 and 0.25 mm) were tested for four different values of speed. Aluminium alloy AlSi9Cu3 was defined as workpiece material. Tool material was WC with PCD coating of 0.7 mm.

Table 6.16 – Summary of 3D turning simulation of AlSi9Cu3 with WC tool (PCD coated)

3D simulation code:			**3D-a**	**3D-b**	**3D-c**	**3D-d**
Process	Cutting speed, v_c (m/min)		88	117	350	432
	Feed rate, f (mm/rev)		0.25	0.05	0.25	0.05
	Depth of cut, w (mm)		1.5	0.25	1.5	0.25
	Cutting length, l (mm)		15	15	15	15
Tool	Mesh	Elements number	45168			
		Nodes number	9158			
		Minimum element size (mm)	0.05			
Workpiece	Mesh	Elements number	6326	9086	6254	15721
		Nodes number	1646	2622	1635	4379
		Minimum element size (mm)	0.0325	0.0075	0.0325	0.0075
	Dimensions (L) (mm)		30	20	30	30
Contact	Friction (hybrid model)	Tool-Workpiece	0.6 (Coulomb) 0.7 (Shear)			
		Workpiece-Workpiece				
	Heat transfer coefficient (N/s/mm/ºC)	Tool-Workpiece	40			
		Workpiece-Workpiece				
	Separation Criterion		Default			
Numerical	Simulation type		Lagrangian Incremental			
	Iteration method		Direct			
	Solver		Skyline			

Figure 6.20 illustrates cutting force curve resultant from each FEM simulation (blue), comparing it to the experimentally obtained cutting forces curves (orange) for the same cutting conditions for 3D simulation with WC as tool material, PCD as coating material and AlSi9Cu3 as workpiece material.

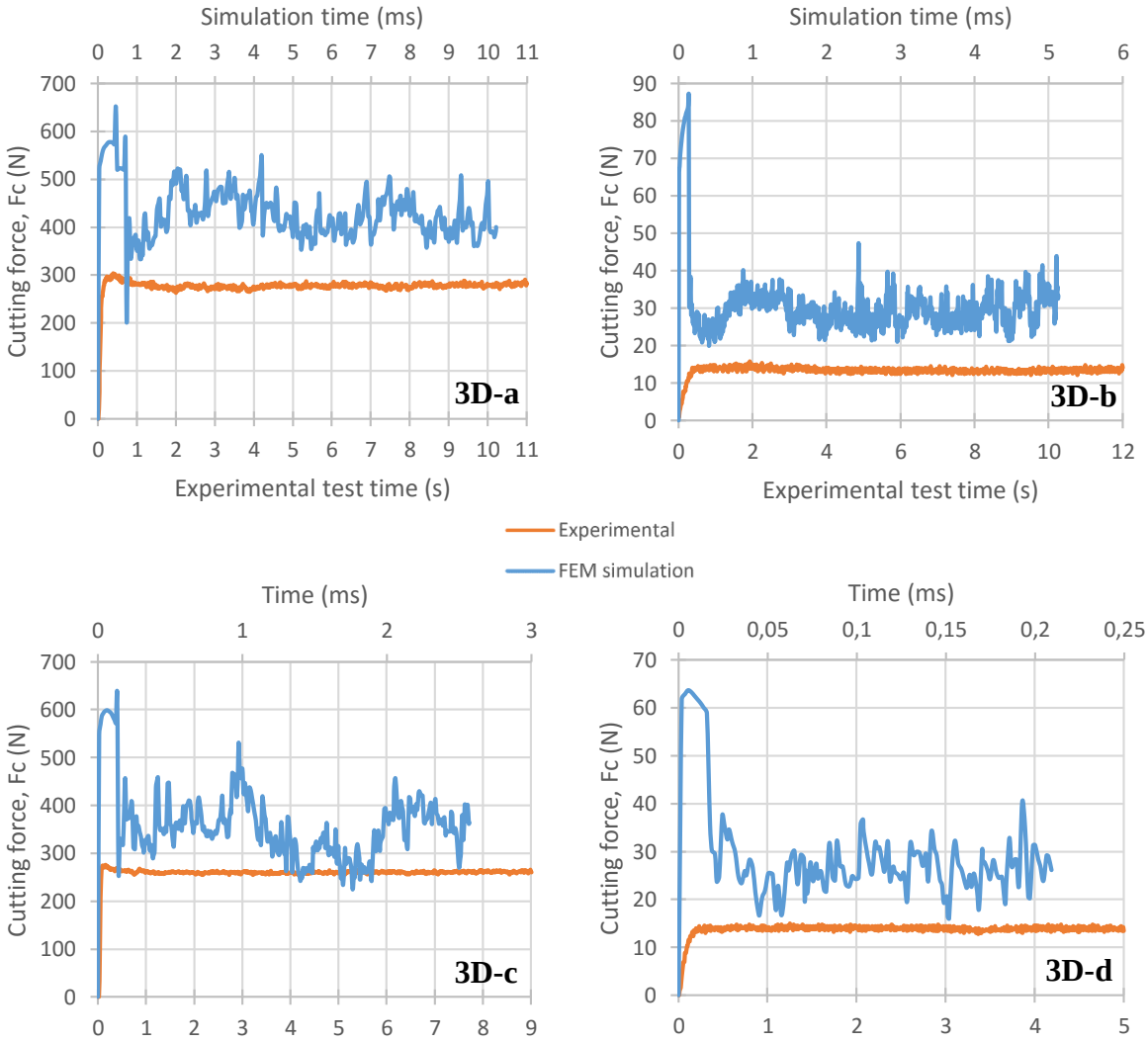

Figure 6.20 - Cutting forces curves for 3D AlSi9Cu3 turning simulation with WC tool and PCD coating

In order to compare the two curves, Table 6.17 shows for both FEM simulation and experimental approaches, the average cutting forces for the same cutting conditions as well as the relative error between them.

Table 6.17 – Cutting forces average results (N) for AlSi9Cu3 turning simulation (3D) with WC tool (PCD coated)

	3D-a	**3D-b**	**3D-c**	**3D-d**
Experimental	281.6	14.5	260.1	14.9
FEM simulation	423.7	29.3	345.4	26.2
Relative error	50.5%	102.1%	32.8%	75.8%

Figure 6.21 shows for each of the simulation from Table 6.16 chip geometry and temperature field distribution, indicating maximum reached temperatures.

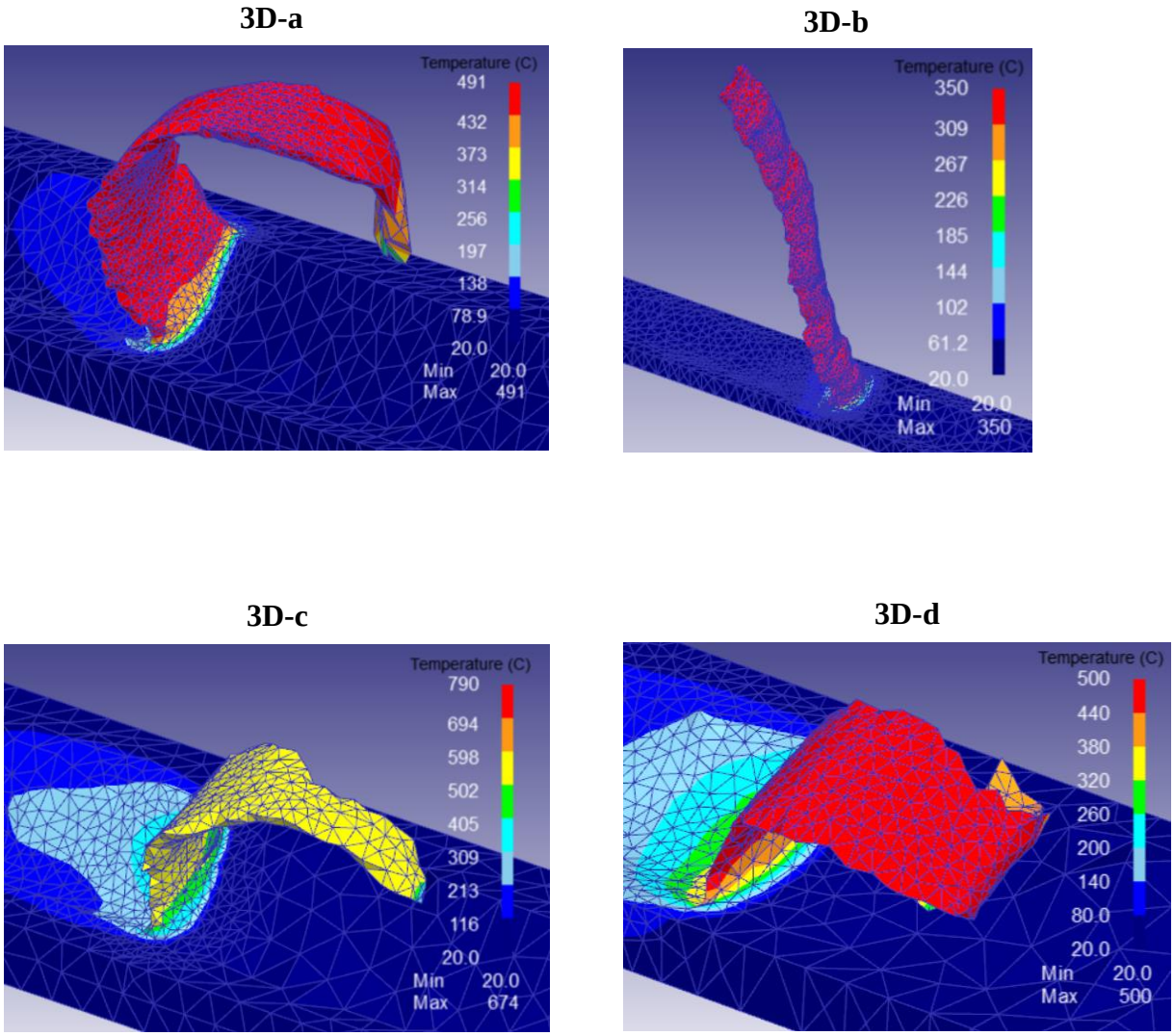

Figure 6.21 – Chip geometry and temperature field distribution for each simulation of AlSi9Cu3 3D turning with WC tool and PCD coating

6.3.2.4 3D simulation with PCD as tool material

Table 6.18 summarizes the used parameters for each of the four three-dimensional simulations with different cutting conditions combination. For those simulations, aluminium alloy AlSi9Cu3 was the selected workpiece material and PCD was assigned to the tool material.

Table 6.18 – Summary of 3D turning simulation of AlSi9Cu3 with full PCD tool

3D simulation code:			**3D-a**	**3D-b**	**3D-c**	**3D-d**
Process	Cutting speed, v_c (m/min)		88	117	350	432
	Feed rate, f (mm/rev)		0.25	0.05	0.25	0.05
	Depth of cut, w (mm)		1.5	0.25	1.5	0.25
	Cutting length, l (mm)		15	15	15	15
Tool	Mesh	Element number	27570			
		Node number	6223			
		Minimum element size (mm)	0.05			
Workpiece	Mesh	Element number	4782	15721	4782	15721
		Node number	1262	4379	1262	4379
		Minimum element size (mm)	0.0375	0.0075	0.0375	0.0075
	Dimensions (L) (mm)		30			
Contact	Friction (hybrid model)	Tool-Workpiece	0.6 (Coulomb) 0.7 (Shear)			
		Workpiece-Workpiece				
	Heat transfer coefficient (N/s/mm/ºC)	Tool-Workpiece	40			
		Workpiece-Workpiece				
	Separation Criterion		Default			
Numerical	Simulation type		Lagrangian Incremental			
	Iteration method		Direct			
	Solver		Skyline			

Figure 6.22 illustrates cutting force curve resultant from each FEM simulation (blue), comparing it to the experimentally obtained cutting forces curves (orange) for the same cutting conditions for 3D simulation with PCD as tool material and AlSi9Cu3 as workpiece material.

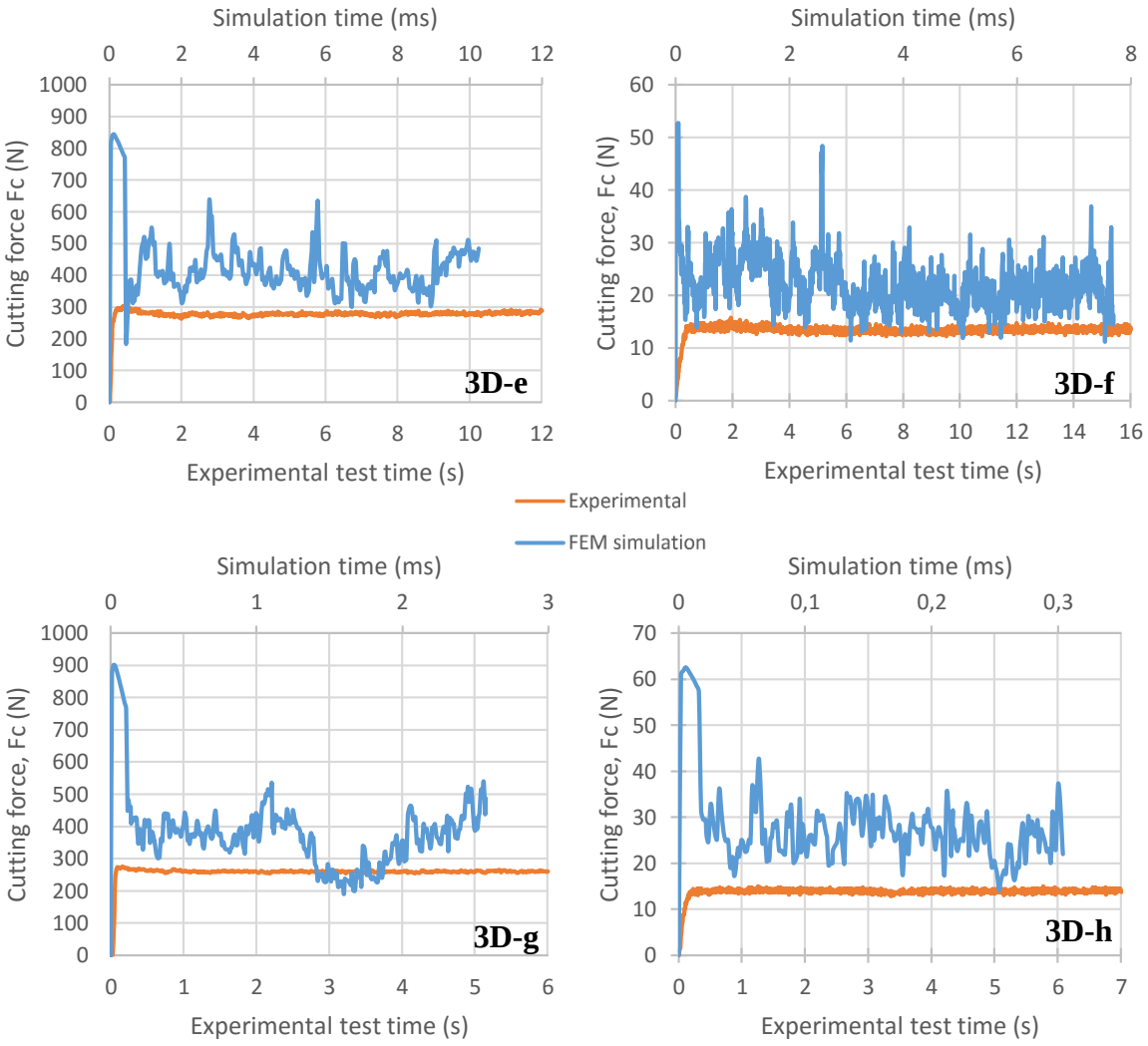

Figure 6.22 - Cutting forces curves for 3D AlSi9Cu3 turning simulation with PCD tool

Table 6.19 shows the cutting force averages values for both experimental machining tests and the performed simulations as well as the relative error between the two.

Table 6.19 – Cutting forces average results (N) for AlSi20 turning simulation (3D) with PCD tool

	3D-e	**3D-f**	**3D-g**	**3D-h**
Experimental	281.6	14.5	260.1	14.9
FEM simulation	412.0	22.0	360.3	26.0
Relative error	46.3%	51.7%	38.5%	74.5%

Figure 6.23 shows for each of the simulation from Table 6.18 chip geometry and temperature field distribution, indicating maximum reached temperature.

3D-e

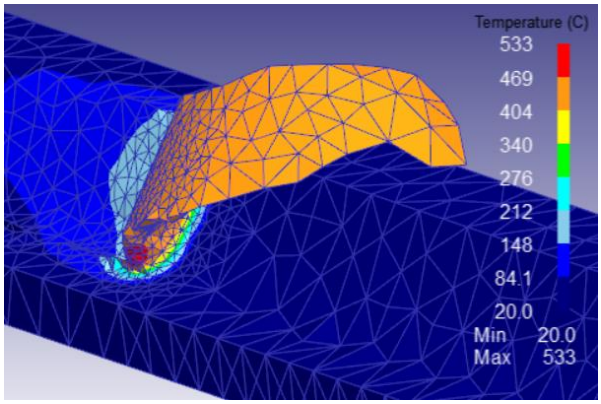

3D-f

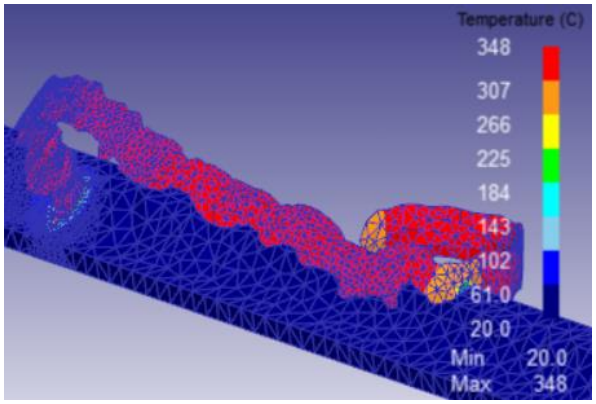

3D-g

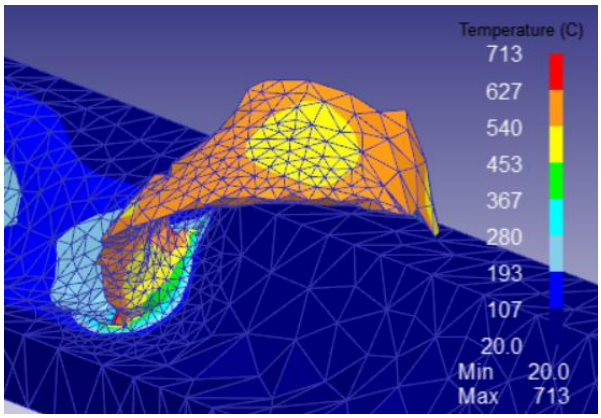

3D-h

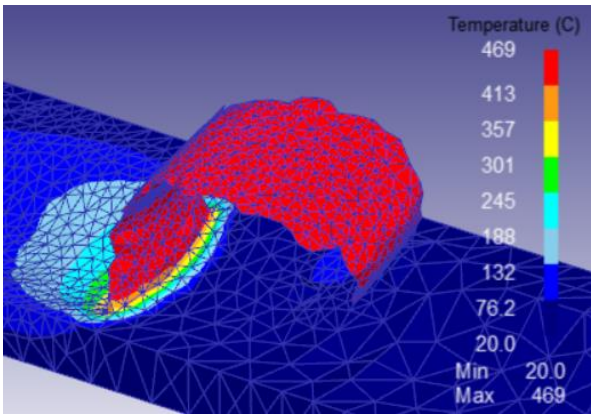

Figure 6.23 – Chip geometry and temperature field distribution for each simulation of AlSi9Cu3 3D turning with full PCD tool

6.3.3 Discussion

Including the aluminium alloy AlSi20 in this simulation study allowed establishing a reference level for the obtained cutting forces. Due to higher resistance of this material when compared to the aluminium alloy AlSi9Cu3, it was expected that cutting forces would be also higher, which was observed.

For the two-dimensional turning simulation, DEFORM™ software does not have a depth of cut input, plane strain conditions being assumed (high values of depth of cut, that is in the viewing plane direction). In order to obtain reasonable correlations between the experimental and simulated values, all the two-dimensional simulations were run for the maximum depth of cut experimented by Rui Soares in [75], which is 1.5 mm. It was found that for the simulations which workpiece material was AlSi20, simulated values of cutting forces presented a better correlation with the experimental than for the simulations with AlSi9Cu3 as workpiece material. This may indicate, among others, that AlSi9Cu3 material was not accurately characterized. Table 6.20 shows the average relative error for both workpiece materials and for the 2D and 3D cases.

Table 6.20 – Average relative error between experimental and simulated values for each workpiece material

	Average relative error (2D)	**Average relative error (3D)**	**Average relative error (total)**
AlSi20	8.1%	79.5%	43.8%
AlSi9Cu3	34.8%	59.0%	46.9%

Even though that for two-dimensional simulation with the software's material library AlSi20 as workpiece material, a relative error smaller than 10% was obtained, it is verified that, in general, there is a poor resemblance between experimental and simulated values for cutting forces. That fact can be related with several aspects:

- Imprecise aluminium alloy AlSi9Cu3 material characterization on flow stress accounting for variable strain-rates and material temperatures;
- The AlSi9Cu3 material shows very distinct compression and tension behaviours, with a less ductile behaviour in tension;
- Imprecise friction model or/and friction coefficient;

- Possibility of different mechanical properties between the tested specimens in [75] and the specimens subjected to compression tests for material characterization;
- Inability of DEFORM™ software to accurately simulate and predict cutting force results, in particular the damage behaviour of the material.

When it comes to three dimensional turning simulation it is observed that simulations with AlSi9Cu3 correspond to better depiction of real cutting forces, though still not reasonable (with an error higher than 20%).

Analyzing the maximum temperatures on 3D turning simulation of AlSi9Cu3, it is possible to observe that temperature values above the melting point were reached, which is an inconsistency of the simulated results. This means that temperature softening effect may have been underestimated, allowing the material to reach melting temperature values.

For 2D simulation of AlSi9Cu3, resultant maximum temperatures are very close to melting point, as seen in Table 6.21, which might be the reason that for higher cutting speed values, the simulations did not converge.

Table 6.21 – Simulated maximum temperature for the two considered workpiece materials (ºC)

	2D-a	**2D-b**	**2D-c**	**2D-d**	**2D-e**	**2D-f**	**2D-g**	**2D-h**
AlSi20	513	383	681	362	468	353	672	336
AlSi9Cu3	496	359	-	-	413	324	-	-

The obtained results support the fact that material characterization is very important and essential when it comes to machining simulation, where high strain-rates and temperatures are observed. One of the reasons to the discrepancy between the experimental and simulated values of cutting force can be connected with that exact matter.

It was also observed that simulations would not converge when the pure Coulomb friction model was used. This way, in order to use the friction coefficient obtained from the orthogonal cutting experimental tests, a hybrid model was defined. For the Coulomb coefficient, the average of the resultant values from the experimental work was used (0.6), while for the shear coefficient, suggested value in DEFORM™ documentation of 0.7 was used.

However, as shown in Table 6.22, it is important to note that, for the same speed magnitude, the percentage difference between the two combinations of cutting speed, depth of cut and feed

rate is similar, which gives some consistence and credibility in the accuracy of the obtained results for the AlSi9Cu3 aluminium alloy.

Table 6.22 – Percentage difference between 3D-a and 3D-b parameter configurations for FEM simulation and experimental tests.

Cutting forces	Experimental	FEM simulation
3D-a (v_c=88m/min; f=0,25 mm/rev; w=1,5mm)	281.6 N	452.4 N
3D-b (v_c=117m/min; f=0,05 mm/rev; w=0,25mm)	14.5 N	29.8 N
Percentage difference	**181,6%**	**175,1%**

Regarding tool modelling, it is interesting to note that, for 2D simulations in low cutting speed range (88-115 m/min), lower cutting forces were obtained when the tool was composed of PCD only. The contrary was observed for the higher speed range (350-397 m/min). For 3D simulations, lower cutting forces were obtained for the tool composed of WC with PCD coating for workpiece material AlSi20.

Figure 6.24 shows the obtained chip geometries for each experimental machinability test that was simulated in this dissertation. It is observed that for both workpiece materials (AlSi20 and AlSi9Cu3), predicted chip geometry correlates well in 3D-a and 3D-c cases (cutting speed range of 350-432 m/min). However, for the lower speed range, chip geometry tends to deviate from the experimentally obtained. However, the chip break observed in conditions 3D-a and 3D-c were not modelled since it requires a proper damage model that was not considered in the simulations.

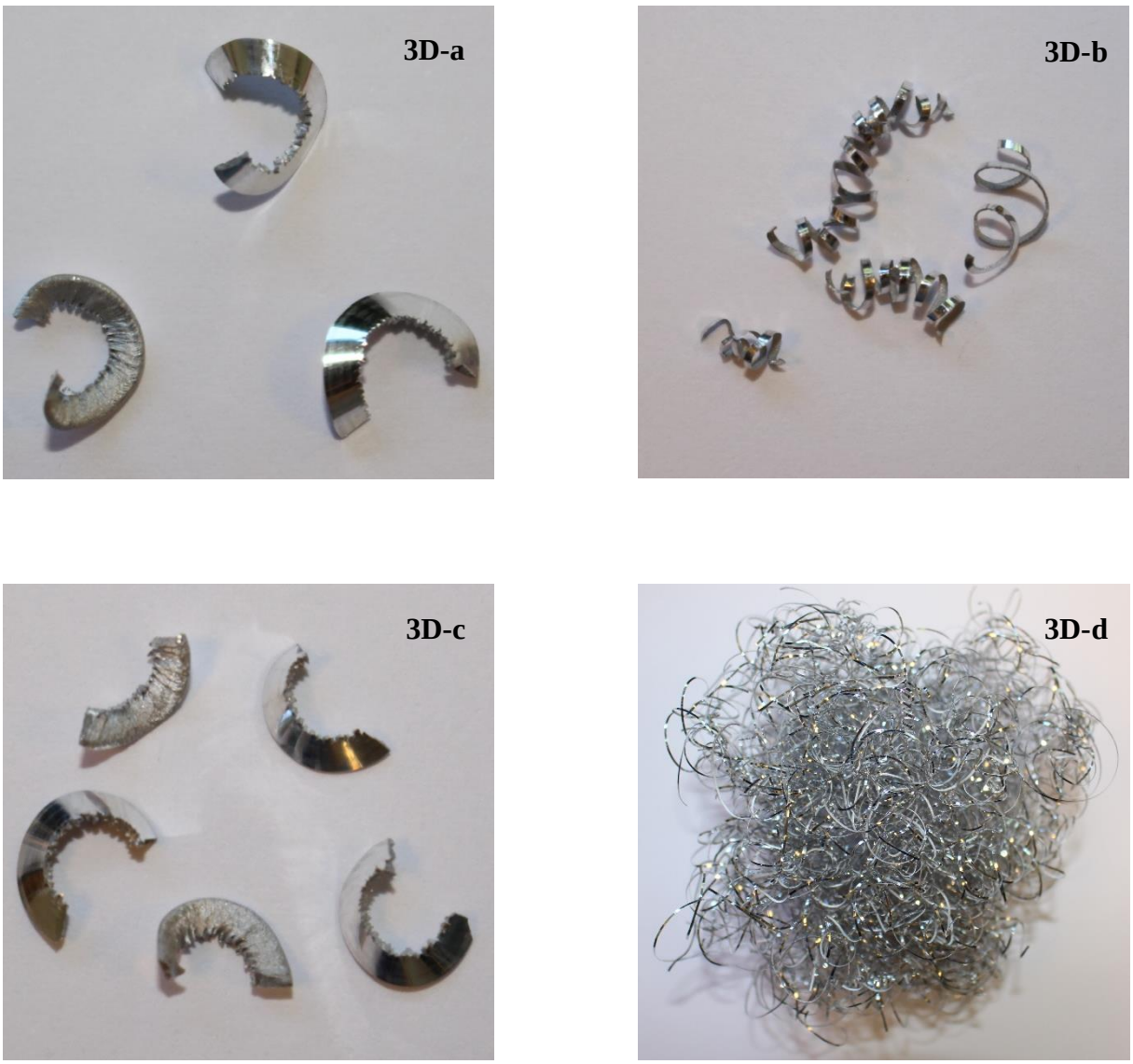

Figure 6.24 – Chip geometry obtained from machinability tests conducted in [75]

7 CONCLUSIONS AND FUTURE WORKS

7.1 Conclusions

In this chapter, the obtained conclusions are presented. A performance evaluation of the numerical simulation software and its predicting capabilities is conducted, given the led simulations for the sensitivity analysis and validation of the experimental results of cutting forces for the aluminium alloy AlSi9Cu3.

7.1.1 Sensitivity analysis study

- With increasing cutting speed, cutting forces generally decrease, while chip's curvature, tool and workpiece maximum temperatures and shear angle increase, for the three considered materials in the sensitivity analysis;

- Uncut chip thickness greatly influences cutting loads. Since the chip section to be cut is increased, cutting and feed forces, chip's curvature and maximum workpiece and tool temperatures also increase. Shear angle tends to stabilize for uncut chip thickness values of 0,5 mm;

- For bigger values of tool face rake angles, cutting loads and chip's curvature and thickness tend to decrease for Al7075 and AISI316L materials. For Titanium alloy Ti6Al4V, it is verified that the periodicity of the serrated chip increases. For the three materials, maximum workpiece temperatures decreased while maximum tool temperatures increased. Average shear angle increases for the 3 mentioned materials;

- With tool cutting edge radius increase, it can be concluded that for the three simulated materials there is an increase of the cutting loads, chip's curvature and maximum workpiece temperature. As concerns tool maximum temperature and average shear angle there is a decreasing tendency;

- Shear friction coefficient does not have a very significant influence on the cutting forces for the performed simulations. However, cutting forces increase very slightly with shear friction coefficient increasing. Additionally, maximum workpiece and tool temperatures increase while average shear angle decreases;

- Heat transfer coefficient between the tool and the workpiece does not have significant influence on the resultant cutting forces for the performed simulations;

- The same happens with mesh element size and iteration method. However, even though mesh element size does not have much influence on the average cutting forces, a finer mesh means less fluctuation on the remeshing steps, which contributes to a more precise value of cutting force and less numerical scatter.

7.1.2 Experimental validation

- The registered cutting forces obtained from the two-dimensional numerical model with AlSi20 as workpiece material correlated well with the experimental values for AlSi9Cu3, with an average relative error lower than 10%;

- For the characterized material AlSi9Cu3, the cutting forces obtained by two-dimensional modelling simulation were predicted by default, while for three-dimensional modelling, by excess;

- The simulated cutting forces obtained for the numerical models with AlSi9Cu3 as workpiece material did not reasonably match the experimental values. An average error of 46.9% was observed;

- Introducing a third dimension in the numerical models (changing from 2D to 3D simulation) significantly increases the relative error values and contributes to a bigger fluctuation on the cutting forces simulated curves;

- Even though there is not a big influence, DEFORM™ shows sensibility in cutting forces to integral PCD tools and WC tools with PCD coating;

- For the average value of the measured assumed Coulomb friction model coefficients in the conducted orthogonal tests, most of numerical models would not converge;

- Even though it is a good method to start an iterative process of friction parameter determination, applying a measured Coulomb friction coefficient does not result in good correlation of simulated values with experimental and should not be used as a final input;

- The usage of hybrid friction models is the most appropriate option which requires calibration procedures more complex than that followed in this study. For example, the numerical simulation of the orthogonal friction tests and evaluation of the friction model parameters by inverse analysis could be a good alternative;

- The fact that 2D turning simulation with workpiece material cast aluminium alloy AlSi20, available in DEFORM™ material library, presented better correlation with the experimental forces than AlSi9Cu3, characterized in this thesis, may indicate that the AlSi9Cu3 was poorly characterized and a bigger effort in material characterization is needed;

- Underestimation of temperature softening effect may have happened since melting temperature of AlSi9Cu3 was reached;

- Accurate and precise material characterization is of extreme importance. Even though material behaviour at high strain-rates and high temperatures (typical of metal cutting processes) is difficult to define, the sensitivity of constitutive models as well as its initial obtained parameters iteration consist of a good material characterization method.

7.2 Future works

In order to continue developing the work performed in this dissertation, some suggestions with the goal of better understanding the capabilities of the software and to broaden the already conducted work are presented:

- Characterizing the material at high strain rates will reduce the degree of uncertainty which can result in better predictions of metal cutting simulation;
- Using constitutive material models that account the influence of temperature on strain-rate;
- Conducting a sensitivity analysis for the Johnson and Cook material constitutive model parameters;
- Simulating the orthogonal experimental tests conducted in this dissertation;
- Exploration of friction models in a deeper approach, by running simulations with different friction coefficients for Shear, Coulomb and Hybrid models;
- Literature review on the thermal and frictional parameters that characterize wet cutting conditions and applying those to numerical simulation on DEFORM™ software in order to establish a comparison between dry and wet cutting simulation;
- Developing flow stress and damage models and implementing those as subroutines on DEFORM™ software will give a bigger control over the numerical modelling;
- As seen in Figure 7.1, obtaining tool insert's chip breaker geometry, will allow the introduction of those geometries in the numerical simulation software and predict the cutting forces and chip behaviour that are essential to make new tools.

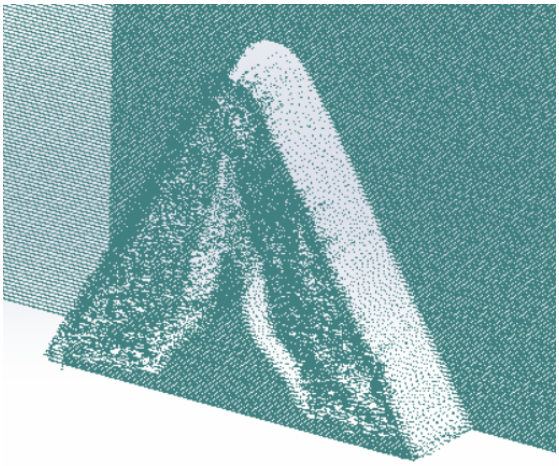

Figure 7.1 – Turning tool chip breaker geometry (point cloud)

- Extending this investigation to other machining operations such as drilling, milling and boring will give a more complete overview of the software's potential and also bigger predictive power for further investigation;

References

[1] A. P. Markopoulos, *Finite element method in machining processes*. Springer Science & Business Media, 2012.

[2] Y. Altintas, *Manufacturing Automation: Metal Cutting Mechanics, Machine Tool Vibrations, and CNC Design*. Cambridge University Press, 2012.

[3] P. J. Arrazola, T. Özel, D. Umbrello, M. Davies, and I. S. Jawahir, "Recent advances in modelling of metal machining processes," *CIRP Ann. Technol.*, vol. 62, no. 2, pp. 695–718, 2013.

[4] W. Grzesik, *Advanced machining processes of metallic materials: theory, modelling and applications*. Elsevier, 2008.

[5] M. P. Groover, *Fundamentals of Modern Manufacturing: Materials, Processes, and Systems*. John Wiley & Sons, 2010.

[6] MIT, "Cutting Processes I & II," 2008. [Online]. Available: http://web.mit.edu/2.008/www/lectures/Culpepper-Cutting.pdf.

[7] "Orthogonal Machining," 2010. [Online]. Available: http://classes.engr.oregonstate.edu/mime/winter2010/ie337-001/Laboratories/3. Orthogonal machining.pdf.

[8] M. C. Shaw, *Metal Cutting Principles*. Oxford University Press, 2005.

[9] H. K. Tönshoff and B. Denkena, "Chip Formation," in *Basics of Cutting and Abrasive Processes*, Berlin, Heidelberg: Springer Berlin Heidelberg, 2013, pp. 21–36.

[10] H.-G. Kim, J.-H. Sim, and H.-J. Kweon, "Performance evaluation of chip breaker utilizing neural network," *J. Mater. Process. Technol.*, vol. 209, no. 2, pp. 647–656, 2009.

[11] M. E. Merchant, "Mechanics of the Metal Cutting Process. I. Orthogonal Cutting and a Type 2 Chip," *J. Appl. Phys.*, vol. 16, no. 5, pp. 267–275, 1945.

[12] M. E. Merchant, "Mechanics of the Metal Cutting Process. II. Plasticity Conditions in Orthogonal Cutting," *J. Appl. Phys.*, vol. 16, no. 6, pp. 318–324, 1945.

[13] A. Moufki, A. Molinari, and D. Dudzinski, "Modelling of orthogonal cutting with a temperature dependent friction law," *J. Mech. Phys. Solids*, vol. 46, no. 10, pp. 2103–2138, 1998.

[14] A. Molinari and A. Moufki, "The Merchant's model of orthogonal cutting revisited: A new insight into the modeling of chip formation," *Int. J. Mech. Sci.*, vol. 50, no. 2, pp. 124–131, 2008.

[15] M. Bäker, "Does chip formation minimize the energy?," *Comput. Mater. Sci.*, vol. 33, no. 4, pp. 407–418, 2005.

[16] E. H. Lee and B. W. Shaffer, "The theory of plasticity applied to a problem of machining," *J. Appl. Mech.*, vol. 18, no. 4, pp. 405–413, 1951.

[17] M. R. V. Sereshk, P. Heydarizadeh, and S. M. Mostafavi, "The Evaluation of Analytical Models for Orthogonal Cutting Process," 2015.

[18] L. Pang, "Metal Cutting Forces for Engineering Alloys," University of Ontario Institute of Technology, 2012.

[19] W. B. Palmer and P. L. B. Oxley, "Mechanics of orthogonal machining," *Proc. Inst. Mech. Eng.*, vol. 173, no. 1, pp. 623–654, 1959.

[20] N. N. Zorev, *Metal cutting mechanics*. Pergamon Press, 1966.

[21] K. Okushima and K. Hitomi, "An Analysis of the Mechanism of Orthogonal Cutting and Its Application to Discontinuous Chip Formation," *J. Eng. Ind.*, vol. 83, no. 4, pp. 545–555, 1961.

[22] P. L. B. Oxley, *The mechanics of machining: an analytical approach to assessing machinability*. E. Horwood, 1989.

[23] E. Usui and A. Hirota, "Analytical prediction of three dimensional cutting process—part 2: chip formation and cutting force with conventional single-point tool," *J. Eng. Ind.*, vol. 100, no. 2, pp. 229–235, 1978.

[24] E. Usui, A. Hirota, and M. Masuko, "Analytical prediction of three dimensional cutting process—Part 1: basic cutting model and energy approach," *J. Eng. Ind.*, vol. 100, no. 2, pp. 222–228, 1978.

[25] E. Usui, T. Shirakashi, and T. Kitagawa, "Analytical prediction of three dimensional cutting process—Part 3: Cutting temperature and crater wear of carbide tool," *J. Eng. Ind.*, vol. 100, no. 2, pp. 236–243, 1978.

[26] P. A. R. Rosa, P. A. F. Martins, and A. G. Atkins, "Revisiting the fundamentals of metal cutting by means of finite elements and ductile fracture mechanics," *Int. J. Mach. Tools Manuf.*, vol. 47, no. 3–4, pp. 607–617, Mar. 2007.

[27] A. G. Atkins, "Modelling metal cutting using modern ductile fracture mechanics: quantitative explanations for some longstanding problems," *Int. J. Mech. Sci.*, vol. 45, no. 2, pp. 373–396, Feb. 2003.

[28] T. Özel, "The influence of friction models on finite element simulations of machining," *Int. J. Mach. Tools Manuf.*, vol. 46, no. 5, pp. 518–530, 2006.

[29] V. A. M. Cristino, P. A. R. Rosa, and P. A. F. Martins, "Cutting under active and inert gas shields: A contribution to the mechanics of chip flow," *Int. J. Mach. Tools Manuf.*, vol. 50, no. 10, pp. 892–900, 2010.

[30] P. J. Arrazola and T. Özel, "Investigations on the effects of friction modeling in finite element simulation of machining," *Int. J. Mech. Sci.*, vol. 52, no. 1, pp. 31–42, 2010.

[31] L. Filice, F. Micari, S. Rizzuti, and D. Umbrello, "A critical analysis on the friction modelling in orthogonal machining," *Int. J. Mach. Tools Manuf.*, vol. 47, no. 3–4, pp. 709–714, 2007.

[32] V. Kryzhanivskyy, V. Bushlya, O. Gutnichenko, I. A. Petrusha, and J.-E. Ståhl, "Modelling and Experimental Investigation of Cutting Temperature when Rough Turning Hardened Tool Steel with PCBN Tools," *Procedia CIRP*, vol. 31, pp. 489–495, 2015.

[33] R. Komanduri and Z. B. Hou, "Thermal modeling of the metal cutting process: Part I — Temperature rise distribution due to shear plane heat source," *Int. J. Mech. Sci.*, vol. 42, no. 9, pp. 1715–1752, 2000.

[34] R. Komanduri and Z. B. Hou, "Thermal modeling of the metal cutting process — Part III: temperature rise distribution due to the combined effects of shear plane heat source and the tool–chip interface frictional heat source," *Int. J. Mech. Sci.*, vol. 43, no. 1, pp. 89–107, 2001.

[35] J. P. Davim, *Machining: fundamentals and recent advances*. Springer Science & Business Media, 2008.

[36] T. Ozel, I. Llanos, J. Soriano, and P.-J. Arrazola, "3D finite element modelling of chip formation process for machining Inconel 718: comparison of FE software predictions," *Mach. Sci. Technol.*, vol. 15, no. 1, pp. 21–46, 2011.

[37] T. Özel and E. Zeren, "Finite element modeling of stresses induced by high speed machining with round edge cutting tools," in *ASME 2005 International Mechanical Engineering Congress and Exposition*, 2005, pp. 1279–1287.

[38] M. R. Vaziri, M. Salimi, and M. Mashayekhi, "A new calibration method for ductile fracture models as chip separation criteria in machining," *Simul. Model. Pract. Theory*, vol. 18, no. 9, pp. 1286–1296, 2010.

[39] F. Ducobu, E. Rivière-Lorphèvre, and E. Filippi, "Application of the Coupled Eulerian-Lagrangian (CEL) method to the modeling of orthogonal cutting," *Eur. J. Mech.*, 2016.

[40] T. Özel and E. Zeren, "Finite element method simulation of machining of AISI 1045 steel with a round edge cutting tool," in *Proceedings of the 8th CIRP International Workshop on Modeling of Machining Operations*, 2005, pp. 533–542.

[41] O. Hermes, *Alegr*. Bellum Publishing, 2012.

[42] E. Uhlmann, R. Gerstenberger, and J. Kuhnert, "Cutting Simulation with the Meshfree Finite Pointset Method," *Procedia CIRP*, vol. 8, pp. 391–396, 2013.

[43] T. Özel and Y. Karpat, "Identification of constitutive material model parameters for high-strain rate metal cutting conditions using evolutionary computational algorithms," *Mater. Manuf. Process.*, vol. 22, no. 5, pp. 659–667, 2007.

[44] T. Shirakashi, K. Maekawa, and E. Usui, "Flow stress of low carbon steel at high temperature and strain rate. I: Propriety of incremental strain method in impact compression test with rapid heating and cooling," *Bull. Japan Soc.*, 1983.

[45] C. M. A. Silva, P. A. R. Rosa, and P. A. F. Martins, "Electromagnetic Cam Driven Compression Testing Equipment," *Exp. Mech.*, vol. 52, no. 8, pp. 1211–1222, 2012.

[46] C. M. A. Silva, P. A. R. Rosa, and P. A. F. Martins, "Mechanical characterization of materials for bulk forming using a drop weight testing machine," *Proc. Inst. Mech. Eng. Part C J. Mech. Eng. Sci.*, vol. 224, no. 9, pp. 1795–1804, Sep. 2010.

[47] G. R. Johnson and W. H. Cook, "A constitutive model and data for metals subjected to large strains, high strain rates and high temperatures," in *Proceedings of the 7th International Symposium on Ballistics*, 1983, vol. 21, pp. 541–547.

[48] Y. Zhang, J. C. Outeiro, and T. Mabrouki, "On the selection of Johnson-Cook constitutive model parameters for Ti-6Al-4V using three types of numerical models of orthogonal cutting," *Procedia CIRP*, vol. 31, pp. 112–117, 2015.

[49] G. Warnecke and J.-D. Oh, "A new thermo-viscoplastic material model for finite-element-analysis of the chip formation process," *CIRP Ann. Technol.*, vol. 51, no. 1, pp. 79–82, 2002.

[50] M. Sima and T. Özel, "Modified material constitutive models for serrated chip formation simulations and experimental validation in machining of titanium alloy Ti–6Al–4V," *Int. J. Mach. Tools Manuf.*, vol. 50, no. 11, pp. 943–960, 2010.

[51] K. S. Vijay Sekar and M. Pradeep Kumar, "Finite element simulations of Ti6Al4V titanium alloy machining to assess material model parameters of the Johnson-Cook constitutive equation," *J. Brazilian Soc. Mech. Sci. Eng.*, vol. 33, no. 2, pp. 203–211, 2011.

[52] Y. B. Guo, Q. Wen, and M. F. Horstemeyer, "An internal state variable plasticity-based approach to determine dynamic loading history effects on material property in manufacturing processes," *Int. J. Mech. Sci.*, vol. 47, no. 9, pp. 1423–1441, 2005.

[53] H. F. Abed and Z. G. Voyiadjis, "A consistent modified Zerilli-Armstrong flow stress

model for BCC and FCC metals for elevated temperatures," *Acta Mech.*, vol. 175, no. 1, pp. 1–18, 2005.

[54] D. Samantaray, S. Mandal, and A. K. Bhaduri, "A comparative study on Johnson Cook, modified Zerilli–Armstrong and Arrhenius-type constitutive models to predict elevated temperature flow behaviour in modified 9Cr–1Mo steel," *Comput. Mater. Sci.*, vol. 47, no. 2, pp. 568–576, 2009.

[55] M. H. Dirikolu, T. H. C. Childs, and K. Maekawa, "Finite element simulation of chip flow in metal machining," *Int. J. Mech. Sci.*, vol. 43, no. 11, pp. 2699–2713, 2001.

[56] J. M. Huang and J. T. Black, "An Evaluation of Chip Separation Criteria for the FEM Simulation of Machining," *J. Manuf. Sci. Eng.*, vol. 118, no. 4, pp. 545–554, 1996.

[57] J. Lemaitre, *A course on damage mechanics*. Springer Science & Business Media, 2012.

[58] M. B. Mazière Jacques, "Damage in materials - From observations to simulations," 2013. [Online]. Available: http://mms2.ensmp.fr/msi_paris/transparents/Matthieu_Maziere/2013-MM-Damage.pdf.

[59] Y. Bao and T. Wierzbicki, "On fracture locus in the equivalent strain and stress triaxiality space," *Int. J. Mech. Sci.*, vol. 46, no. 1, pp. 81–98, 2004.

[60] Y. Bai, X. Teng, and T. Wierzbicki, "On the Application of Stress Triaxiality Formula for Plane Strain Fracture Testing," *J. Eng. Mater. Technol.*, vol. 131, no. 2, p. 21002, 2009.

[61] I. Barsoum and J. Faleskog, "Rupture mechanisms in combined tension and shear—Experiments," *Int. J. Solids Struct.*, vol. 44, no. 6, pp. 1768–1786, 2007.

[62] G. R. Johnson and W. H. Cook, "Fracture characteristics of three metals subjected to various strains, strain rates, temperatures and pressures," *Eng. Fract. Mech.*, vol. 21, no. 1, pp. 31–48, 1985.

[63] T. Mabrouki, C. Courbon, Y. Zhang, J. Rech, D. Nélias, M. Asad, H. Hamdi, S. Belhadi, and F. Salvatore, "Some insights on the modelling of chip formation and its morphology during metal cutting operations," *Comptes Rendus Mécanique*, vol. 344, no. 4–5, pp. 335–354, 2016.

[64] Y. Bai, "Effect of loading history on necking and fracture," 2007.

[65] F. A. McClintock, "A Criterion for Ductile Fracture by the Growth of Holes," *J. Appl. Mech.*, vol. 35, no. 2, pp. 363–371, 1968.

[66] J. Lemaitre, "A continuous damage mechanics model for ductile fracture," *J. Eng. Mater. Technol.*, vol. 107, no. 1, pp. 83–89, 1985.

[67] "Stainless Steel Fasteners." [Online]. Available: http://web.archive.org/web/20070929001157/http://www.assda.asn.au/asp/index.asp?pgid=18732. [Accessed: 23-Apr-2016].

[68] P. J. Arrazola, A. Garay, L. M. Iriarte, M. Armendia, S. Marya, and F. Le Maître, "Machinability of titanium alloys (Ti6Al4V and Ti555.3)," *J. Mater. Process. Technol.*, vol. 209, no. 5, pp. 2223–2230, 2009.

[69] S. Zhang, J. Li, X. Zhu, and H. Lv, "Saw-tooth chip formation and its effect on cutting force fluctuation in turning of Inconel 718," *Int. J. Precis. Eng. Manuf.*, vol. 14, no. 6, pp. 957–963, 2013.

[70] J. Barry, G. Byrne, and D. Lennon, "Observations on chip formation and acoustic emission in machining Ti–6Al–4V alloy," *Int. J. Mach. Tools Manuf.*, vol. 41, no. 7, pp.

1055–1070, 2001.

[71] M. J. Donachie, *Titanium: A Technical Guide, 2nd Edition*. ASM International, 2000.

[72] P. Oxley, “Shear angle solutions in orthogonal machining,” *Int. J. Mach. Tool Des. Res.*, vol. 2, no. 3, pp. 219–229, 1962.

[73] W. N. Sharpe, *Springer handbook of experimental solid mechanics*. Springer Science & Business Media, 2008.

[74] J. C. Outeiro, “Influence of tool sharpness on the thermal and mechanical phenomena generated during machining operations,” *Int. J. Mach. Mach. Mater.*, vol. 2, no. 3–4, pp. 413–432, 2007.

[75] R. Soares, “Estudos de Maquinabilidade da Liga AlSi9Cu3 Recorrendo a Ferramentas PCD com Quebra-Aparas,” Faculdade de Engenharia da Universidade do Porto, Porto, Portugal, 2016.

[76] “Alumínio e ligas de alumínio produtos vazados : composição química e características mecânicas NP EN 1706 2000 .” IPQ , Caparica , p. 20 p.–20 p., 2000.

[77] “Diamond Tool Materials for Metalworking Managers’Guide to the Review Process.”

[78] MAPAL, “Super hard cutting materials:Turning.” [Online]. Available: http://www.mapal.com/fileadmin/mapal_ftp/Blaetterkataloge/index.html?catalog=Super-hard-cutting-materials&lang=en_GB#page_1.

[79] M. P. Groover, *Fundamentals of modern manufacturing: materials processes, and systems*. John Wiley & Sons, 2007.